

Problems in Scattering and Imaging

by

Miao-Bin Lien

A dissertation submitted in partial fulfillment
of the requirements for the degree of
Doctor of Philosophy
(Electrical Engineering)
in the University of Michigan
2017

Doctoral Committee:

Professor Theodore B. Norris, Chair

Professor Jeffrey A. Fessler

Professor Nicholas A. Kotov

Associate Professor Zhaohui Zhong

Miao-Bin Lien

mblen@umich.edu

ORCID iD: 0000-0003-4370-0480

© Miao-Bin Lien 2017

DEDICATION

To my dearest family

ACKNOWLEDGEMENT

The PhD study at the University of Michigan has been a long and amazing journey for me. I am truly grateful for everyone who has accompanied me, supported me, or shared important moments with me during this period, and it is them who made this journey colorful and memorable.

First of all, I would like to express my most sincere gratitude to my advisor, Professor Ted Norris, for all the support during these years. He is a great thinker and a truly brilliant figure. Equally important, he has a pure curious mind and never sets a boundary on science. It is the unimaginable degree of freedom he offered in research that enabled me to fully explore a broad spectrum of scientific problems. I appreciate the opportunity to be his PhD student and enjoy the time working for him. Over the years, it is his careful guidance and constant encouragement that established me to be an independent researcher. I would also like to express my appreciation to all the committee faculties for the involvement in my PhD research. I would like to thank Professor Jeff Fessler for guiding me as I began a completely different research project: light field reconstruction. I am truly grateful of his devotion in the regular research discussions where he always gave me insightful feedback. I would like to thank Professor Nick Kotov for the collaboration on the projects of electrostatic and optical asymmetry of gold nanorods, which constitutes the first half part of my PhD research. I would also like to thank Professor Zhaohui Zhong for the collaboration on the project of creating a focal stack camera using graphene detectors, which is my focus of future work.

I was lucky to work with all the great lab members in Norris's group: Jessica, Momchil, You-Chia, Heather, Gong, Nooshin, Zhen, Zhengyu, and special thanks go to You-Chia and Heather. For me, You-Chia is a senior friend as well as a paragon of scholar: he is knowledgeable, diligent, and selfless. I learned so much in the discussions with him, and I sought advice from him when I need wisdom. Heather is my best partner in the lab. Doing experiments with such a capable and positive figure has always been joyful to me. Outside of lab, she is a sincere friend and always encouraging. I would also like to thank all my collaborators – Ji-Young, Moussa, Sai, Hung, Che-

Hung and more, for the inspiring discussions and the great times working together. Without their involvement, this work would not have possibly been done.

It is the moments with friends that piece together the happy memories of my life in Ann Arbor. I would like to thank all my friends and graduate peers who have accompanied me during my PhD period. You have all been an important part to my journey here.

Finally, I would like to express my deepest gratitude to my beloved family members, though words are never enough for it. I would like to thank my parents, who raised me up with love, educated me with care, and always believe in me. It is their unwavering support that allows me to pursue my dream with no reserve. I would like to thank my wife, Hsiaomin, for always standing on my side and being my warmest support. It is the sweetest blessing to have experienced every moment with you in my PhD, and to live with you the rest of my life.

TABLE OF CONTENT

DEDICATION	ii
ACKNOWLEDGEMENT	iii
LIST OF FIGURES	viii
ABSTRACT	x
CHAPTER 1 Hidden Asymmetry of Gold Nanorods	1
Section 1.1 Introduction.....	1
Section 1.2 Overview of gold nanorods.....	2
Section 1.2.1 Synthesis	2
Section 1.2.2 Plasmonic properties.....	4
Section 1.2.3 Optical properties.....	7
Section 1.2.4 Applications	10
Section 1.3 Electrostatic asymmetry of gold nanorods.....	12
Section 1.4 Optical asymmetry of gold nanorods.....	16
Section 1.5 Summary.....	20
CHAPTER 2 Optical Asymmetry and Nonlinear Light Scattering from Gold Nanorods	21
Section 2.1 Introduction.....	21
Section 2.2 Nonlinear light scatterings in noble nanoparticles.....	22
Section 2.3 The anisotropic nature of gold nanorods	23
Section 2.4 Experimental Procedures	25
Section 2.4.1 Experimental setup.....	25
Section 2.4.2 Gold nanorod characterization.....	26

Section 2.4.3	Extraction of intensity dependence	27
Section 2.5	The nonconventional scaling of HG	30
Section 2.5.1	Previous works and the experimental results.....	30
Section 2.5.2	HG with optically induced plasmon damping	31
Section 2.6	Origin of the broadband photoluminescence	33
Section 2.6.1	Previous works and the experimental results.....	33
Section 2.6.2	Novel physical model for the broadband photoluminescence	35
Section 2.7	Summary	37
CHAPTER 3	Controlling Light Transmission Through Highly Scattering Media.....	39
Section 3.1	Introduction.....	39
Section 3.2	Previous works.....	40
Section 3.3	Algorithm.....	41
Section 3.3.1	Transmission matrix formulation.....	41
Section 3.3.2	Spatial light modulation	43
Section 3.3.3	Phase retrieval with SDP	44
Section 3.4	Experimental results.....	46
Section 3.5	Summary	50
CHAPTER 4	Optics of Graphene	51
Section 4.1	Introduction.....	51
Section 4.2	Overview of graphene.....	53
Section 4.2.1	Electronic properties of graphene	53
Section 4.2.2	Optical properties of graphene.....	57
Section 4.3	Absorption saturation in optically excited graphene	61
Section 4.3.1	The microscopic theory.....	61
Section 4.3.2	The optical experiment	66

Section 4.4	Light field camera with graphene focal stack	70
Section 4.4.1	All-Graphene Heterojunction Photodetector	70
Section 4.4.2	Prototype single-pixel camera with graphene detectors	73
Section 4.5	Summary	76
CHAPTER 5	Light Field Reconstruction from a Focal Stack.....	77
Section 5.1	Introduction.....	77
Section 5.2	Overview of light field.....	79
Section 5.3	Design of the focal stack light field camera.....	81
Section 5.3.1	Light field transport and camera modeling.....	81
Section 5.3.2	Light field imaging and transformation	85
Section 5.3.3	Fourier slice sampling and the detector configuration.....	87
Section 5.4	Light field reconstruction from focal stack.....	90
Section 5.4.1	Reconstruction settings	90
Section 5.4.2	Light field reconstruction of the synthetic scene	92
Section 5.5	Summary	97
CHAPTER 6	Retrospect and Prospect	98
Section 6.1	Nonlinear light scattering of nano-plasmonics	98
Section 6.2	Light transmission through highly scattering media.....	99
Section 6.3	Light field imaging based on graphene optics	100
APPENDIX	Focal Stack Camera with Synthetic Focal Lengths.....	102
BIBLIOGRAPHY	105

LIST OF FIGURES

Figure 1.1 The modern synthesis methods for AuNR.	3
Figure 1.2 Plasmon oscillations of gold nanoparticles.	5
Figure 1.3 GNRs with tunable absorption bands at visible and NIR wavelengths.	6
Figure 1.4 Calculated absorbances from Gans theory.	9
Figure 1.5 Electrostatic distribution of individual AuNRs.	13
Figure 1.6 Non-centrosymmetric distribution of CTAB on AuNR.	14
Figure 1.7 Kelvin probe microscopy.	15
Figure 1.8 The PSS/AuNR film sample.	17
Figure 1.9 Photoluminescence and SHG from AuNRs film samples.	19
Figure 2.1 Structural symmetry and electrostatic asymmetry of AuNR.	24
Figure 2.2 The experimental setup for the study on the nonlinear light scattering from AuNRs.	26
Figure 2.3 Intensity dependence measurements of Rhodamine 6G.	29
Figure 2.4 Nonlinear optical response on resonant excitation with 800-nm ultrashort pulses.	31
Figure 2.5 Measurement of the spectral dependence of the intensity scaling of the PL.	34
Figure 2.6 Picture of the PL nonlinear light scattering process and the reproduced PL spectra.	36
Figure 3.1 The schematic and geometric settings of the scattering system.	42
Figure 3.2 Experimental setup for the TM determination using SDP method.	47
Figure 3.3 Optimal light focusing through ground glass sample.	48
Figure 3.4 Optimal light focusing through yogurt sample.	49
Figure 3.5 Spell-out of words beyond the scattering media using SDP method.	50
Figure 4.1 Electronic configuration of graphene.	53
Figure 4.2 Honeycomb lattice and its Brillouin zone.	54
Figure 4.3 Electronic dispersion in the honeycomb lattice.	56
Figure 4.4 Light-induced transitions in doped graphene.	58
Figure 4.5 Optical conductivity of graphene with linear response theory.	59
Figure 4.6 The electrically tunable optical conductivity of graphene.	60

Figure 4.7 The broadband spectrum of the optical conductivity of graphene.	61
Figure 4.8 Illustration of the optical saturation in graphene.	64
Figure 4.9 Saturation behavior in consideration of different scattering channels.	65
Figure 4.10 Experimental setup for the differential transmission measurements.	67
Figure 4.11 Images of multilayer epitaxial graphene (MEG).	68
Figure 4.12 Experimentally determined saturation of transmission.	69
Figure 4.13 Device structure and working mechanism of the graphene photodetector.	71
Figure 4.14 The all-graphene transparent heterojunction photodetector.	73
Figure 4.15 Prototype single-pixel focal stack camera.	74
Figure 4.16 Demonstration of optical ranging.	76
Figure 5.1 Light field parameterizations.	80
Figure 5.2 Schematic of light field transport in the photography process.	82
Figure 5.3 Light field transformation in the photography process.	84
Figure 5.4 Schematic of the proposed focal stack camera.	85
Figure 5.5 Fourier slice sampling.	89
Figure 5.6 Focal stack camera with synthetic focal lengths.	91
Figure 5.7 Planar scene objects of two patterned disks.	93
Figure 5.8 Focal stack of the worst-case sampling.	94
Figure 5.9 Focal stack images of the photorealistic scene.	95
Figure 5.10 Light field reconstruction of the photorealistic scene.	96
Figure 5.11 Demonstration of perspective shift and multi-view stereo.	96
Figure A.1 Two focal stack camera schemes.	102
Figure A.2 Synthetic refocusing and scaling operations.	103

ABSTRACT

Technology advances are always driven by the discovery of new materials, better understanding of their properties and improvements in processing power. This trend is reflected in this work, where I will demonstrate how new science and applications of both scattering and imaging are enabled by these frontiers.

This thesis explores a broad spectrum of topics associated with the problems of scattering and imaging. The first topic concerns the fundamental study of the symmetry breaking and the nonlinear light scattering in the system of gold nanorod. In the most recent experiments, the intrinsic electrostatic asymmetry of gold nanorods was investigated by Ji-Young et al. using a variety of microscopy techniques, and the associated optical asymmetry was immediately demonstrated through the nonlinear optical experiments. The understanding of the symmetry breaking of gold nanorods, motivated the development of a model where the second order longitudinal plasmon resonance mode scatters with the electron gas and accounting for the plasmon damping effect. The new microscopic description self-consistently explains all the main features of the nonlinear optical components, and provides a fresh look that beautifully aligns with the recent observations of the nonlinear optical properties of nanorods.

Next, we demonstrate an optical system that enables the control of monochromatic light transmission through highly scattering media, with Complex Semi-Definite Programming (SDP) introduced as a novel approach to solve the associated phase retrieval problem. In contrast to the conventional approach that employed an interferometric design which is vulnerable to system vibration, a simple optical setup without the need for a reference beam is proposed by Moussa et al. The SDP algorithm allows computation of the complex transmission matrix of the system from a sequence of intensity speckle patterns generated with phase-modulated wavefronts. We showed that once the transmission matrix is determined, optimal wavefronts can be computed that focuses the incident beam to any position on the far side of the scattering medium, without the need for subsequent measurements or wavefront shaping iterations.

Finally, the optical properties and applications of graphene were explored. As a true 2D material, graphene has a unique electronic band structure and has been demonstrated by various research groups to be an interesting photonic building block. At first, we focused on the absorption saturation in optically excited graphene. The microscopic theory that includes Coulomb-scattering as the dominant relaxation mechanism at high carrier densities was developed and then verified by the optical transmission experiment. Then, we showed a novel scheme of a light field camera using a focal stack proposed by a team at the University of Michigan. The key enabling technology is the highly transparent graphene photodetector fabricated by Che-Hung et al., where graphene is used both as the photoconductive gain material and the circuit interconnects. Physically, we built the prototype single-pixel light field camera and demonstrated its operation through optical experiment. Computationally, a synthetic camera system was designed based on the Fourier slice analysis and the framework for the model-based light field reconstruction was provided.

CHAPTER 1

Hidden Asymmetry of Gold Nanorods

Section 1.1 Introduction

The symmetry of molecules and particles is of great importance in various fields of science. In many cases, the symmetry of the material system plays the central role in determining the electronic structure, optical properties and particle dynamics. Therefore, symmetry consideration is one of the key component in the frontier research of self-assembly¹ and highly nonlinear system.² Due to the multicomponent nature and multiscale dynamics, a complete symmetry characterization of nanoscale colloid system is a challenging task. Symmetry assignments to nanoscale colloids therefore often simplifies to the geometry measurement of the metal core structure. In this study, we revisited the symmetry of gold nanorods (AuNRs) which show nearly perfect geometry of a cylinder under transmission electron microscopy (TEM). Among various noble metal nanostructures, AuNRs receive particular interest due to their versatility in the field of biomedical engineering. The ability to modify the surface and conjugate molecules makes AuNR fascinating candidate for drug and gene delivery applications.³ The ability to support optical-frequency surface-plasmon, which directly leads to the strong interaction with light, enables all the exciting applications of nano-scale optical imaging, photothermal therapy and molecule-level sensing.⁴ Fundamental studies on the AuNRs continue to be active and interesting.

While AuNRs were generally presumed to be centrosymmetric, over the past decade there have been multiple plasmonics studies on the AuNR that have consistently observed evidence of the system being non-centrosymmetric. Experiments include different plasmon mapping techniques such as electron energy loss spectroscopy (EELS),⁵ cathodoluminescence,⁶ and near-field microscopy.⁷ The observations were nonetheless simply attributed to either unspecified effects of the local environments around the NRs, or the non-perfect geometry due to AuNR surface defects without in-depth investigation. In the most recent experiments, the hidden

electrostatic asymmetry of AuNRs was investigated with a variety of microscopy techniques, and the physical origin of this asymmetry is revealed to be associated with a constantly unequal number of cetyltrimethylammonium bromide (CTAB) moieties capping the two ends of the AuNRs. In this study, we provide another key piece of evidence supporting the anisotropic nature of the AuNRs through a series of nonlinear optical (NLO) experiments. Optically transparent films containing AuNRs with and without electrostatic asymmetry were prepared and excited with ultrafast laser pulses to investigate the NLO properties in the context of different symmetry conditions of AuNRs. The behaviors of the measured second harmonic generation (SHG) and nonlinear photoluminescence (NPL) show excellent agreement with the asymmetry assumption of AuNRs. This is a strong confirmation of the anisotropic nature of AuNRs and further provides a new pathway to explain and control NLO properties.

Interestingly, the understanding of AuNRs being optically anisotropic in turn motivated the development of a novel microscopic model that simultaneously, self-consistently, and quantitatively explains all the main features of the SHG, third harmonic generation (THG), and NPL. The proposed model resolved the long-standing, puzzling discrepancies in nonlinear optical effects reported previously in other literatures based on the conventional electron-hole recombination process and the centrosymmetric assumption, and is the focus in the subsequent chapter.

This is a work done in collaboration with Prof. Nicholas Kotov's group. The symmetry characterization using microscopy techniques was done by Ji-Young Kim et al. I performed the nonlinear optical experiments. The result of this project is published on *Science Advances* titled "Hidden Asymmetry of Gold Nanorods".⁸

Section 1.2 Overview of gold nanorods

Section 1.2.1 Synthesis

A truly convenient synthesis method that is in a controllable and reproducible fashion was introduced in the early 2000s.⁹ This new seed-mediated growth method offers simplicity in the procedure, high quality and yield of nanorods, ease of particle size controlling, and flexibility for structural modifications. The approach has become the model for almost all subsequent AuNR

syntheses. The three-step seeded growth method was the first of this kind implemented in 2001,^{10,11} which involves the addition of citrate-stabilized small gold nanospheres (GNS) to a growth solution containing HAuCl_4 and CTAB. First-stage gold nanorods are used as seeds for second growth, and then sequentially used as seeds for third growth, providing AuNRs with larger aspect ratios between 10 and 25. The drawback however, is the large fraction of GNS produced, which requires the additional centrifugation steps to separate the rods from the spheres. In 2003, a one-step, silver-assisted seeded growth procedure was invented.¹² Instead of the sodium citrate, a stronger CTAB stabilizer is utilized in the seed formation process and silver ions from AgNO_3 were added to control the aspect ratio of gold nanorods. The new protocol is particularly useful in the synthesis of smaller aspect ratio AuNRs between 2 and 5. Moreover, the one-step method significantly improves the yield such that better than 95% yield relative to other shapes is achieved compared with the three-step procedure, therefore avoids the needs for repetitive centrifugations to remove the spheres. At the present, silver-assisted seeded growth method remains the most popular protocol for AuNR synthesis due to its convenience and the ability to precisely control the aspect ratio.




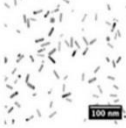
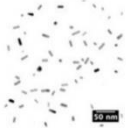
<u>Year</u>	<u>Seed</u>	<u>Growth Solution</u>	<u>AuNR Properties/Structure</u>	<u>Notes</u>
2001	 3.5 nm Citrate AuNP	HAuCl_4 , CTAB, Ascorbic Acid	 Dimensions: ~400 x 25 nm	<ul style="list-style-type: none"> • 5% rod yield (by shape) • AR 6-20 • Penta-twinned crystals
2003	 1.5 nm CTAB AuNP	HAuCl_4 , CTAB, AgNO_3 , Ascorbic Acid	 Dimensions: ~60 x 12 nm	<ul style="list-style-type: none"> • 95% rod yield (by shape) • 15% rod yield (total gold) • AR 1.5-5.0 • Single crystals
2005	-- No Seed BH_4^- addition	HAuCl_4 , CTAB, AgNO_3 , Ascorbic Acid	 Dimensions: ~20 x 6 nm	<ul style="list-style-type: none"> • Undetermined yield • AR 1.5-5.0 • Single crystals

Figure 1.1 The modern synthesis methods for AuNR. Top: the three-step seeded growth method. Middle: the one-step, silver-assisted seeded growth method. Bottom: the "seedless" silver-assisted AuNR growth method. Adapted from ref⁹.

More recently, a new “seedless” silver-assisted AuNR growth method was developed.¹³ The preparation is similar to the standard silver-assisted seeded growth method, but instead of using preformed seeds, the seed is generated *in situ* by adding a small amount of the strong reducing agent BH_4^- . In addition, the aspect ratio is controlled through the concentration of BH_4^- rather than the concentration of AgNO_3 , within the range between 2 and 5. Though the scale-up is relatively complicated due to the high concentration of CTAB, it has been demonstrated that, the synthesis of AuNRs up to the gram scale can be achieved using this approach. Another distinct feature that attracts attention is that this method tends to generate AuNRs with notably smaller dimensions when compared with the AuNRs prepared by the traditional seed-mediated growth method.¹⁴ This provides advantages in the biomedical applications, since the smaller AuNRs not only facilitates transport through biological systems, but also have increased absorption and reduced light scattering, making them more effective as photothermal therapy agents.

In summary, the modern synthesis of AuNRs has developed into three main approaches: (i) the original three-step seeded growth protocol using citrate-stabilized AuNPs as seeds, (ii) the silver-assisted seeded one-step seeded growth protocol using CTAB-stabilized AuNPs as seeds, and (iii) the seedless silver-assisted synthesis, where seeds are formed *in situ* by adding BH_4^- . Each method has its own strength and weakness. The principal drawback associated with these synthesis methods is that, even with the development of several gram-scale approaches these syntheses remain relatively low-yielding in the absolute sense. Finally, it should be noted that, though different approaches can produce AuNRs with different crystal structures (ex: single crystalline or pentatetrahedrally twinned), they display very similar optical properties⁹ and therefore crystallography is not a differentiating factor to be considered in the optical experiment.

Section 1.2.2 Plasmonic properties

Noble metal nanoparticles have distinguished themselves from other classes of metallic nanoparticles with the ability to confine resonant photons. When resonant with the frequency of light, the conduction band electrons of the noble metal nanoparticle experience a collective coherent oscillation, which is called the surface plasmon resonance (SPR).¹⁵ The oscillation induces a charge separation between the free electrons and the background ionic sites, which in turn exerts a restoring Coulomb force to make the electrons oscillate back and forth on the particle

surface, resulting in a dipole oscillation in the simplest case, see Fig 1.2. When the SPR is excited, the surface electromagnetic fields propagate around the particle and decay exponentially over a distance comparable to the particle size, leading to a strong localization effect.¹⁶

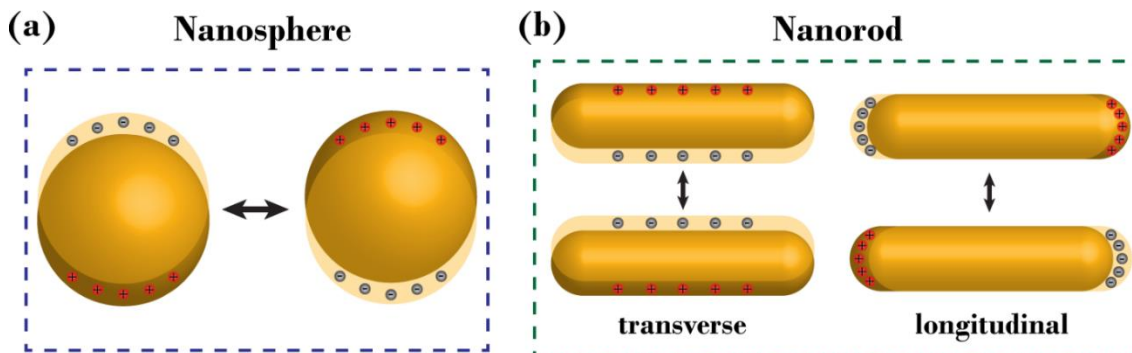


Figure 1.2 Plasmon oscillations of gold nanoparticles. Plasmon oscillations of (a) nanospheres and (b) nanorods. Note that while nanospheres have only one mode, nanorods have two that correspond to the transverse and longitudinal oscillations.

The photon confinement increases the amplitude of the light by orders of magnitude, which dramatically increases the light intensity as the intensity is proportional to the square of the amplitude. Through plasmonic confinement, noble metal nanoparticles resonantly focus coupled light. All radiative properties, such as light absorption, fluorescence, Rayleigh (Mie) scattering, and Raman scattering are boosted by this plasmonic enhancement. A remarkable feature of plasmonic nanoparticles is the degree by which their optical properties can be tuned through changes in their size, shape, composition, structure, and, when assembled, their relative interparticle orientation and separation.¹⁷

For AuNRs, electron oscillation can occur either along the short axis or the long axis, depending on the polarization of the incident light. The SPR along the short axis would induce an absorption band in the visible region at shorter wavelength, referred to as the transverse mode. The SPR along the long axis would induce a much stronger absorption band in the longer wavelength region, referred to as the longitudinal mode. The transverse mode of AuNRs inherits its properties from the isotropic plasmonic mode of the AuNSs, including the wavelength of the absorption peak (at 520 nm) and the insensitiveness to the increasing particle size as well as aspect ratio (only

slightly red-shifts). The longitudinal band on the other hand, can have large red-shift from the visible to near-infrared region with increasing aspect ratio, see Fig 1.3(a).

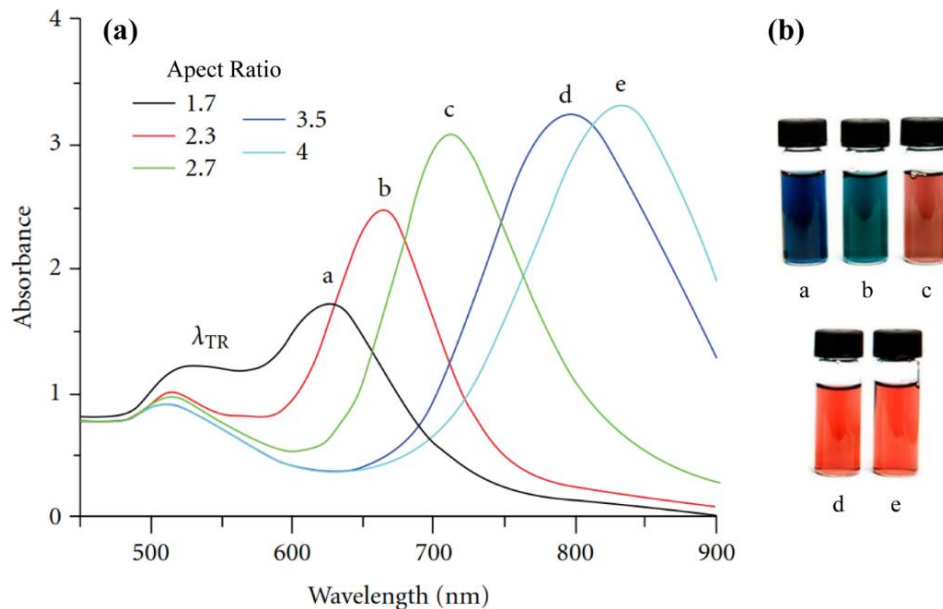


Figure 1.3 GNRs with tunable absorption bands at visible and NIR wavelengths. (a) Experimental absorption spectra of GNRs with different aspect ratios. The absorption peak exhibits red-shift with increasing aspect ratio. (b) GNR colloidal solutions used for the measurements in (a). Adapted from ref ¹⁸.

The SPR linewidth plays an important role in the sensitivity of SPR to local environmental changes.¹⁹ Narrow linewidth gives higher sensitivity and is associated with the large near-field enhancement. The resonance linewidth is inversely proportional to the lifetime of the plasmon. When a plasmon is created, it subsequently undergoes processes that damp the collective oscillation and ultimately results in its decay. Damping can occur through radiative or nonradiative processes. Radiative damping occurs when the oscillating dipole moment of the plasmon gives rise to photon emission. Nonradiative damping occurs when the plasmon excites intraband or interband electronic transitions or through electron scattering processes at the surface of the nanostructure. At a fixed rod width, AuNRs with a high aspect ratio show narrower linewidths and hence longer lifetimes due to the reduced nonradiative plasmon decay.²⁰ At a fixed aspect ratio, the relationship between the lifetime and the rod width is however not monotonic. When the rod width keeps increasing, the larger volumes would associate with the increased radiative damping.

When the width keeps decreasing, intense surface scattering would eventually occur when the width is significantly smaller than the electronic mean free path of gold (20 nm). The two competing processes together determines an optimum rod width in the range of 10-20 nm that leads to the sharpest resonance, the longest lifetime, and the greatest near-fields.²¹

Finally, the field enhancement for various nanoparticle shapes was compared using discrete dipole approximation (DDA) calculations.²² The results indicated that prisms, rods, and spheroids with similar size dimension show similar intensity enhancement on the scale of 10^3 or more, which is significantly higher than spheres (10^2). The computed field distribution also concluded that high curvature nanoparticles would give a strong field enhancement (lightning-rod effect) and for AuNRs, they show much higher electric fields at the end of the long axis and weakest fields at the center of the rods.

Section 1.2.3 Optical properties

The resonantly enhanced scattering from AuNRs greatly increases their functionality in optical imaging. The plasmonic resonance critically improves the optical imaging resolving power, thereby beating the diffraction limit as a direct consequence of the strong localization of light down to the nano-scale particle size. The SPR oscillation induces a strong absorption of light, as seen in the UV–VIS spectrum, which is the origin for the observed color of the colloidal solution, see Fig 1.3(b). While AuNRs are well-known to be cylinder-like with two hemisphere caps on the ends under TEM, it turns out that proper approximation with ellipsoid particles in the EM modeling is sufficient to capture many of the key features of the optical properties found in the physical experiments. The complete EM fields of the sub-wavelength ellipsoid particles can be solved with Gans theory,¹⁵ which helps explain the optical behaviors such as how the longitudinal absorption band can red-shift largely from the visible to near-infrared region with increasing aspect ratio and media dielectric constant, see Fig 1.4.

Gans theory is the extension of Mie theory for the case of spheroidal particles. It provides the analytical solutions for the scattering characteristics of both oblate and prolate spheroidal particles much smaller than the excitation wavelength. In Gans theory, the absorption spectrum is only dependent on the aspect ratio of the particles and not on the absolute dimensions. This

dependence is introduced through so called polarization or shape factors related to the three dimensions of the particle. For the case of spheroids, this reduces to only two different factors since the particle is rotational symmetric around one axis. Most important, the quantitative description of the cross-sections of absorption (C_{abs}), scattering (C_{sca}), and total extinction (C_{ext}) can be derived from Gans theory:

$$C_{\text{abs}} = \frac{2\pi}{3\lambda} \epsilon_m^{3/2} V \sum_i \frac{\epsilon_2/P_i^2}{\left[\epsilon_1 + \left(\frac{1-P_i}{P_i}\right)\epsilon_m\right]^2 + \epsilon_2^2}$$

$$C_{\text{sca}} = \frac{8\pi^3}{9\lambda^4} \epsilon_m^2 V^2 \sum_i \frac{(\epsilon_1 - \epsilon_m)^2 + (\epsilon_2/P_i)^2}{\left[\epsilon_1 + \left(\frac{1-P_i}{P_i}\right)\epsilon_m\right]^2 + \epsilon_2^2}$$

$$C_{\text{ext}} = C_{\text{abs}} + C_{\text{sca}}$$

where λ is the wavelength of light, V the unit volume of the nanoparticle, ϵ_m the dielectric constant of the surrounding medium, ϵ the dielectric constant of the metal given by $\epsilon = \epsilon_1 + i\epsilon_2$, and P_i the depolarization factor, defined by:

$$P_a = \frac{2}{R^2-1} \left(\frac{R}{2\sqrt{R^2-1}} \ln \frac{R+\sqrt{R^2-1}}{R-\sqrt{R^2-1}} - 1 \right)$$

$$P_b = P_c = (1 - P_a)/2$$

where a , b , and c are the length of the three ellipsoid axes, $a > b = c$, and $R = a/b$ is the aspect ratio. Some numerical examples of calculated absorbances using Gans theory are shown in Fig 1.4. Spheres are considered as the degenerate case of $P_a = P_b = P_c = 1/3$. The absorption, scattering, and total extinction of gold nanorods not only depend on the wavelength of the light, but also the particle aspect ratio and size. The SPR occurs at $\epsilon_1 = -\left(\frac{1-P_i}{P_i}\right)\epsilon_m$, where $i = a$ corresponds to the longitudinal mode and $i = b, c$ corresponds to the transverse mode. At such resonance wavelengths, the absorption, scattering, and total extinction are all strongly enhanced, which is the basis for their application in biomedical imaging and therapeutics.

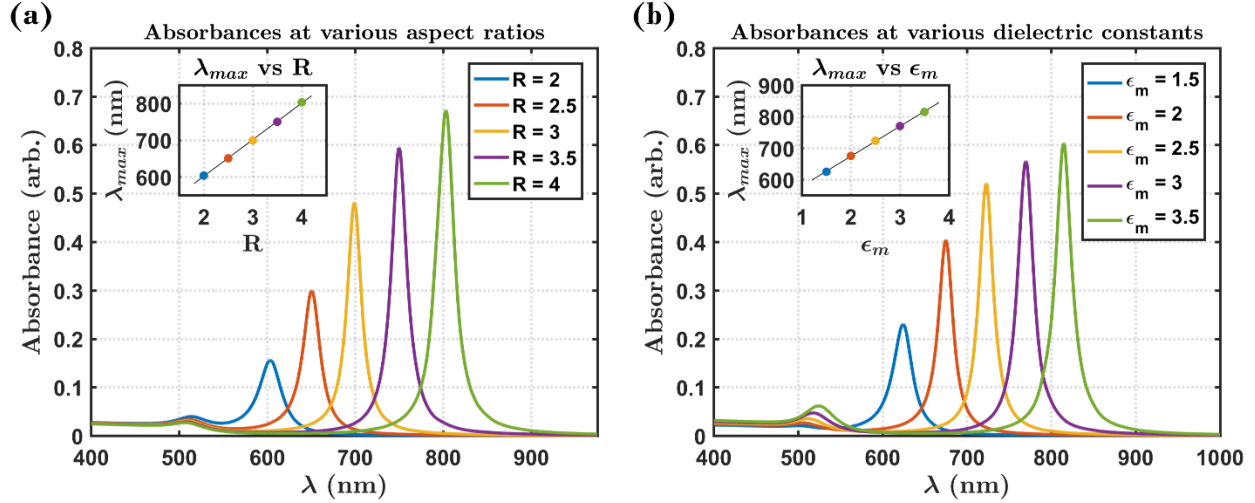


Figure 1.4 Calculated absorbances from Gans theory. Longitudinal absorption band red-shifts (a) with increasing aspect ratio, R (at $\epsilon_m = 1.5$) and (b) with increasing media dielectric constant, ϵ_m (at $R = 3$). Within the range of these specific examples, the spectral location of the maximal absorbance, λ_{max} , is almost linearly proportional to both R and ϵ_m , see insets. Dielectric constant of gold adapted from ref ²³.

The relative contribution of the absorption and scattering to the total extinction at different aspect ratios and sizes can be quantified through scattering quantum yield: $\eta = \left. \frac{Q_{sca}}{Q_{ext}} \right|_{Res}$, defined as the ratio of scattering efficiency (Q_{sca}) to the total extinction efficiency (Q_{ext}) at their respective resonance maxima. In Gans theory, η increases with V , which explains the fact that at a fixed aspect ratio, the absorption efficiency is dominant for smaller rods and the scattering efficiency is dominant for larger rods, offering a golden standard for choosing gold nanoparticles for biomedical applications. For imaging, larger nanoparticles are preferred because of their higher scattering efficiency, whereas for photothermal therapy, smaller nanoparticles are preferred as light is mainly adsorbed by the particles, and thus, efficiently converted to heat for cell and tissue destruction.

Despite the success of Gans theory in explaining many of the optical behaviors of AuNRs in an elegant way, there still exist discrepancies between its predictions and the experimental data. Most glaring is that λ_{max} does not only depend on the particle aspect ratio but also on the particle width and length independently.²⁴ To better model the exact shape of AuNRs, a generic and powerful method, discrete dipole approximation (DDA) is used. The DDA is a numerical method that represents the object as a cubic lattice of N polarizable point dipoles, each characterized by a

polarizability α_i . There is no restriction on the localization of cubic lattice sites so that the DDA represents a particle of arbitrary shape and composition.²⁵ The precise modeling of the cylinder shape and the rod end-cap geometry (flat, oblate spheroid, or sphere) correctly accounts for the width and length dependence, providing the more accurate optical properties of AuNRs.²⁴

Section 1.2.4 Applications

AuNRs are such versatile nanoparticles that find numerous applications in various areas. But perhaps, the most exciting field where they can make tremendous impacts is the biomedical engineering, due to their physical, chemical, and optical properties. One important aspect is their all-around capabilities to work in the biomedical system, including the nanoscale size (facile transport with fluid), the relative biocompatibility (the gold core of AuNRs is considered as non-toxic), and the ability to be chemically functionalized (so that they can carry specific proteins or DNA). The other aspect is their strong interaction with the light in the visible and infrared range, thanks to the presence of SPR when excited with light. This leads to their great potentials in optical imaging (due to the intense light scattering), photothermal therapy (with the efficient heat transfer from the absorbed photon energy) and chemical sensing (from the sensitivity of plasmonic resonance to the environmental susceptibility). In addition, plasmonic and optical properties such as surface plasmon wavelengths, scattering and absorption cross sections can be tailored with the control of the environmental susceptibility and the rod aspect ratio, offering great flexibility in engineering and design.

One of the intrinsic advantages shared by all nanoparticles in the biomedical applications is the enhanced permeability and retention effects (EPR), enabling them to preferably accumulate in tumor tissues than in normal ones due to the leaky tumor blood vasculature (passive targeting).^{26,27} With the additional attachment of recognition molecules (e.g., antibodies), nanoparticles can achieve enhanced targeting to the desired location (active targeting).^{28,29} The extremely high surface area to volume ratio of nanoparticles maximizes the payload/carrier ratio and is advantageous in providing the high local concentration of drug released at the targeted tissue or cells, which in principle can make significantly greater effect than the conventional single dose treatment. Since gold is one of the most chemically inert metals in the bulk, it is a natural choice

of material for nanoparticles as a therapeutic agent, and considerable efforts were made to develop AuNRs as drug delivery vehicles.^{3,30}

There are numerous examples of methods for conjugating NRs with biomolecular labels for cell targeting or intracellular delivery, such as folic acid,^{31,32} antibodies^{33,34} and DNA/RNA.^{35,36} Various surface functionalization methods of attaching the payload have been demonstrated. For one example, a thiolated DNA can be used to displace the CTAB bilayer resulting in DNA-modified AuNRs.³⁷ For another, the CTAB bilayer can be replaced with a nonionic surfactant, which is then replaced with a cationic phospholipid, and the RNA is then associated with the AuNRs through electrostatic complexation.³⁸ Efficient release of these nano-scale agents is also of great importance in determining the effectiveness of the therapy. For general classes of nanoparticle, the release could be triggered internally in a biologically control manner (ex: glutathione³⁹ or pH⁴⁰). Gold nanoparticles, especially AuNRs, are additionally capable of spatio-temporal control via external stimuli of light, making them superior candidates over other nanoparticles as therapeutic agents.^{37,41–43}

In addition to all the common benefits of nanoparticles mentioned earlier, what makes AuNRs distinctive is the ability to support visible/infrared plasmonic modes, which leads to the intense mutual interaction with light. As a matter of fact, their absorption cross sections can be at least five orders larger than those of conventional dyes.⁴⁴ The light scattering by gold nanorods can be several orders larger than the light emission from efficient fluorescent dyes. Compared to the bulk gold, the fluorescence can be enhanced over a million times.⁴⁵ The plasmonic properties strongly depends on the size of rods, the aspect ratio, and the surrounding medium.⁴ Each of these modalities has been exploited to find interesting applications, and we review some of the impressive demonstrations below.

When light strongly interacts with the AuNRs, it can be scattering or absorbed, which can be advantageous in different cases.⁴⁶ For the applications of optical imaging, larger AuNRs are preferred because of their higher scattering efficiency. Related studies include cancer cell imaging via scattering from the AuNRs in dark field,⁴⁷ *in vitro* and *in vivo* two-photon luminescence imaging,⁴⁸ optical coherence tomography (OCT) for molecular contrast enhancement,⁴⁹ and photoacoustic imaging using bio-conjugated AuNRs.⁵⁰ For the applications of photothermal therapy, smaller AuNRs are preferred as light is mainly adsorbed by the particles and then

efficiently converted to heat for cell and tissue destruction. The temperature increases through photothermal effect has been reported to range from 10 °C to 1000 °C,⁵¹ sufficient to cause irreversible damage to pathogens, cultured cancer cells, and tumor tissue. Examples of application include selective photothermal therapy with anti-bodies conjugated AuNRs,⁵² AuNR assisted plasmonic photothermal therapy,⁵³ and computationally guided photothermal tumor destruction.⁵⁴ In some of the studies, the advantage of photothermal therapy with the imaging modality at the same time, unique for AuNRs, were demonstrated.

The wavelengths of light that gold nanorods absorb and scatter are sensitive to the changes in the dielectric constant of the medium surrounding the nanorods, and to aggregation state of the nanorods.⁵⁵ Increasing dielectric constant of the surrounding medium leads a red-shift of the SPR peak of AuNRs, which essentially serves as a means to monitor the changes of the local environment of the nanoparticle. The dependence of the fractional shift of the plasmon wavelength from coupled pairs of nanoparticles on the interparticle distance (in units of the particle size) has also been exploited to measure intersite distances in biological systems.⁵⁶ In this regard, bio/chemical sensor and molecule ruler are the primary applications. Related works include chemical⁵⁷ and biomedical⁵⁸ sensing, detection of assembly configuration,⁵⁹ and the kinetics study of protein absorption by temporally monitoring the shifts in the plasmonic absorption bands.⁶⁰

AuNRs have been proven to be an exciting building block in different disciplines. They have shown exceptional properties with a variety of demonstrated applications. The fundamental understanding of AuNRs and their potential applications continue to be explored and remains an active area of research.

Section 1.3 Electrostatic asymmetry of gold nanorods

Being focus of this work, the electrostatic asymmetry of the AuNRs was investigated with a variety of microscopy techniques, resulting in two important conclusions: (i) the electrostatic potential gradient was explicitly measured on the AuNRs that are centrosymmetric with respect to the gold core, thus confirming the existence of the electrostatic asymmetry that does not arise from the structural defects, and (ii) the physical origin is associated with a consistently unequal number

of CTAB moieties capping the two ends of the AuNRs. Each of the above inferences was supported by a group of experiments, as elaborated below.

The existence of electrostatic asymmetry has been observed previously, primarily from the experiments associated with plasmon mapping techniques.^{5,61} The recorded observations however, are often overlooked because these observations cannot be explained within the centrosymmetric model. In this study, the off-axis electron holography experiment provides the key evidence of the existence of electrostatic asymmetry, see Fig 1.5(A). The electrostatic potential around a nanoscale object can be determined by evaluating the phase shift $\phi(x)$ of an electron wave that has passed through the sample, relative to the wave that has travelled through a vacuum. The magnitude of $\phi(x)$ for non-magnetic materials is proportional to the integral of the potential along a straight-line path through the specimen. While the off-axis electron holography directly provides the electrostatic potential profile of the AuNR, the measured $\phi(x)$ gradient may originate from a variety of sources. Therefore, it is important to track down each of these potential contributing sources for any meaningful conclusion.

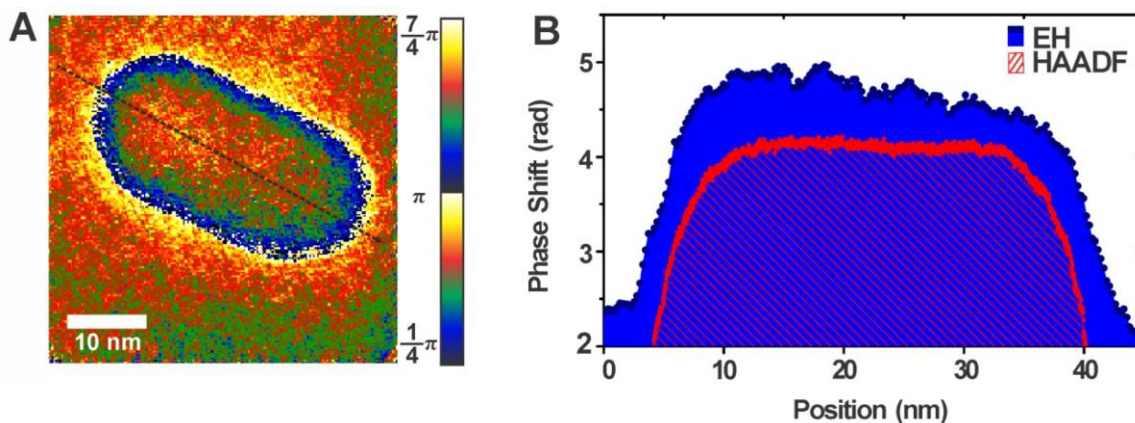


Figure 1.5 Electrostatic distribution of individual AuNRs. (A) phase map of electron holography (B) linear phase profiles of electron holography conventional (EH) and high angle angular dark field (HAADF) along the longitudinal axis of the AuNRs, supported by silicon grids. Adapted from ref ⁸.

One probable source is the variation of the NR diameter along the long axis of the AuNR. To exclude this possibility, high-angle annular dark field (HAADF) images of same NR were taken

using scanning transmission electron microscopy (STEM), as the signal intensity in HAADF is proportional to the NR diameter. As can be seen in Fig 1.5(B) (red curve), HAADF intensity profile shows no variability along the long NR axis, indicating that the gold core is axially symmetric. Another potential source of asymmetry is the variation of CTAB in the axial direction of the AuNRs. To investigate this possibility, secondary electron imaging and energy-filtered TEM (EF-TEM) were performed for the direct visualization of the organic layer distribution on the AuNR. As shown in Fig 1.6(D, F), we see no evidence of significant CTAB patchiness on the long sides of the NRs. To this end, it is therefore concluded that the gradient $\phi(x)$ profile shown in Fig. 1.5(A) reflects the potential gradient generated by charge accumulation in the CTAB-AuNR electronic system.

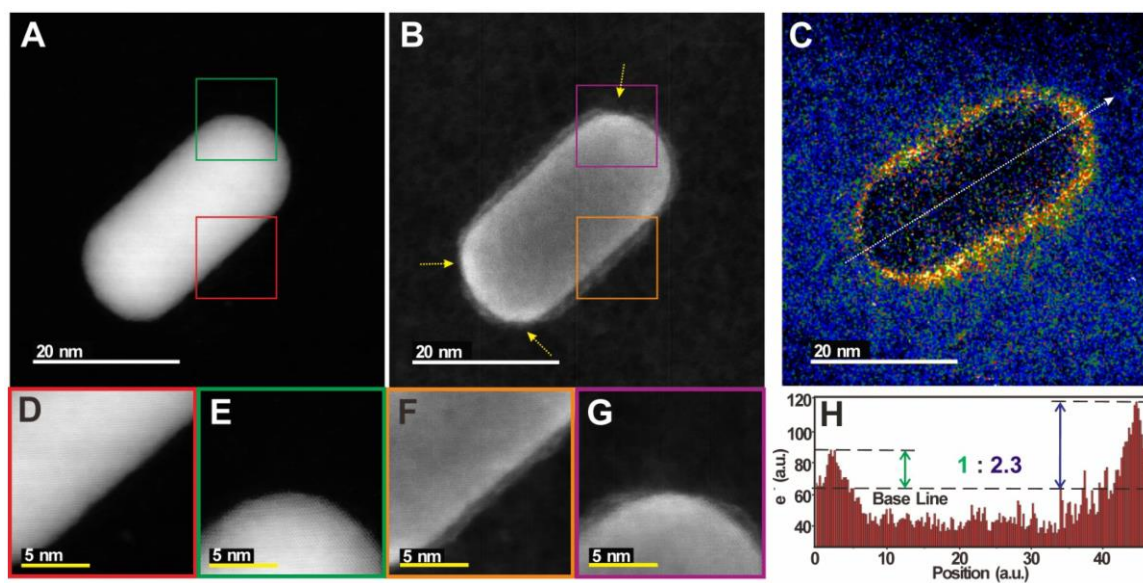


Figure 1.6 Non-centrosymmetric distribution of CTAB on AuNR. (A, D, E) STEM-HAADF and (B, F, G) SEM images for a same gold NR. (D-G) Atomic resolution images of the side (D, F) and end (E, G) sections of the AuNR. (C) Carbon element map and (H) carbon profile along the white arrow obtained by energy filtering (EF) TEM. Adapted from ref ⁸.

Within the off-axis electron holography experiment, it was constantly observed that the holograms of standard NRs stabilized by CTAB are asymmetric. Their $\phi(x)$ values display small but distinct gradients along the long axis that are consistent across multiple grid areas, separately

prepared samples, and imaging conditions. This strongly implies that, AuNRs may be centrosymmetric with respect to the atomic lattice of the gold core but non-centrosymmetric due to the organic shell surrounding the gold core.

To investigate the non-centrosymmetric distribution of CTAB on AuNR and the correlation with the asymmetric potential, a series of state-of-art microscopies were performed: (i) The Kelvin probe microscopy measures the profile of capacitance gradient, dC/dz in the AuNR, and therefore the contributions from several interfaces and materials, such as CTAB and gold, are manifested in the dC/dz map, see Fig 1.7(A, B). As can be seen, the dC/dz map vividly shows the difference between the sides and ends of a NR, which should be attributed to different CTAB density on the sides and ends, see Fig 1.6(B). (ii) The aberration-corrected STEM with a secondary electron detector enables the direct atomic-scale visualization of the CTAB layer. In Fig 1.6(A, B), one can see that the CTAB coverage on the two caps is different. (iii) Elemental mapping of carbon in the organic layer around the gold core by energy-filtered TEM (EF-TEM, Fig. 1.6C) enabled quantitative analysis of CTAB density difference between two ends. Using a supporting carbon grid as the baseline, it is shown that the NR has about 2.3 times more CTAB on one end than the other, see Fig. 1.6(H).

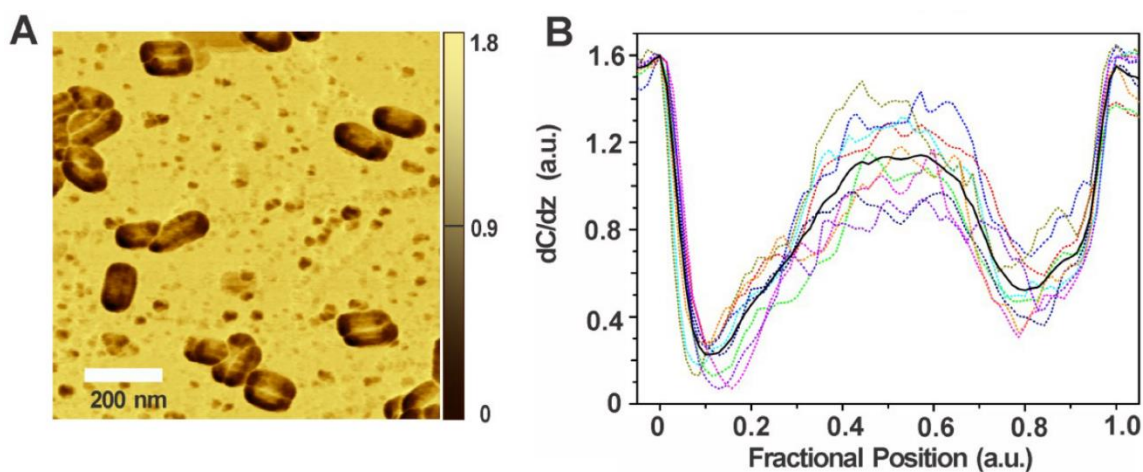


Figure 1.7 Kelvin probe microscopy. (A) Capacitance gradient (dC/dz) image and (B) line profiles and average curve (solid, black) along long axis. The visual contrast between the sides and ends of a NR results from the different associated CTAB densities. Adapted from ref ⁸.

Section 1.4 **Optical asymmetry of gold nanorods**

The NLO of the AuNRs have been extensively studied, as the understanding of their optical properties is essential for the development of the AuNR-based NLO applications. However, the electrostatic symmetry breaking of the AuNRs has never been systematically considered to explain the NLO mechanism, even if the symmetry breaking from a highly centrosymmetric nanostructure had attracted some attention.⁶² The surprisingly high hyperpolarizability values in AuNRs and the resulting strong harmonic light scattering signal were attributed to the internal charge distortions that lead to an instantaneous non-centrosymmetric electron distribution. The electrostatic asymmetry of AuNRs should induce a static dipole moment, which breaks the inversion symmetry and leads to an optical asymmetry. This can incur as a modification of the NLO properties, since for an optically symmetric nanoparticle, SHG is forbidden to lowest order, and can arise only through the effect of retardation and quadrupole radiation. The NLO thus offers an entirely different perspective on the anisotropic nature of AuNRs, as opposed to the microscopy techniques that are associated with the spatial mapping of different physical quantities such as the electric potential, the conductance gradient, and the chemical compositions as discussed in the previous section.

To investigate how the electrostatic asymmetry modifies the NLO properties, the experiment was designed to compare the NLO responses between AuNR samples with and without electrostatic asymmetry. As concluded in the previous section, the electrostatic symmetry breaking of the AuNRs is caused by the unequal number of CTAB moieties capping the two ends of the AuNRs, hence the ideal sample for the control experiment is the conventional colloidal AuNRs with only the CTAB completely removed. It turns out however, that the complete removal of CTAB from dispersed AuNRs without losing colloidal stability is difficult^{63,64}, and we therefore go a different route to prepare the samples in the solid-state form. These AuNR composite films on quartz slides allows random directionality, sufficient optical density, and controlled inter-particle spacing of AuNRs, as elaborated below. The AuNRs were purchased from Nanopartz, which have diameter 25 nm and an average length 102 nm, leading to a transverse plasmon resonance at 517 nm and longitudinal plasmon resonance at 808 nm.

To prepare the asymmetric AuNR samples, an uncharged polymer, poly(vinyl alcohol) (PVA) was chosen as polymer matrix, since it has been proven to have almost negligible affinity

to the surface of gold. PVA/AuNR film samples (asymmetric AuNRs) were then simply prepared by drop casting 1 OD of AuNR colloids re-dispersed in PVA (7.5 wt%) onto quartz slides. The average distance between AuNRs in these films was 300 nm; these gaps exceeding the AuNR dimensions by many times are sufficient to decouple transient oscillating electrical dipoles.

To prepare the symmetric AuNR samples, 1 mm thick quartz slides were first treated with piranha solution, pre-coated with one PAA/PDDA layer and finished with one poly(sodium 4-styrene sulfonate) (PSS) layer. Several bilayers of AuNR/PSS were then added by the layer-by-layer (LBL) method. During LBL deposition the rarefied layers of AuNRs anchored to the substrate by the polyelectrolyte stratum, are exposed to solution of PSS. The negatively charged polyelectrolyte draws away and strips positively charged CTAB from surface of the NRs. To gain more insight from the experiment, we prepared two types of PSS/AuNR film samples. The one with spacers of poly(acrylic acid) (PAA) and poly(diallyldimethylammonium chloride) (PDDA) added between every two bilayer of AuNR/PSS is called the *decoupled PSS/AuNR* sample, since the spacers increase the interlayer distances so that the interactions of AuNRs between layers are decoupled, see Fig 1.8. The one without the spacers is called the *coupled PSS/AuNR* sample, following the same reasoning.

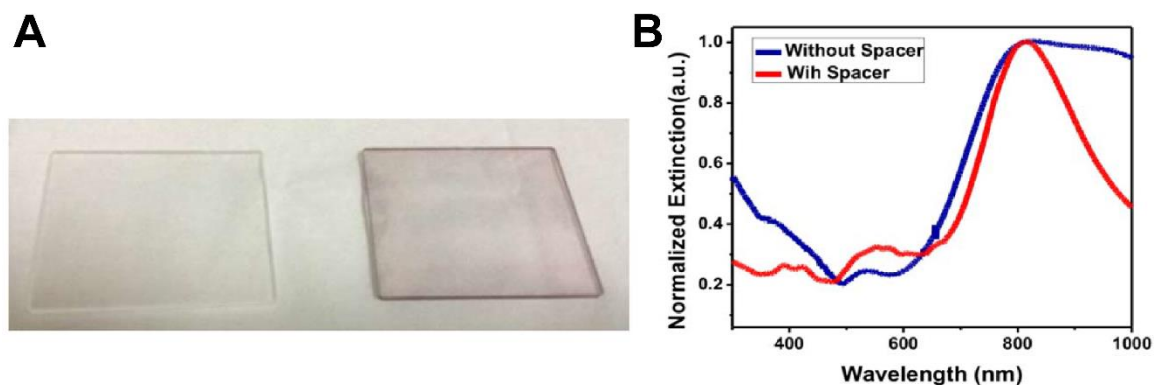


Figure 1.8 The PSS/AuNR film sample. (A) Sample picture of AuNR composite and reference polymer film on quartz slides and (B) UV-VIS spectra of AuNR composite film with/without spacer. Sample without spacer shows red-shift in the longitudinal mode, indicating the presence of end-to-end field coupling effect.

In the NLO experiment, the excitation source was a Ti:sapphire mode-locked laser which delivers 50-fs pulses with a repetition rate of 76 MHz at 800 nm, resonant with the longitudinal plasmon of the AuNRs. Different samples of AuNR film on quartz slides were excited with the focused beam, and the NLO responses were filtered through a spectrometer and then detected by a single photon counting photomultiplier to study the spectral features, where the gated photon counting technique was applied to achieve the best signal-to-noise ratio. The experimental setup is shown in Figure 2.2, and for more experimental details, please refer to Section 2.4.2 and 2.4.3. There are four types of samples used in the experiment: (i) the PVA/AuNR sample that is electrostatically asymmetric (ii) the coupled PSS/AuNR sample that is electrostatically symmetric with interlayer interaction (iii) the decoupled PSS/AuNR sample that is electrostatically symmetric without interlayer interaction and (iv) the reference films which were made for film (i)-(iii) with only polymer or polyelectrolyte components of the corresponding samples.

The NLO measurements started with all the reference film samples. There were only negligible NLO signal, indicating that the NLO responses from all the AuNR film samples, if any, result from the embedded AuNRs and are plotted in Fig 1.9. The spectra of all the AuNR film samples were normalized with their particle densities, which are approximately proportional to their measured intensities at the longitudinal plasmon resonant frequency in the UV-VIS spectra. The two principal NLO components are the second harmonic generation (SHG), located at 400 nm a broadband feature ranging from 350 to 600 nm that is referred to as the nonlinear photoluminescence (PL). The strength of the SHG signal is indicative of the system asymmetry, which can be understood based on the fact that solving the electromagnetic distribution of an asymmetric system would require the presence of the plane wave component that is frequency-doubled with respect to the excitation light source. The PL, as will be investigated in detail in the subsequent chapter, results from the second order longitudinal plasmon resonance mode scattering with the electron gas which is induced by the optical and electrostatic asymmetry.

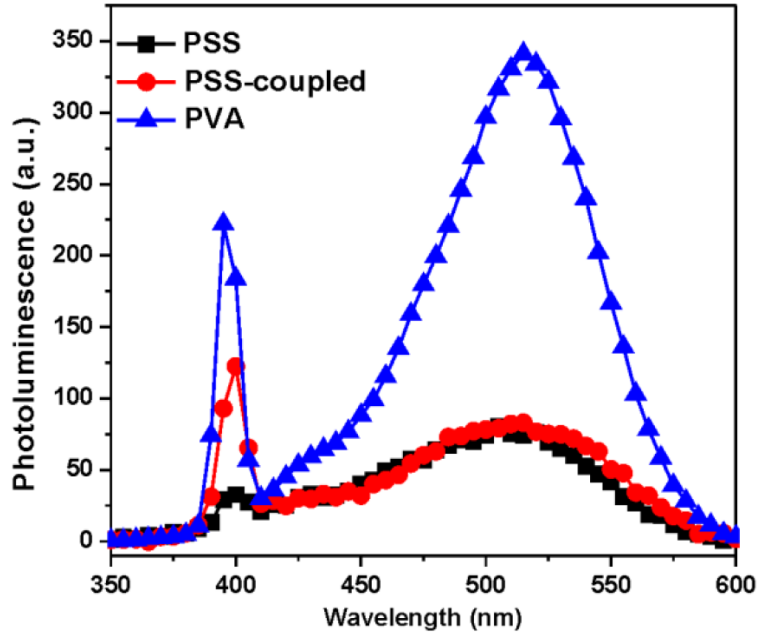


Figure 1.9 Photoluminescence and SHG from AuNRs film samples. (black) PSS-decoupled (red) PSS-coupled and (blue) PVA. The PVA sample generates the most intense SHG and PL signals, indicative of the high system asymmetry. Compared to the PSS-decoupled sample, the PSS-coupled sample generates stronger SHG signal due to the end-to-end field coupling effect. Adapted from ref ⁸.

The inferences from the experimental observations of SHG and PL signals perfectly aligned with the electrostatic properties of the corresponding AuNR film samples. Among all samples, the electrostatically asymmetric PVA/AuNR film produces the most intense SHG and PL signals. On the other hand, the complete removal of CTAB in the coupled/decoupled PSS/AuNR samples, indeed, results in strong suppression of PL. The surprisingly high SHG from the coupled PSS/AuNR compared to the decoupled PSS/AuNR samples can be explained by the strong SHG from the bowtie effect (e.g. strong SHG from the closely spaced nanoscale tips). It is well known that when two NRs are end-to-end, closely spaced, strong field coupling can occur and leads to a red-shift in the longitudinal mode. Such coupling can be verified by the UV-VIS extinction spectrum of the coupled PSS/AuNR sample, which clearly shows the red-shift in the longitudinal mode as compared to the decoupled PSS/AuNR sample, see Fig 1.8(B).

Section 1.5 Summary

While the AuNRs have long been considered as highly symmetric nanostructures based on the cylindrical geometry of their metal cores, their anisotropic nature was shown by many different of experimental observations in this study. The electrostatic asymmetry of AuNRs was confirmed with a variety of microscopy techniques, and the physical origin of this asymmetry is revealed to be associated with a constantly unequal number of CTAB moieties capping the two ends of the AuNRs. The optical asymmetry induced by the electrostatic asymmetry was revealed by the experiments of nonlinear light scattering, where the SHG and broadband PL are indicative of the system asymmetry. AuNR film samples with and without electrostatic asymmetry were prepared for the control experiments, and the corresponding NLO responses are consistent with their symmetry properties. The observed optical asymmetry is thereafter included in the consideration of the NLO mechanism, which leads to a novel microscopic model that can self-consistently explains all the main features of the NLO components and is the foundation of discussions in the next chapter.

CHAPTER 2

Optical Asymmetry and Nonlinear Light Scattering from Gold Nanorods

Section 2.1 Introduction

Metal nanoparticles and other plasmonic structures are of great interest for a wide array of applications primarily due to the presence of optical-frequency surface-plasmon modes confined to the nanostructure. Through engineering the metal sub-wavelength structure, exquisite control over the absorption, emission, and scattering of light can be achieved. Even in the model case of the simplest metal nanostructures, however, such as isolated nanorods in a uniform dielectric environment (e.g. solution), the detailed microscopic mechanism for the nonlinear optical response is a subject of controversy. In this work, we present a systematic study of the nonlinear light scattering from gold nanorods in solution, including second and third harmonic generation and multiphoton luminescence. Building on recent observations of the existence of a static dipole on the nanorods, we are able to obtain a new and complete microscopic picture of nonlinear light scattering in this system.

A systematic study is presented of the intensity-dependent nonlinear light scattering spectra of gold nanorods under resonant excitation of the longitudinal surface plasmon resonance (SPR). The spectra exhibit features due to coherent second and third harmonic generation as well as a broadband feature that has been previously attributed to multiphoton photoluminescence arising primarily from interband optical transitions in the gold. A detailed study of the spectral dependence of the scaling of the scattered light with excitation intensity shows unexpected scaling behavior of the coherent signals, which is quantitatively accounted for by optically induced damping of the SPR mode through a Fermi liquid model of the electronic scattering. The broadband feature is

shown to arise not from luminescence, but from scattering of the second-order longitudinal SPR mode with the electron gas, where efficient excitation of the 2nd order mode arises from an optical asymmetry of the nanorod. The electronic-temperature-dependent plasmon damping and the Fermi-Dirac distribution together determine the intensity dependence of the broadband emission, and the structure-dependent absorption spectrum determines the spectral shape through the fluctuation-dissipation theorem. Hence a complete self-consistent picture of both coherent and incoherent light scattering is obtained with a single set of physical parameters.

The result of this project was published in *ACS Nano* in 2017.⁶⁵ Electron holography experiments were carried out in part at the Brookhaven National Laboratory. The HAADF images and the CBED patterns were provided by NIST. I performed the nonlinear optical experiments and developed the novel microscopic model.

Section 2.2 Nonlinear light scatterings in noble nanoparticles

Nanoscale noble metal structures, such as gold and silver nanoparticles, exhibit optical and electronic properties that are not observed in their bulk counterparts. The electromagnetic modes of these systems, known as SPRs, lead to strong interaction with light, and an enhancement of the optical field enabling nonlinear effects to be observed with low incident light intensity.^{45,66} The plasmon resonances and the field enhancement can be tailored through the choice of metal, the specific size and shape, the dielectric environment, and their mutual spatial arrangement.^{44,67,68} In fact, the sensitivity of the resonances to the local dielectric and charge environment enables the SPR to serve as an optical interrogation of the environment and thus as an optical sensor. The attachment of chemical ligands enables selective sensing of chemical or biomedical targets. As a result, metal nanoparticles serve as important building blocks in the fields of modern chemical engineering,⁶⁹ biosensors⁷⁰ and advanced microscopy.^{47,48,71} A fundamental understanding of the nonlinear optical response of metal nanostructures is thus essential for the development of optical applications of plasmonics.

The two principal nonlinear optical responses that can be observed on direct far-field excitation are multi-photon luminescence (PL) and harmonic generation (HG). Both phenomena have been investigated extensively. Early observations of two-photon luminescence (TPL) were

reported by Boyd et al.,⁷² and interpreted as the generation and recombination of electron–hole pairs involving the d-band and the conduction (sp) band. The luminescence efficiency of gold nanoparticles can be remarkably high,⁷³ suggesting applications to biological labeling and imaging.⁷⁴ More recently, harmonic generation from metal nanoparticles has received considerable attention. Lippitz et al. reported the first observation of third-harmonic generation (THG) from individual gold colloidal particles down to 40 nm diameter,⁷⁵ and third harmonic imaging experiments with gold nanorods was demonstrated;⁷⁶ SHG from gold nanorods was also investigated in ref.⁶² A phenomenological theory of second harmonic generation (SHG) from centrosymmetric spherical metallic particles was developed by J. I. Dadap et al.^{77,78} Starting with the second order nonlinear surface susceptibilities, they presented a general electro-magnetic theory of SH Rayleigh scattering (SHRS) for spheres within the small particle limit, including the contribution from the bulk nonlinear response compatible with isotropic symmetry. They predicted a quadrupolar-type radiation pattern, as the second order process is in principle dipole-forbidden in centrosymmetric material with centrosymmetric geometry, consistent with experimental results on hyper-Rayleigh scattering from silver nanospheres reported by Hao et al.⁷⁹ and a series of polarization analysis experiments performed by Brevet et al.^{80–82}

Section 2.3 The anisotropic nature of gold nanorods

Among the most common forms of structure used for studies of nanoplasmonics are chemically synthesized AuNRs, grown in aqueous solution guided by the surfactant cetyltrimethylammonium bromide (CTAB).⁸³ These structures exhibit a high degree of structural symmetry and crystallinity, as can be seen from the atomic-resolution high-angle annular dark-field images and convergent beam electron diffraction pattern of a single AuNR of the sample used in these experiments in Fig. 2.1(a, b). A spatial analysis of the electrostatic potential around the AuNRs was recently performed using off-axis electron holography.⁸⁴ In the absence of magnetic field, the phase shift $\phi(x, y)$ in an electron wave after passing through a specimen is proportional to a line integral of the electrostatic potential along the propagation direction.⁸⁵ The reconstructed phase shift $\phi(x, y)$ map obtained for a AuNR shows a considerable asymmetry and a distinctive slope along the long axis of the rod as seen in Fig. 2.1(c, d), indicating the presence of a static dipole moment. In a recent companion study,⁸⁶ we have found that non-uniform coverage of the

surfactant CTAB induces a static dipole moment, which breaks the inversion symmetry and leads to an optical asymmetry. This has far-reaching consequences, since for an optically symmetric nanoparticle, SHG is forbidden to lowest order, and can arise only through the effect of retardation and quadrupole radiation. Motivated by these considerations, we seek to answer the two questions (i) Can we observed the anisotropy of the gold nanorods optically? (ii) How does such anisotropy affect their photonic properties? We will show in the following of this study that, the optical symmetry breaking by the static dipole in AuNRs enables a quantitative and self-consistent explanation of all the major features of nonlinear light scattering.

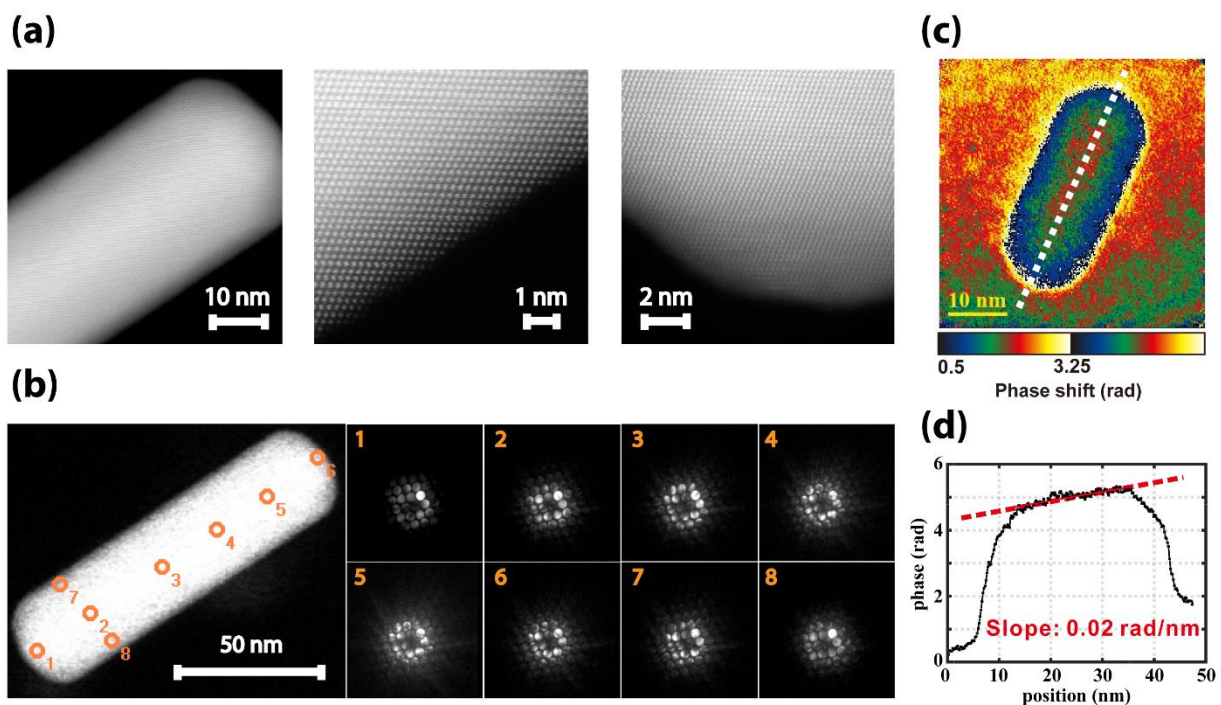


Figure 2.1 Structural symmetry and electrostatic asymmetry of AuNR. (a) Atomic-resolution high-angle annular dark-field (HAADF) images of a single AuNR used in the optical experiment and (b) convergent beam electron diffraction (CBED) pattern collected with beam positioned at various locations (orange markers) in the AuNR. Results indicated consistent structure in all areas of the rod and showed the high degree of structural symmetry of the AuNRs. (c) False-color reconstructed phase shift image and (d) its line profile along the long axis (white dashed line in d) of the AuNR. Adapted from ref ⁶⁵.

Section 2.4 Experimental Procedures

Section 2.4.1 Experimental setup

Figure 2.4(a) displays a typical light scattering spectrum from a dilute colloidal AuNR sample under excitation from ultrashort laser pulses at 800 nm; the spectra exhibit resonant features at the second and third harmonic wavelengths, as well as a broadband component. We present here the experimental details for the spectral and intensity dependence study on the nonlinear light scattering from AuNRs.

The experimental setup is shown in Figure 2.2. The excitation source is a Ti:sapphire mode-locked laser, which provides 800-nm, 50-fs pulses at a repetition rate of 76 MHz. The excitation power is controlled by a variable attenuator consisting of a half-wave plate mounted on a programmable rotator and a Glan-Thompson polarizer. The laser pulses pass through a prism compressor so that the pulses are transform-limited at the focal point. A small fraction of the beam is sampled by a photodiode in order to measure the incident power and its fluctuations. In addition, a 780 nm high-pass filter is placed before the focusing lens to ensure there is no residual SHG or THG in the excitation beam. The beam is focused in the center of a cuvette containing an aqueous solution of AuNRs with a longitudinal plasmon resonance at 808 nm. Light scattered at 90° from the excitation direction is collected by an $f^{\#}=1$ uv-coated lens and filtered through either Blue-Green (BG) filters (BG-39, BG-40 color filters) or 267 nm band-pass filters to remove the linear 800 nm scattering. The collected signal is focused on the entrance slit of a monochromator and detected by a single photon counting photomultiplier. A chopper is placed in the excitation beam path to modulate the excitation beam in order to subtract background dark counts from the signal in gated photon counting mode.

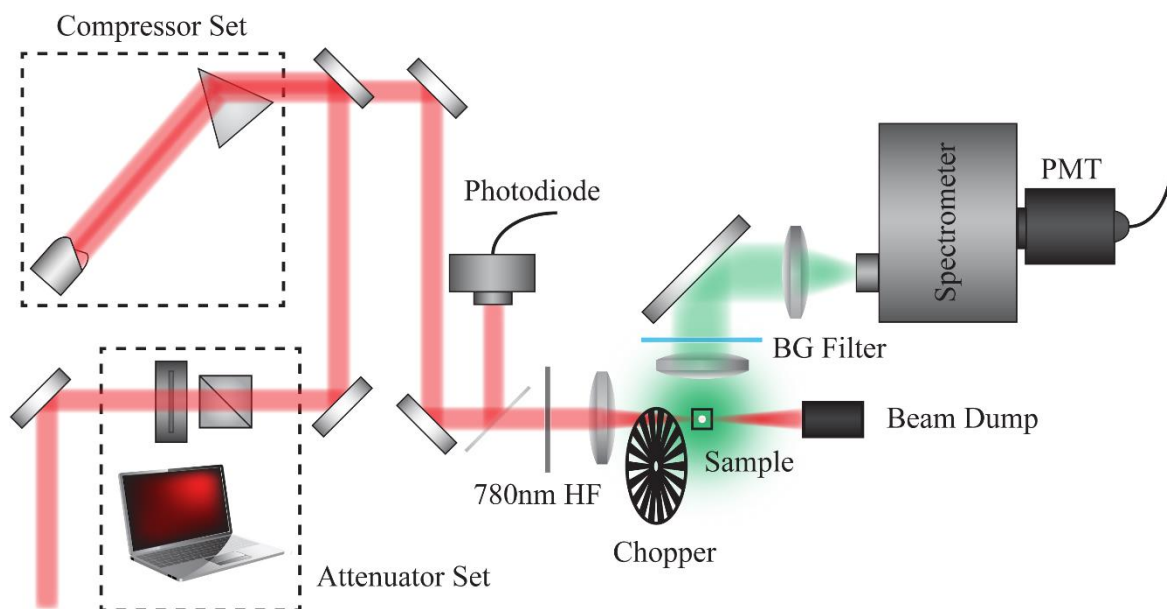


Figure 2.2 The experimental setup for the study on the nonlinear light scattering from AuNRs. The dynamic sampling of optical signal for the defined SNR is enabled by the programmable attenuator set; spectral and intensity dependence studies were performed. Adapted from ref ⁶⁵.

Section 2.4.2 Gold nanorod characterization

The data presented in this study are from samples consisting of aqueous solutions of AuNRs purchased from Nanopartz. The solution concentration is approximately 1 nM, sufficiently low that particle interaction effects are negligible. The AuNRs have diameter 25 nm and an average length 102 nm, leading to a transverse plasmon resonance at 517 nm and longitudinal plasmon resonance at 808 nm. The longitudinal plasmon resonance is typically inhomogeneously broadened due to residual fluctuations in the nanorod length, but it should be noted that the excitation light only interacts with nanorods having plasmon resonances close to the excitation wavelength; this was verified by control experiments showing that the signals disappeared when using samples with longitudinal plasmon energies away from resonance.

In the optical experiments, we ruled out the possibility of rod melting by monitoring the difference between the initial and final UV-VIS spectra of the gold nanorod solution sample. Gold nanorods in solution can be melted into spherical nanoparticles by excitation with intense

femtosecond laser pulses of sufficient energy. If the energy absorbed by the rods are strong enough such that the rods are partially melted before diffusing out of the focal volume, the longitudinal absorption band would blue-shift, as the aspect ratio of the rods would decrease. If the absorbed energy is even larger such that the rods completely melt into spheres before diffusing out of the focal volume, the intensity of the longitudinal absorption band would decrease, while the intensity of the transverse absorption band would increase, suggesting the depletion of the gold nanorods and the formation of spherical nanoparticles. This phenomenon has previously been observed and reported as a valid method to monitor the rod shape change.⁸⁷ Indeed, even with the most intense excitation in our experiment, no blue-shift or the decrement of the longitudinal absorption intensity in the final UV-VIS spectrum was observed, indicating that no rod melting occurred.

Section 2.4.3 Extraction of intensity dependence

While obtaining the spectrum is straight forward, a precise measurement on the intensity dependence is more challenging, especially since these nonlinear responses are generally weak. Here we developed a procedure based on statistical analysis to precisely define the uncertainty of the intensity dependence measurements. The measurement of the intensity scaling corresponds to the determination of γ from $y = ax^\gamma$ where y represents the optical signal and x represents the excitation intensity. The task is essentially the extraction of the fitted linear slope from the data points in a log-log plot, which must be performed in such a way as to obtain a well-defined error in the determined scaling coefficient. Consider several data points measured with increasing incident intensities. The integration time at each incident intensity is varied to control the error bar on each of the data points, such that the error bars on the log-log plot have equal width. This can be achieved by making the signal-noise-ratio (SNR) the same at every data point via the number of measurements at each data point. Let μ be the population mean, \bar{x} be the sample mean, σ^2 be population variance and s^2 be sample variance. With n samples, we have

$$\mu = \bar{x} \pm t_{n-1} \frac{s}{\sqrt{n}} = \bar{x} \pm \Delta x$$

for 95% confidence under t-distribution, and we define $SNR = K = \bar{x}/\Delta x$. Now \bar{x} and s can be obtained through measurements and the estimated number of samplings n to reach the desired

$SNR = K$ is $n = \left[\frac{K \cdot t_{n-1} s}{\bar{x}} \right]^2$. With these definitions, we developed the following procedure to reach a desired $SNR = K$:

1. Take $n_0 = 10$ measurements and calculate \bar{x}_{10} and s_{10} . In our case we collect photon counts in 5 sec segments for 10 times.
2. Compare $K_{10} = \bar{x}_{10}/t_{10-1} \frac{s_{10}}{\sqrt{10}}$ to the desired SNR, K , where $t_9 = 2.262$. If $K_{10} > K$, we conclude that the desired SNR is reached and take \bar{x}_{10} as the signal count rate.
3. If $K_{10} < K$, we enlarge n_1 by $n_1 = \left[\frac{K \cdot t_{10-1} s_{10}}{\bar{x}_{10}} \right]^2$
4. Take the additional $n_1 - n_0$ points. Calculate \bar{x}_{n_1}, s_{n_1} and K_{n_1} . Note \bar{x}_n and s_n will converge as $n \rightarrow \infty$.
5. Repeat 2 – 4.

The procedure ensures that on each data point, the error bars on the log-log plot are with equal width $\log \frac{K+1}{K-1}$, hence minimizing the variance of the extracted fitted linear slope on the log-log plot.

Now we define the precision. When graphing $y = ax^\gamma$ in log-log plot, it becomes linear and the slope represents γ , the intensity dependence information. At every point, we have control on the error bar so that $\frac{K-1}{K} y_i \leq y_i \leq \frac{K+1}{K} y_i$ where y_i is the signal at i^{th} data point. In a log-log plot, it corresponds to $\log \frac{K-1}{K} + \log y_i \leq \log y_i \leq \log \frac{K+1}{K} + \log y_i$. Hence in log-log plot, the width of error bar is $\log \frac{K+1}{K} - \log \frac{K-1}{K} = \log \frac{K+1}{K-1}$ which is invariant to x . This qualifies the use of the simple linear regression model: for $y_i = \beta_0 + \beta_1 x_i + \varepsilon$, $\varepsilon \sim N(0, \sigma^2)$ where β_0 and β_1 are the estimators, $Var(\beta_1) = \sigma^2/S_{xx}$ and $S_{xx} = \sum_i (x_i - \bar{x})^2$.

To see the influence on $Var(\beta_1)$ from dynamic range and number of points, assume a total of $N + 1$ points starting at x_0 across the range R . With some derivation, we get

$$Var(\beta_1) = \sigma^2/S_{xx} = \frac{6N\sigma^2}{(N+1)(N+2)R^2}.$$

Since we use the 95% confidence standard, the relationship between K and σ is $\log \frac{K+1}{K-1} = 4\sigma$ and we complete the work to relate dynamic range, local SNR of each point, and number of points to the variance of γ , the extraction of intensity dependence.

As a test case, we applied the procedure on 9 intensity dependence measurements of Rhodamine 6G, which is known to have a quadratic scaling. The estimation of uncertainty with 95% confidence from our developed expression is 0.0073 and the true statistics shows 0.0061, see Fig 2.3. This verified the effectiveness of the procedure.

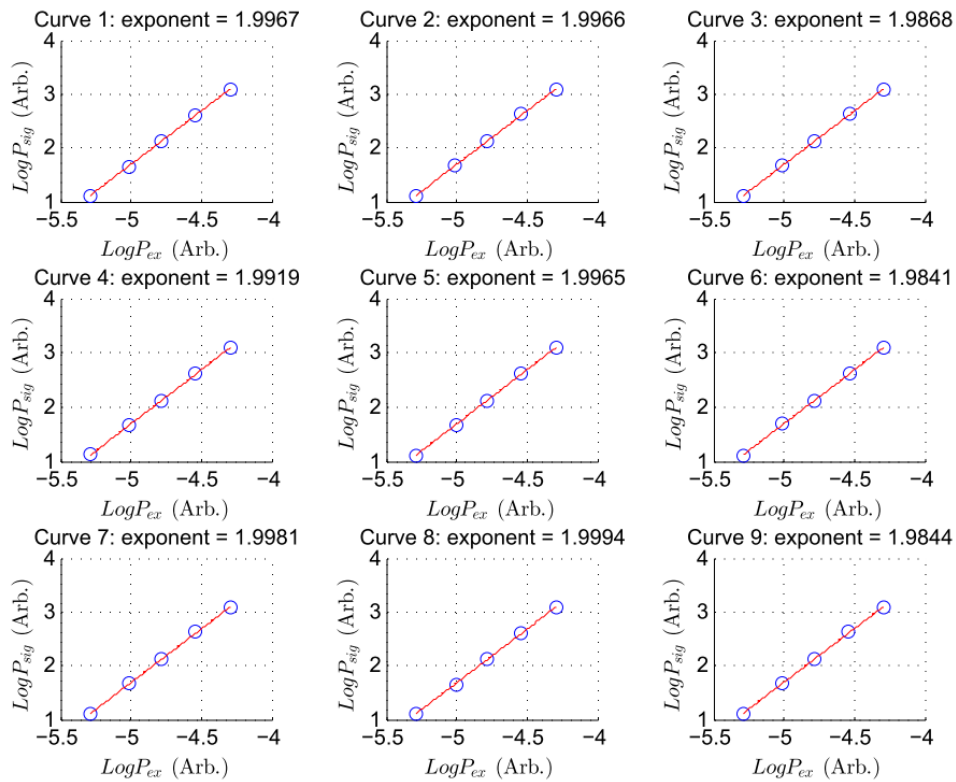


Figure 2.3 Intensity dependence measurements of Rhodamine 6G. The measurements serve as the validation of our statistical analysis and the proposed sampling strategy.

Section 2.5 The nonconventional scaling of HG

Section 2.5.1 Previous works and the experimental results

Over the past decades, the nonlinear optics (THG and SHG) of metal nanoparticles has been vastly studied. Specifically for gold nanorods, the two most important original works for the THG and SHG are ⁷⁶ and ⁸⁸, respectively. The first observation and characterization of THG was performed in ⁷⁶. The work is closely related to ours as their experimental conditions are similar, including the excitation source (both Ti:sapphire mode-locked laser with a repetition rate in sub-100 MHz and a pulse duration of 100 fs at around 798 nm) and sample (both water suspension of nanorods with size about 25×100 nm). The measured THG spectrum is background free, and the dependence of the THG signal on illuminating intensity was reported, which showed a saturation-like behavior. Instead of investigating in depth, they simply attributed it to the possible thermal effects and partial melting of nanorods and did not provide the error bar on the measured intensity scaling.

On the other hand, while there were previously abundant literatures on the SHG from gold nanosphere due to the interest to investigate the system of centrosymmetric structure and material, the study of SHG from gold nanorods first appeared in ⁸⁸. Instead of water suspension of gold nanorods, their nanostructures were fabricated by electron beam lithography through the lift-off method. On the spectrum, the SHG peak is mixed with the background broadband luminescence and they reported the extracted exponent to be 1.9. While it is close to the ideal value of 2 from the perturbative nonlinear optics, their intensity dependence measurement includes both the spectral components of SHG peak and the background broadband luminescence underneath. In principle, they originate from different physical processes (SHG is coherent and the broadband luminescence is incoherent) and should not be considered as a combined quantity. Separation of the two spectral components for the correct calculation of intensity scaling is a subtle subject and will be discussed in more detail in the following.

Now we discuss on the experimental results. A typical spectrum of the nonlinearly scattered light is shown in Figure 2.4(a), showing clearly three main components: THG and SHG peaks (hyper-Rayleigh scattering) located at 267 nm and 400 nm, respectively, and a broadband feature ranging from 350 nm to 600 nm that is generally referred to as PL. Figure 2.4(b) and 2.4(c) shows the measured scaling of the SHG and THG peaks. On the basis of the standard perturbation

theory of nonlinear optics,⁸⁹ the SHG should scale exactly as the square of the intensity, and the THG as the cube.

The THG signal has a well-defined spectral peak and is background-free (Figure 2.4 inset). A fit to a scaling curve of the form $I_{sig} = a(I_{ex})^b$ yields an exponent of $2.46 (\pm 0.022)$, quite different from the expected value of 3. The SHG peak sits on top of the broad PL background. To determine the SHG scaling, we subtract the PL before integrating the area under the 400-nm peak (the assumption that the PL spectrum is smooth is fully justified by the model below). The background-subtracted SHG scales with an exponent of 1.49 ± 0.03 , far from its conventional expected value of 2.

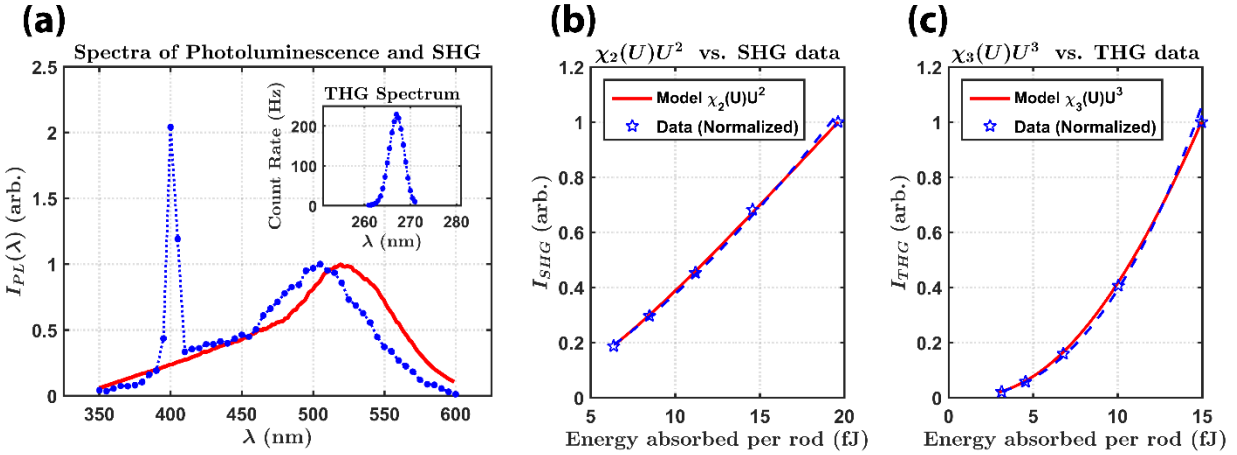


Figure 2.4 Nonlinear optical response on resonant excitation with 800-nm ultrashort pulses. (a) the spectral components include SHG, THG (inset) and a broadband PL. The red curve is the calculated spectrum with the proposed model (b) the unconventional intensity scaling of SHG (with the background PL subtracted) and (c) THG (background free). The blue dashed lines are the exponential fittings of the data and the red curves are the calculated SHG and THG with optically induced damping of the longitudinal SPR model. Notice the red curves fit the data better than the exponential fitting. Adapted from ref⁶⁵.

Section 2.5.2 HG with optically induced plasmon damping

Nonlinear optical processes are often described using an expansion of the nonlinear susceptibility in powers of the optical field.⁸⁹ In the strict limits of $\chi^{(2)}$ and $\chi^{(3)}$, the SHG and THG signals must respectively scale quadratically and cubically with the intensity. The unexpected

scaling of the SHG and THG signals at even the lowest fluence can be seen as a breakdown of this approximation. Nevertheless, the discrepancy of this scaling can be explained quantitatively within this framework by the optically induced damping of the longitudinal SPR by hot electrons.^{90,91} In a model of the SPR mode of the AuNR as a classical anharmonic oscillator, the second and third order nonlinear susceptibilities $\chi^{(2)}$ and $\chi^{(3)}$ are related to the linear susceptibility $\chi^{(1)}$ by

$$\chi^{(2)}(\omega) \propto \chi^{(1)}(2\omega)[\chi^{(1)}(\omega)]^2 \text{ and } \chi^{(3)}(\omega) \propto \chi^{(1)}(3\omega)[\chi^{(1)}(\omega)]^3 \text{ where}$$

$$\chi^{(1)}(\omega) = \frac{N(e^2/m)}{\epsilon_0 D(\omega)}, D(\omega) = \omega_0^2 - \omega^2 - 2i\omega\gamma$$

and ω_0 is the material resonance frequency

The factor $D(\omega)$ contains the resonance frequency of the system (corresponding to 808 nm wavelength for the longitudinal plasmon mode of the AuNR) and the damping rate γ . It has been shown that scattering of the nanoparticle plasmon from single-particle excitations of the electron gas is the dominant nonlinearity in the optical response, as γ depends on the electron temperature.⁹¹ Following the Fermi liquid model of ref,⁹¹ we find the intensity scaling will be modified by the pump-induced electron heating according to $I_{SHG} \propto \chi^{(2)}(\omega)I^2 \propto [I/\gamma_p]^2$ and

$$I_{THG} \propto \chi^{(3)}(\omega)I^3 \propto [I/\gamma_p]^3 \text{ where}$$

$$\gamma_p \propto \langle \gamma_{ee} \rangle = \frac{\int_0^\infty f(\epsilon)\gamma_{ee}(\epsilon)d\epsilon}{\int_0^\infty f(\epsilon)d\epsilon} \text{ is the total electron-temperature-dependent scattering rate and}$$

$$\gamma_{ee}(\epsilon, T_e) = \gamma_0 + \frac{K(\pi k_B T_e)^2 + (\epsilon - \epsilon_F)^2}{1 + \exp[-(\epsilon - \epsilon_F)/k_B T_e]}$$

where T_e can be further related to the absorbed energy U_{abs} per AuNR with the knowledge of the electronic heat capacity of gold C_e ⁹².

For the data presented in Figure 2.4(b) and 2.4(c), we excited the AuNRs with increasing powers $\hat{x} = (x_1, x_2, \dots, x_5)$ and measured the SHG(THG) signal powers to be $\hat{y} = (y_1, y_2, \dots, y_5)$. The absorbed energy per rod is associated with these excitation powers through $\hat{U}_{abs} = c\hat{x}$, where c is a scalar. Now using the equations above, we can fit $(\hat{x}/\hat{\gamma}_p)^n$ to \hat{y} (with normalization), where

$\hat{\gamma}_p$ is a function of \hat{U}_{abs} , $n = 2,3$ for SHG and THG respectively. Note the operation of division and exponent are element-wise. The model therefore has only two fitting parameters, namely γ_0 , the electronic-temperature-independent part of γ_{ee} , and c , the scalar that relates the excitation powers (\hat{x}) to the absorbed energy per rod (\hat{U}_{abs}). The SHG and THG scaling fit the model very well (data fits are 1.49, 2.46 and the model predictions are 1.47, 2.41 for SHG and THG respectively) for a single value of $\gamma_0 = 0.067$ (fs^{-1}) and $U_{abs} \approx 0.267U_{th}$, where U_{th} is the absorbed energy estimated from the estimated incident intensity and a classical model of the absorption cross section of a AuNR.⁶⁸ In fact, it can be seen in Figure 2.4(b) and 2.4(c) that the Fermi liquid model fits the scaling data better than an assumed power law scaling $\hat{y} = a\hat{x}^b$, which also has two fitting parameters of a and b . We conclude that the SPR damping induced by a hot thermal distribution of single-particle excitations quantitatively accounts for the unexpected scaling of the nonlinear optical response of the AuNR longitudinal plasmon resonance.

Section 2.6 Origin of the broadband photoluminescence

Section 2.6.1 Previous works and the experimental results

We now discuss the broadband scattered light, which has generally been attributed to PL arising from the recombination of d-band holes with conduction band electrons excited by multiphoton absorption in prior work. Our key experiment is the measurement of the complete spectral dependence of the intensity scaling of the broadband emission, as shown in Figure 2.5(b). The scattered light scales with an exponent of approximately 3.6 at 375 nm to 2.5 above 550 nm; *i.e.* the shorter wavelength emission exhibits a more highly nonlinear behavior. Interestingly, the total signal at 400 nm (*i.e.* the sum of the coherent SHG and the broadband signal) does not follow the general trend, but scales with an exponent of 1.92.

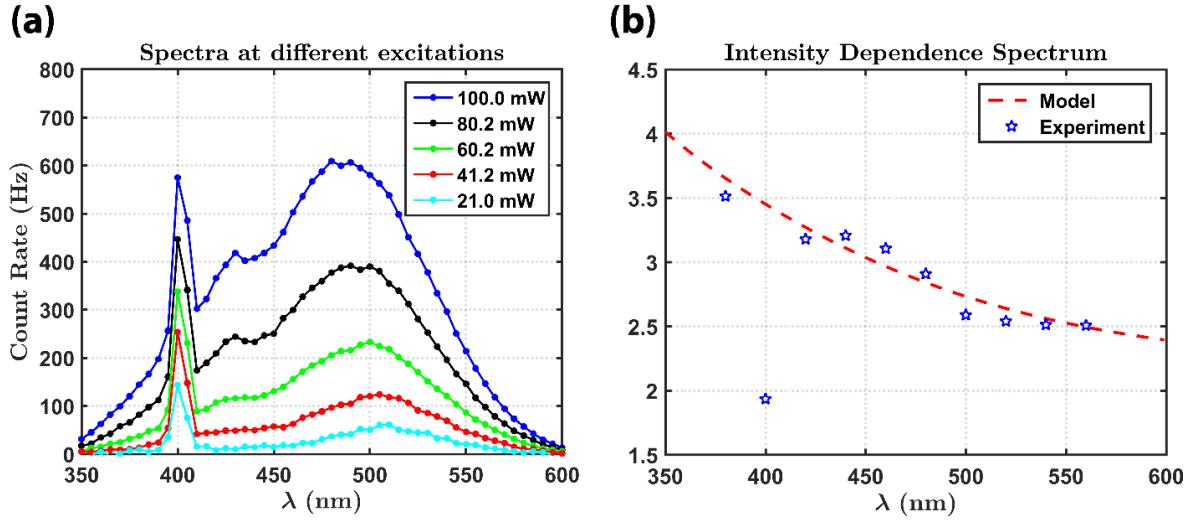


Figure 2.5 Measurement of the spectral dependence of the intensity scaling of the PL. (a) The spectra of nonlinear optical responses measured at different excitation intensities (b) The spectrally resolved intensity dependent scaling. Notice the scaling at 400 nm is close to 2. The red dash curve is generated from the proposed model. Adapted from ref⁶⁵.

While multiphoton PL from interband transitions can account for some features of the spectrum,^{48,73,93} others are inconsistent with PL as the source of the broadband emission. In particular, the spectral features of the broadband spectrum from AuNRs do not really match well with those from their bulk counterpart, though some previous work has attempted to attribute these features to recombination processes between conduction band electrons and d-band holes near the X and L symmetry points in the Brillouin zone.^{48,94–96} Recent experiments comparing PL from gold nanoantennas fabricated from single crystals and polycrystalline films, however, have suggested that it is the nanoscale geometry of the plasmonic structures that determines the shape of the emission spectra,⁹⁷ and not the band structure. Other recent work on PL from plasmonic metals also suggests that scattering from electronic excitations rather than traditional luminescence is responsible for light emission.⁹⁸ We therefore performed an additional set of experiments in which the AuNRs were excited directly with 400-nm 50-fs pulses (generated by frequency doubling the Ti:sapphire laser), which should induce one-photon absorption energetically equivalent to 2-photon absorption at 800 nm. The threshold for absorption from the d bands in Au is 1.8 eV; hence 800-nm excitation from the d-band requires two- or three-photon absorption, while linear absorption of 400-nm light can excite d-band holes. We found there was only

negligible emission from the AuNRs under 400-nm excitation even at the highest accessible excitation intensity; this indicates unequivocally that the broadband emission under 800-nm excitation does not arise from interband transitions as is usually thought.

Section 2.6.2 **Novel physical model for the broadband photoluminescence**

Given that the broadband emission is not in fact interband PL, we propose a model in which the nonlinear light scattering arises from an interplay of the plasmon damping and the optical anisotropy due to the presence of a static dipole on the AuNRs. On illumination with 800-nm pulses, the gold nanorod's longitudinal plasmon mode, corresponding to a collective oscillation of the electrons along the long axis of the particle, is resonantly excited. The charge asymmetry associated with the static dipole along the nanorod axis gives rise to a nonzero $\chi^{(2)}$; the second-order nonlinear polarization along the nanorod axis excites the asymmetric second-order longitudinal plasmon mode, which can efficiently scatter with the background free electron gas just as the fundamental plasmon mode scatters, as described above.

The process is illustrated in Figure 2.6(a), indicating how two longitudinal plasmons excited by the pump give rise to a fluctuating polarization P_ω due to scattering from the free electron gas. Electrons oscillating in opposite directions in the asymmetric second-order longitudinal mode scatter with free carriers, producing dipole fluctuations along the transverse nanorod axis, see Figure 2.6(a) inset. The emission arises as radiation from P_ω , and the coupling of these dipole fluctuations to free-space electromagnetic modes is enhanced by the transverse plasmon mode of the AuNRs. As illustrated in Figure 2.6(a), a continuum of radiation is produced since the scattering of an electron with initial energy $\varepsilon - \Delta/2$ to a final state with energy $\varepsilon + \Delta/2$ results in a shift Δ of the emission relative to the second harmonic of the 800-nm excitation; the broadband spectrum arises from an integral over all possible initial and final free-carrier states with occupations f_i and f_f determined by the Fermi function for a carrier gas with electron temperature T_e , which is well-known from the scaling experiments on SHG and THG discussed above. Since the nonlinear light scattering is driven by scattering of plasmons from free carriers, the total emission should be proportional to the plasmonic damping rate, $\gamma_p \propto \langle \gamma_{ee} \rangle$. Finally, the spectrum of scattered light is generally determined by the Fourier transform of the dipole-dipole correlation function.⁹⁹ By the fluctuation-dissipation theorem, this correlation function is

proportional to the imaginary part of the susceptibility, i.e. the absorption spectrum.^{99–101} Physically, the scattering-induced fluctuations in the polarization radiate with a strength proportional to the absorption spectrum. This effect is included by incorporating a lineshape factor $L(\omega)$ which is obtained from the actual experimental absorption spectrum of the AuNR sample. Putting all these elements together, the broadband scattered light will be given by the expression

$$I(\lambda, U) = I(\omega, T_e) \propto \int f(\varepsilon - \Delta/2)[1 - f(\varepsilon + \Delta/2)] d\varepsilon \cdot \gamma_{ee}(T_e) \cdot L(\omega)$$

$$\text{where } \Delta = 2\hbar\omega_{800 \text{ nm}} - \hbar\omega \text{ and } f(\varepsilon) = \frac{1}{1 + \exp\left(\frac{\varepsilon - \varepsilon_F}{k_B T_e}\right)}$$

is the Fermi function with electron temperature $T_e(U)$.

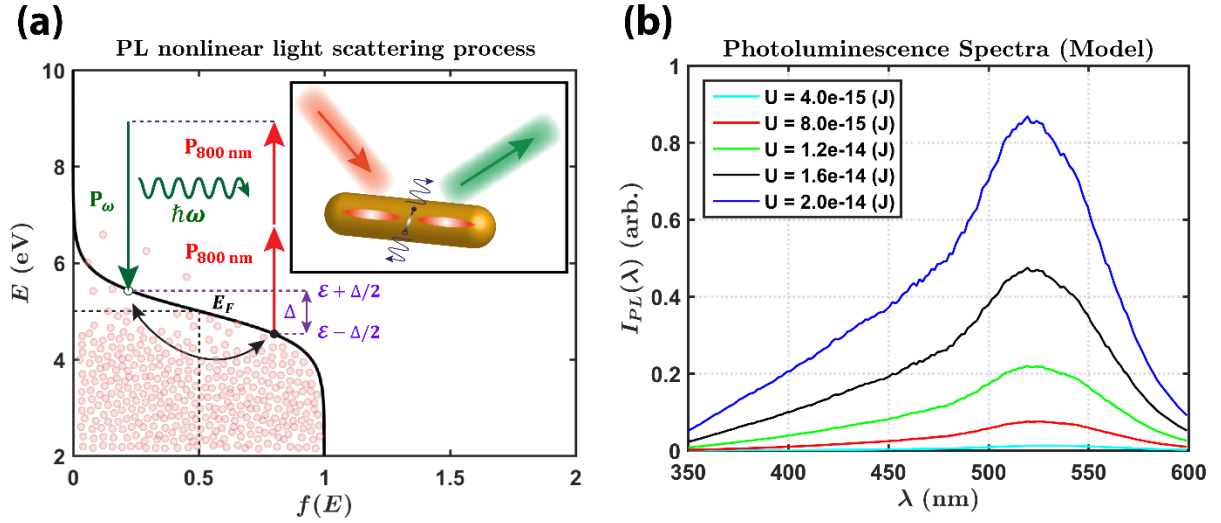


Figure 2.6 Picture of the PL nonlinear light scattering process and the reproduced PL spectra. (a) Energy diagram of the PL nonlinear light scattering process and (inset) a physical illustration of the 2nd order plasmon excitation and the PL generation. (b) Calculated scattered light spectrum using the values of γ_{ee} and U_{abs} obtained from the SHG and THG experiments. The spectral line shape is determined by the (structure dependent) absorption spectrum of AuNRs, i.e., the measured UV-VIS spectrum. Adapted from ref⁶⁵.

Figure 2.6(b) shows the calculated scattered light spectrum using the values of γ_{ee} and U_{abs} obtained from the SHG and THG experiments; Figure 2.4(a) shows the close match of the theory (red line) and experimental (blue dots) line shapes. Note that the spectral smoothness around the SHG position justifies the interpolation and subtraction of the background from the SHG peak

around 400 nm discussed above. Most critically, we can also generate from the calculation the intensity scaling as a function of wavelength; the result shown as the red curve in Figure 2.5(b), and shows excellent agreement with the data. This is a strong confirmation of the model, indicating that interband PL processes do not play a significant role in the multiphoton broadband emission, but that second-order nonlinear light scattering mediated by damping of the second-order longitudinal plasmon resonance is mainly responsible for the scattered light. It should be noted the only fitting parameter in the calculation is the value of the Fermi level; the fitting leads to $\epsilon_F = 5.4$ (eV), which is very close to the bulk value of 5.5 (eV), and the slight difference may be due to pump-induced heating. A final confirmation that the second-order light scattering mechanism described above is correct is the observation that excitation at 400 nm only leads to negligible broadband emission; excitation at 400 nm does not induce an excitation of the second order plasmon mode which could then scatter into a fluctuating dipole transverse to the nanorod.

Section 2.7 Summary

We have systematically investigated nonlinear light scattering from AuNRs under resonant excitation of the longitudinal plasmon mode, with detailed measurements of the spectral dependence of the intensity scaling across the SHG, THG, and broadband components. From our recent electron holography study (reported elsewhere), we know that the structurally symmetric gold nanorods are in fact electrically and optically anisotropic due to asymmetric charge distributions induced by the ligands used to guide their self-assembly. This optical asymmetry leads to strong second-order polarizability $\chi^{(2)}$ and hence the significant SHG signal. The SHG and THG nonlinear susceptibilities are intensity dependent, through the optically induced damping of the SPR linear susceptibility, corresponding to scattering of the plasmon with hot electrons; this damping is quantitatively understood through the electron temperature dependence in the Fermi liquid model. Because of the nonzero $\chi^{(2)}$, the second-order longitudinal mode is excited. Scattering of this mode from the electron gas results in a fluctuating polarization along the transverse direction of the nanorod, which radiates a broadband spectrum. The spectrum as well as the intensity scaling are understood through a self-consistent model of light scattering. Interband transition processes apparently play no significant role in the light emission. We note finally that the model incorporates the actual SPR spectrum through the fluctuation-dissipation theorem and

assumes scattering from a perfectly thermalized electron gas, and hence does not account for the individual microscopic scattering processes responsible for the radiation. It thus cannot account for the possible role of coherence in the scattering process, which may be important for the complete interpretation of the emission around 400 nm; the nearly quadratic scaling of the total signal at 400 nm (SHG + broadband component) is highly suggestive, and remains the subject for additional study.

CHAPTER 3

Controlling Light Transmission Through Highly Scattering Media

Section 3.1 Introduction

Light scattering in complex media was long thought to be the limiting factor for the ultimate penetration depth and resolution of all optical methods. Indeed, even with the most advanced multi-photon microscope, the typical penetration depth in biological tissue is less than a millimeter.¹⁰² The last decade however has witnessed tremendous advances in techniques for focusing light that pass through complex media with wavefront shaping applied on incident fields. The key enabling technology is the spatial light modulator (SLM) that can compensate for scattering phenomena to produce light focused onto a point inside or beyond the scattering medium, and its use was first demonstrated by Vellekoop et al.¹⁰³ The ability to focus light through highly scattering random media at a desired location can significantly contribute to various fields, and exciting applications have been demonstrated, such as fiber endoscopic and fluorescence endomicroscopy,¹⁰⁴ optical trapping,¹⁰⁵ super resolution imaging,^{106,107} and nano-positioning.¹⁰⁸

While SLM serves as a powerful tool to externally provide amplitude and phase control, the optimal application of the wavefront shaping to compensate for the scattering in the media can be challenging. Often, it requires a full knowledge of both the amplitude and phase of a field and hence resorts to an interferometric design which is vulnerable to system vibration. This study introduces Complex Semi-Definite Programming (SDP) as a novel approach to solve the associated phase retrieval problem for the control of light transmission through highly scattering media. Importantly, the approach removes the need for a reference beam and the simple optical setup only involves a SLM, a camera and a few passive optical components. The SLM generates

a random sequence of phase-modulated wavefronts, and a camera records the resulting intensity speckle patterns in the transmitted light. The SDP algorithm then computes the complex transmission matrix of the scattering system from this sequence of intensity-only measurements. Once the transmission matrix is recovered, optimal wavefronts are rendered via the SLM that focus the incident beam to any position or sequence of positions on the far side of the scattering medium, without the need for any subsequent measurements or wavefront shaping iterations. The number of measurements required and the degree of enhancement of the intensity at focus is determined by the number of pixels controlled by the SLM.

This is collaborative work of a DARPA project led by Dr. Moussa N'Gom. The optical experiments were performed by Dr. Moussa N'Gom, the algorithm was developed by Professor Raj Rao Nadakuditi and I contributed to the infrastructure of the software implementation. The result of this work is published in *Scientific Reports* in 2017.¹⁰⁹

Section 3.2 Previous works

The strategies to apply wavefront shaping have developed into two primary directions. The first are iterative methods which progressively improve field focus by sequentially modulating the input beam, based on the previous measurements of the transmitted intensity profile.¹⁰² Iterative methods are straight forward to implement, without need for prior knowledge about the scattering system, and a local optimum is always reached. The approaches however, tend to be slow and the progression to a global optimum is never guaranteed. Importantly, they must be repeated every time a new target output intensity profile is specified, even if speckle correlations (i.e., the memory effect) can be exploited to refocus fields onto a neighboring pixel with only minor degradation in intensity without restarting the algorithm.¹¹⁰ In the deep medium regime, where the fields are decorrelated and the memory effect no longer holds, refocusing requires the procedure to be repeated every time a new target output profile is specified.

Another direction, called the transmission matrix (TM) approach, has completely different characteristic from the iterative method. Optimal wavefront that leads to the constructive interference at the target point can be computed without a need for subsequent measurements or iterations. Therefore, the TM approach is particularly powerful in the applications where the target

output intensity profile varies frequently.¹⁰⁴ This however, comes with the price that at least part of the transmission matrix of the scattering system must be known in advance which can be understood as the preprocessing step. Depending on the specific application, the portion of the TM required can vary a lot. If the desired output is a focal spot, then the knowledge on some row of the TM is sufficient. The first measurement of an optical TM was performed by Popoff et al.¹¹¹ Most approaches developed to date to measure TMs rely on holographic methods to recover the complex TM.^{104,112} No doubt, methods for determining TMs that do not require a reference beam could be advantageous in this context and a step in this direction was taken by Drémeau et al. recently.¹¹³

This work serves as a TM approach toward the implementation without need for a reference. Unlike the work done by Drémeau et al., who applied digital micromirror device (DMD) as the light modulator and solved the corresponding phase retrieval problem in the variable of binary amplitude modulation, we formulate the phase retrieval problem as an optimization in the variable of phase modulation. The formulation in the phase instead of binary amplitude is advantageous from the perspective of a higher theoretically achievable enhancement.¹⁰² Semidefinite programming (SDP) as the method to retrieve the phase elements of the TM leverages a rigorous yet flexible computational framework that utilizes the algorithm developed by Waldspurger et al.¹¹⁴ It requires only the intensities recorded in the desired focal spot, produced by several randomly structured illuminations of the scattering medium, to recover the relevant parts of the TM (specifically in our experiment, it is one row of TM).

Section 3.3 Algorithm

Section 3.3.1 Transmission matrix formulation

Consider a light scattering system, where a highly scattering random medium is sandwiched in between the rectangular input and output apertures, see Fig 3.1. The input and output apertures can be pixelized with an $n_x \times n_y$ array and an $m_x \times m_y$ array, respectively. Light on the input aperture impinging on the random medium can therefore be described by an $n_x \times n_y$ matrix, where each matrix element assigns the electric field onto its corresponding grid location. Similarly, light leaving the output aperture can be characterized by an $m_x \times m_y$ matrix. In the most

general form, the assigned electric field is a complexed-value vector, where the information of phase and polarization are included. In this study, we assume the presence of polarizers on both planes that scalarize the electric field so that the problem be solved in a concise form.

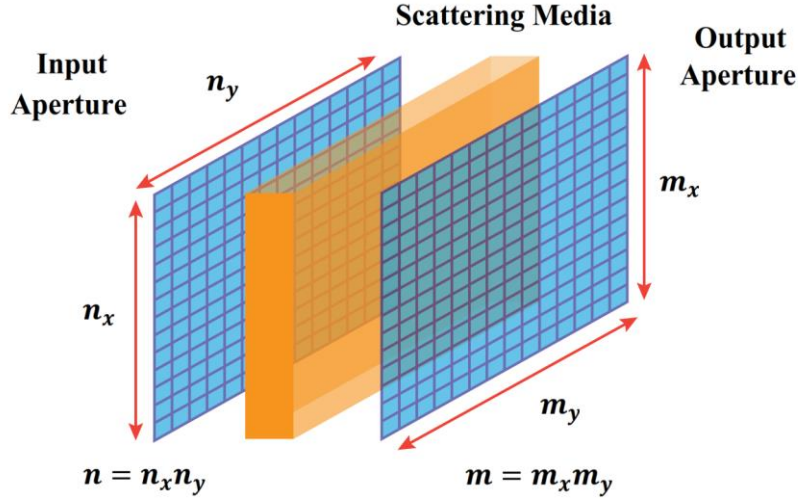


Figure 3.1 The schematic and geometric settings of the scattering system. The scattering medium is sandwiched between two rectangular apertures. The input and output apertures are pixelized with an $n_x \times n_y$ array and an $m_x \times m_y$ array, respectively.

The process of light scattering from the input aperture through the in-between media to the output aperture can be linearly modeled, with the following reasoning. First, each of the grid on the input aperture can be regarded as an individual contributing light source, called the *input channel*, and similarly for the *output channel*. Consider a complex scalar electric field E_j^{in} at the input channel indexed with j , where the convention of linear index is applied and used throughout the context. The electric field then propagates and experiences complicated interactions in the scattering media, with the resulting electric field being $E_i^{\text{out}} = T_{ij} E_j^{\text{in}}$ at the output channel i . The process can be extended to every possible pair of (i, j) and since each channel is considered as independent, superposition applies. The complete scattering process can therefore be described by a linear operation:

$$\mathbf{E}^{\text{out}} = \mathbf{T} \cdot \mathbf{E}^{\text{in}}, \text{ where}$$

$\mathbf{E}^{\text{out}} = [E_1^{\text{out}}, E_2^{\text{out}} \dots E_m^{\text{out}}]^T \in \mathbb{C}^{m \times 1}$ and $\mathbf{E}^{\text{in}} = [E_1^{\text{in}}, E_2^{\text{in}} \dots E_n^{\text{in}}]^T \in \mathbb{C}^{n \times 1}$ are the column vectors vectorized from the complex electric field on the output and input apertures, respectively.

$\mathbf{T} = \begin{bmatrix} T_{11} & T_{12} \dots & T_{1n} \\ \vdots & \vdots & \\ T_{i1} & T_{i2} \dots & T_{in} \\ \vdots & \vdots & \\ T_{m1} & T_{m2} \dots & T_{mn} \end{bmatrix} \in \mathbb{C}^{m \times n}$ is the *transmission matrix* that characterizes the scattering

media; $m = m_x m_y$ and $n = n_x n_y$ are the number of output and input channels, respectively.

Section 3.3.2 Spatial light modulation

The objective is to manipulate the incident field subject to an energy constraint so that it produces a maximally focused spot at a predefined location in the output plane. This can be achieved with the use of a light modulator. While full amplitude and phase control is possible, in this study we focus on phase-only modulation as it permits a simpler optical setup. An external phase profile can be applied to the incident electric fields that impinges on the pixelized surface of a spatial phase modulator (SLM). For simplicity, the SLM is set such that modulator surface coincides with the input aperture and assume beam profile is unity. Note the two simplifications are always valid since any deviation from the settings can be absorbed into the transmission matrix. The phase modulation can therefore be modeled as:

$$\mathbf{E}^P = e^{iP} = [e^{i\theta_1}, e^{i\theta_2} \dots e^{i\theta_n}]^T \in \mathbb{C}^{n \times 1}, \text{ called } \textit{phase vector}$$

where $\mathbf{P} = [\theta_1, \theta_2 \dots \theta_n]^T$ is the spatial phase map to apply on the beam profile.

With the application of SLM, we have

$$\mathbf{E}^{\text{out}} = \mathbf{T} \cdot \mathbf{E}^P,$$

and the problem of maximizing the intensity at output channel i , i.e., $|E_i^{\text{out}}|^2$, is subject to the determination of the optimal spatial phase map \mathbf{P}^{opt} such that

$$\mathbf{P}^{\text{opt}} = \max_{\mathbf{P}} |\mathbf{t}_i \cdot \mathbf{E}^P|^2, \text{ where}$$

$$\mathbf{t}_i = [T_{i1}, T_{i2}, \dots T_{in}] \in \mathbb{C}^{1 \times n} \text{ is the } i^{\text{th}} \text{ row of the transmission matrix } \mathbf{T} \text{ and}$$

$|\cdot|$ is the complex modulus operator.

Recovering \mathbf{t}_i however, is *not* trivial. While system is described in a simple linear form $\mathbf{E}^{\text{out}} = \mathbf{T} \cdot \mathbf{E}^P$, obtaining \mathbf{t}_i is not the conventional inverse problem, where \mathbf{t}_i can be solved with the knowledge of \mathbf{E}^P (the applied phase vector) and \mathbf{E}^{out} (the measured electric field). The challenge comes from the fact that, \mathbf{E}^{out} is *complex* and *cannot* be directly measured. The complete knowledge of \mathbf{E}^{out} from measurements would require an interferometric design which is vulnerable to system vibration and has been demonstrated before.¹¹⁴

Instead of the interferometric approach, we seek to solve \mathbf{t}_i using only a camera, where its i^{th} pixel measures the square of field magnitude $|E_i^{\text{out}}|^2$. The strategy is therefore, to apply w sets of spatial phase map $[\mathbf{P}_1, \mathbf{P}_2, \dots, \mathbf{P}_w]$ to the SLM and the w incident fields are modulated as

$$[\mathbf{Q}_1, \mathbf{Q}_2, \dots, \mathbf{Q}_w] = [e^{P_1}, e^{P_2}, \dots, e^{P_w}]$$

and we then record the corresponding w field magnitudes at the i^{th} output channel,

$\mathbf{b}_i = [b_1 \ b_2 \ \dots \ b_w]^T \in \mathbb{R}^{w \times 1}$. These data can be related in a compact matrix form as (in a noiseless setting):

$$\text{abs}(\mathbf{A}\mathbf{t}_i) = \mathbf{b}_i \text{ where } \mathbf{A} = \begin{bmatrix} \mathbf{Q}_1^T \\ \mathbf{Q}_2^T \\ \vdots \\ \mathbf{Q}_w^T \end{bmatrix} \in \mathbb{C}^{w \times n}$$

and $\text{abs}(\cdot)$ is the element-wise complex modulus operator.

The problem is therefore formulated as:

$$\text{Find } \mathbf{t}_i \text{ such that } \text{abs}(\mathbf{A}\mathbf{t}_i) = \mathbf{b}_i, \text{ in the variable } \mathbf{t}_i \in \mathbb{C}^n$$

which is known as the phase-retrieval problem.

Section 3.3.3 Phase retrieval with SDP

The focus of Section 3.3.3 is the introduction of the procedure to solve \mathbf{t}_i based on the *PhaseCut* algorithm.¹¹⁴ As discussed, we obtain $\text{abs}(\mathbf{A}\mathbf{t}_i) = \mathbf{b}_i$ through applying a sets of training

spatial phase maps and the measurement of the corresponding field magnitudes at the i^{th} output channel.

Now assume the magnitude and the phase parts of $\mathbf{A}\mathbf{t}_i$ are decoupled as $\mathbf{A}\mathbf{t}_i = \text{diag}(\mathbf{b}_i)\mathbf{u}$, where $\mathbf{u} \in \mathbb{C}^w$ is a phase vector, i.e., $|u_i| = 1$. The original phase-retrieval problem can be cast into the optimization of

$$\min \|\mathbf{A}\mathbf{t}_i - \text{diag}(\mathbf{b}_i)\mathbf{u}\|_2^2, \text{ in the variable } \mathbf{t}_i \text{ and } \mathbf{u} \in \mathbb{C}^w, \text{ with } |u_i| = 1.$$

where $\|\cdot\|_2$ operates on a complex vector and returns its Euclidean norm.

Optimization over \mathbf{t}_i is a standard least square problem, with the solution being $\mathbf{t}_i = \mathbf{A}^\dagger \text{diag}(\mathbf{b}_i)\mathbf{u}$ and therefore we solve

$$\min \|\mathbf{A}\mathbf{A}^\dagger \text{diag}(\mathbf{b}_i)\mathbf{u} - \text{diag}(\mathbf{b}_i)\mathbf{u}\|_2^2, \text{ in the variable } \mathbf{u} \in \mathbb{C}^w, |u_i| = 1$$

which can be rewritten as:

$$\min \mathbf{u}^* \mathbf{M} \mathbf{u}, \text{ in the variable } \mathbf{u} \in \mathbb{C}^w, |u_i| = 1$$

$$\text{where } \mathbf{M} = \text{diag}(\mathbf{b}_i)(\mathbf{I} - \mathbf{A}\mathbf{A}^\dagger)\text{diag}(\mathbf{b}_i)$$

This can be transformed into an equivalent linear programming by setting $\mathbf{U} = \mathbf{u}\mathbf{u}^* \in \mathbf{H}_w$ which is a $w \times w$ Hermitian matrix:

$$\min \text{Tr}(\mathbf{U}\mathbf{M}), \text{ in the variable } \mathbf{U} \in \mathbf{H}_w$$

$$\text{subject to } \text{diag}(\mathbf{U}) = \hat{\mathbf{1}}, \mathbf{U} \succcurlyeq 0, \text{Rank}(\mathbf{U}) = 1$$

Note $\mathbf{U} \succcurlyeq 0$ denotes the positive semidefinite constraint. The constraint $\text{diag}(\mathbf{U}) = \hat{\mathbf{1}}$ is a direct result of $\mathbf{U} = \mathbf{u}\mathbf{u}^*$ and $|u_i| = 1$. We then drop the nonconvex rank constrain for the convex relaxation:

$$\min \text{Tr}(\mathbf{U}\mathbf{M}), \text{ in the variable } \mathbf{U} \in \mathbf{H}_w$$

$$\text{subject to } \text{diag}(\mathbf{U}) = \hat{\mathbf{1}}, \mathbf{U} \succcurlyeq 0$$

which is an SDP in standard form and \mathbf{U} can be computed efficiently using the *cvx* package.¹¹⁵ The theoretical guaranties accompanying *PhaseCut* establish that when $w > \mathcal{O}(n \log n)$,¹¹⁴ this

procedure will perfectly recover a unique solution \mathbf{U} with high probability in the noise-free setting when the training phase vectors are drawn at random.

A last step is required, to solve \mathbf{u} from \mathbf{U} for the ultimately desired quantity \mathbf{t}_i , the i^{th} row of the transmission matrix \mathbf{T} . Ideally the solved \mathbf{U} can be factored into $\mathbf{u}\mathbf{u}^*$ and has rank 1. Practically the low rank approximation is used: Let $\mathbf{v}_1(\mathbf{U})$ be the eigenvector of \mathbf{U} with the largest eigenvalue λ_1 . The optimal solution is then $\mathbf{u} = \frac{\mathbf{v}_1(\mathbf{U})}{\|\mathbf{v}_1(\mathbf{U})\|} \in \mathbb{C}^w$ and finally $\mathbf{t}_i = \mathbf{A}^\dagger \text{diag}(\mathbf{b}_i)\mathbf{u}$. After we compute \mathbf{t}_i , solving the optimal \mathbf{P} , \mathbf{P}^{opt} , is trivial:

$$\mathbf{P}^{\text{opt}} = (-\angle \mathbf{t}_i)^T = [\angle T_{i1}, \angle T_{i2}, \dots, \angle T_{in}]^T \in \mathbb{R}^{n \times 1}$$

Section 3.4 Experimental results

Figure 3.2 shows the experimental setup. The light source is a single longitudinal mode diode laser with wavelength $\lambda \sim 633$ nm and output power 50 mW. The beam is expanded to a diameter of 20 mm by a beam collimator. A set of polarization optics is used to select the suitable polarization state of the incident beam for the phase-only modulation. The phase-only SLM is a LCOS (Liquid Crystal on Silicon) micro-display with full HD resolution (1920×1080 pixels) and $8 \mu\text{m}$ pixel pitch. The surface of the SLM is $4-f$ imaged and focused on the scattering sample by a lens with 50 mm focal length. The Fourier plane of the backside of the sample is imaged onto a CMOS camera, which has 2048×2048 resolution and $8 \mu\text{m}$ pixel size. The samples used for this experiment are ground glass (i.e., frosted glass) and yogurt, for the static and quasi-static studies respectively. The glass diffuser is 2 mm thick and 120 grit. The yogurt sample is prepared by spreading the plain white yogurt in between two thin microscope slides and pressed to form a thin white translucent layer similar to white paint on glass.

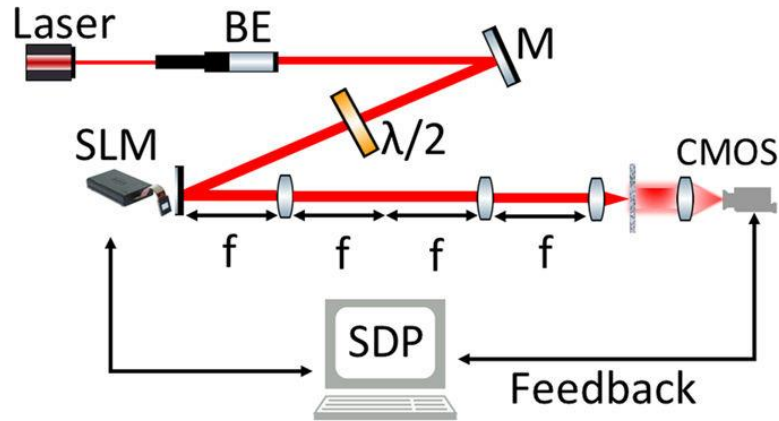


Figure 3.2 Experimental setup for the TM determination using SDP method. A 633 nm CW laser is expanded then spatially filtered through a lens and a 100 μm pinhole (not shown). The polarization optics are placed before the SLM. The homogeneous beam is then reflected by the SLM that is $4f$ imaged onto the sample. The resulting speckle pattern from the scattering sample is collected by a lens and imaged on the CMOS camera. Adapted from ref ¹⁰⁹.

We first study the ground glass sample. Since the independent control of every pixel on the SLM is extremely expensive, we subdivide the SLM display into n equally sized squares, called *superpixels*. The SLM is set to assign identical phase value to every pixels that are within the same superpixel, in the range of $[0, 2\pi]$. On the other hand, phase values assigned to different superpixels are random. Following the notations in the previous section, all the n phase values of the superpixels constitute the spatial phase map \mathbf{P} . In this experiment, $w = 461$ sets of \mathbf{P} are generated for the phase modulation, and the corresponding transmitted field magnitudes \mathbf{b}_i at $i = (940, 540)$ are measured after the ground glass.

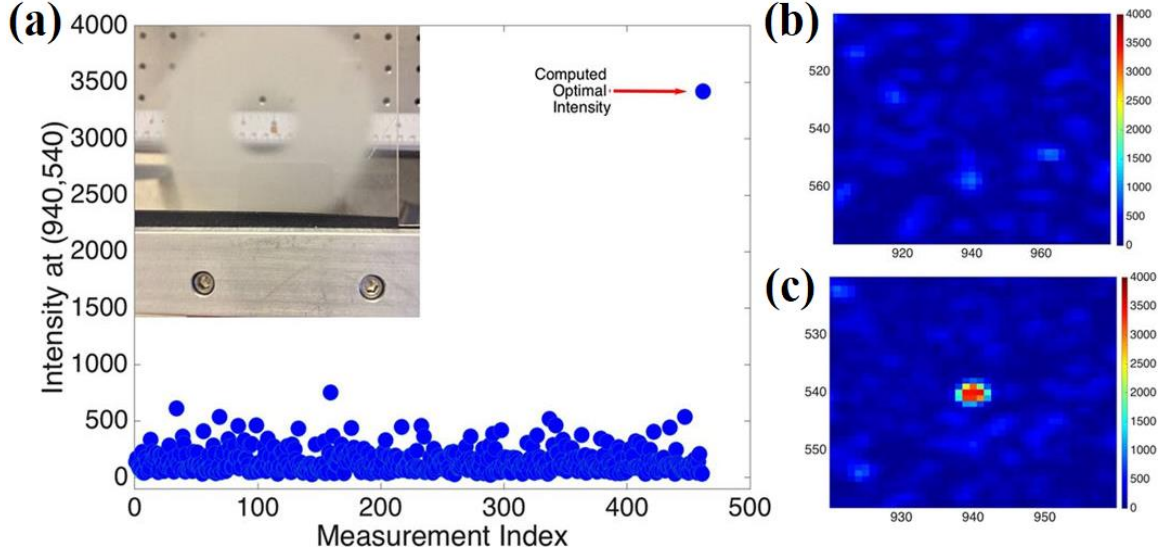


Figure 3.3 Optimal light focusing through ground glass sample. (a) A plot of the intensity at the target spot from 461 random trial fields, followed by the intensity using the optimal wavefront. (inset) Groundglass sample. (b) zoomed-in image of the measured average speckle pattern. (c) high intensity focus obtained using the optimal wavefront. Each camera pixel corresponds to $8 \mu\text{m}$. Adapted from ref ¹⁰⁹.

As clearly seen in Fig 3.3(a), the first 461 measured intensities are fairly weak. This is not surprising since they result from the random phase modulations. The last measurement, $|E_i^{\text{opt}}|^2$ results from applying the optimal spatial phase map \mathbf{P}^{opt} for the phase modulation and is considerably stronger than the previous measurements, validating the effectiveness of the SDP algorithm. An enhancement of $\eta = 48$ is achieved, see Fig 3.3(b, c), where η is defined as

$$\eta = |E_i^{\text{opt}}|^2 / |E_{\text{avg}}|^2,$$

and $|E_{\text{avg}}|^2$ is the average intensity obtained by averaging intensities at the i^{th} output channel with w training phase modulations applied.

While the ground glass sample speckle pattern can be static for hours, the yogurt sample has a speckle lifetime in scale of minutes, and it is verified in the study of the yogurt sample that the SDP algorithm is stable and fast enough to be relevant for samples that are quasi-static. In this experiment, three optimal output intensity profiles were obtained, with different number of superpixels, see Fig 3.4 (b, c, d) Note the generated foci are confined to within a single detector

pixel, considerably smaller than the focal profile in the case of ground glass. This can be understood with the fact that, the scattering process in the media can provide bandwidth to the angular spectrum and thus making the scattering media an unconventional lens to achieve imaging beyond the diffraction limit of the optical system.¹¹⁶ This property is manifested by the speckle size of the scattering system, and note that the speckle size of the yogurt sample is much smaller than that of the ground glass sample. The recorded maximal intensities on the three profiles also indicate that the enhancement at the desired point in general increases with the number of superpixels.

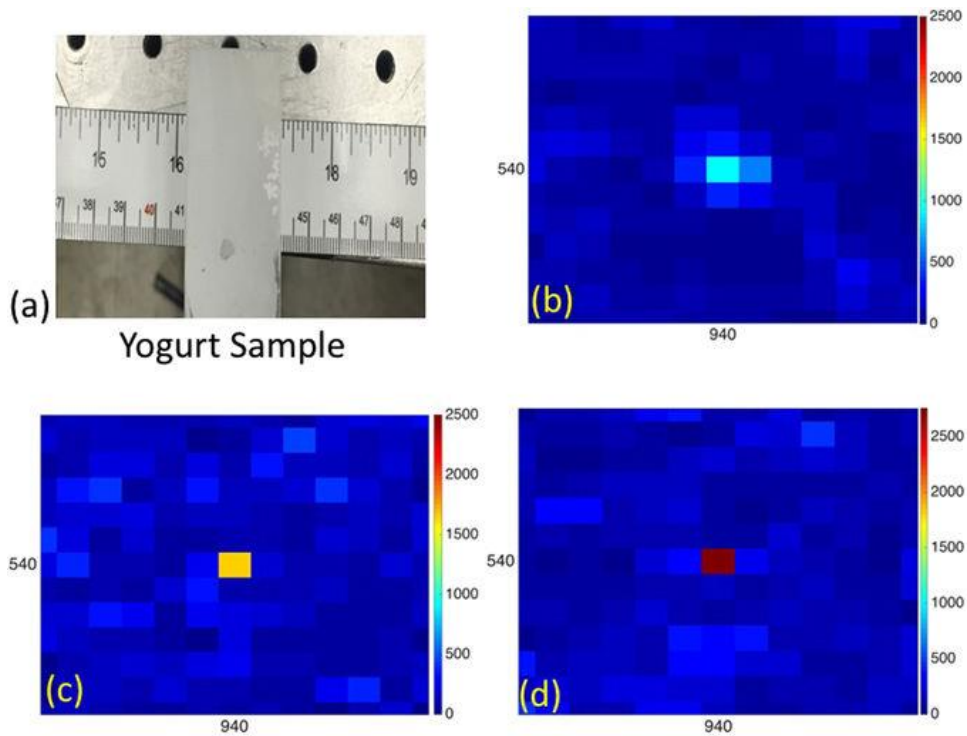


Figure 3.4 Optimal light focusing through yogurt sample. (a) real picture of the yogurt sample (b) the intensity at pixels surrounding (940, 540) after a focus is generated at (940, 540) using the SDP algorithm with with 36 (c) 64 (d) 100 superpixels. Adapted from ref ¹⁰⁹.

Finally, note that the introduced scheme with SDP can be efficient in the sense of data acquisition. Given the computation is highly parallelizable, multiple rows of TM can be determined simultaneously with the same sampling procedure as discussed, since the camera

records the *entire* output channels in each capture. We demonstrate in Fig 3.5 two sets of foci generated beyond the scattering medium that traces out MIAO-BIN (my name) and MICHIGAN respectively.

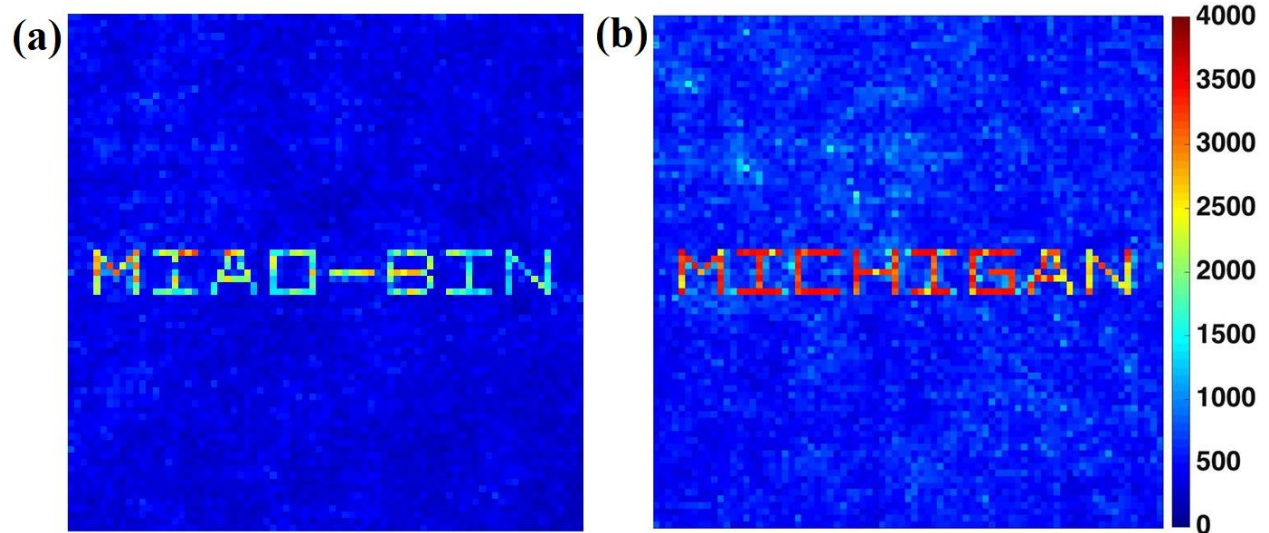


Figure 3.5 Spell-out of words beyond the scattering media using SDP method. (a) spell-out of MIAO-BIN (b) spell-out of MICHIGAN. Image (b) adapted from ref ¹⁰⁹.

Section 3.5 Summary

We demonstrate a new method for controlling light transmission through highly scattering random media by shaping wavefronts that optimally focus the incident beam to any position, or sequence of positions, on the far side of a scattering medium. The optimal wavefront for a particular focus position is determined in closed-form from knowledge of the complex-valued transmission matrix, which we determine using a sequence of intensity-only measurements, without the need for a reference beam, using a semidefinite programming based phase retrieval method. Once the transmission matrix is thus determined, we demonstrate that increasing the number of modes increases the intensity of the focus and that we can steer the focus.

CHAPTER 4

Optics of Graphene

Section 4.1 Introduction

Graphene is an amazing material in various aspects. It has the ultimate atomic thickness and is the strongest material ever measured.¹¹⁷ It has extremely high intrinsic carrier mobility and thermal conductivity.¹¹⁸ Since the first isolation of single-layer graphene in 2004,¹¹⁹ many other crystalline materials, such as transition metal dichalcogenides (TMDs), molybdenum disulphide (MoS₂),¹²⁰ and hexagonal boron nitride (h-BN),¹²¹ have also been exfoliated or grown into atomically thin layers. They are now classified as two-dimensional (2D) materials,¹²² which have very distinct properties from their bulk counterparts.

As a true 2D material, graphene exhibits unique electronic properties and has been demonstrated by various research groups to be an interesting photonic building block.¹²³ In this chapter, we explore two aspects of the optics of graphene. In the first part, we investigate the absorption saturation in optically excited graphene. The microscopic theory is studied using graphene Bloch equations within the equation of motion formalism, where both the carrier-carrier scattering (Coulomb-scattering) and the carrier-phonon scattering are included. The saturation behavior was found to be the interplay between Pauli-blocking and scattering-induced redistribution of the excited carriers. Under the ultrashort pulse setting, the temporal evolution of the pump-induced change of the carrier occupation was numerically solved, and shown to agree with the experimental results of the optical differential transmission measurement where a 60-layer epitaxial graphene sample was excited with the ultrafast laser pulses.

In the second part, we focus on the opportunities provided by graphene as the key material that enables novel applications in the photodetection and the imaging system. Graphene

photodetectors with different detection mechanisms have been previously explored, such as photovoltaic,¹²⁴ photo-thermoelectric,¹²⁵ and bolometric effects.¹²⁶ Most of the designs however, suffer either from the low responsivity due to the weak absorption of graphene (only 2.3% for monolayer),¹²⁷ or the loss of ultra-broadband detection with the application of a resonant system.¹²⁸ Very recently, a highly sensitive, all-graphene heterojunction photodetector that preserves the ultra-broadband detection, was demonstrated. It utilizes a gain mechanism from the photo-gating effect to increase the responsivity.¹²⁹ Importantly, the all-graphene photodetector is highly transparent, graphene can be not only used as the photoconductive gain material but also the circuit interconnects. Therefore, unlike the photodetectors made of silicon or similar material, these transparent graphene detectors can be used in an unconventional stacked fashion.

On this basis, we propose a novel imaging system that consists of a main camera lens followed by a set of graphene transparent detector arrays, which allows the *simultaneous* capture of 2D images under different focusing conditions, called *focal stack*. A high-dimensional visual information (to be exact, 4D), called *light field*, can be reconstructed from the focal stack data with the model-based approach, which is the main focus of the next chapter. In this study, we provide the detail about the fabrication and working principle of the transparent graphene detector. While a dense 2D array of transparent graphene sensors is not available at this stage, we demonstrate the key operating principle with a proof-of-concept single-pixel focal stack light field camera and perform optical ranging.

The optical saturation study of graphene was done in collaboration with Dr. Malic's group, where the microscopic theory was developed by Winzer et al. and I conducted the optical experiment to measure the saturation behaviors of graphene. The result of this work was published in *Applied Physics Letters* in 2012.¹³⁰ The project of focal stack light field camera using transparent graphene detector was done in collaboration with Prof. Zhong's group. The device fabrication and characterization was done by Che-Hung et al.; I built the single-pixel, proof-of-concept focal stack camera and collected the optical ranging data.

Section 4.2 Overview of graphene

Section 4.2.1 Electronic properties of graphene

A carbon atom has the electronic configuration of $C^6 = 1s^2 2s^2 2p^2$ and 4 valence electrons. It has atomic orbitals that can hybridize since the s -orbital and p -orbitals of carbon's second electronic shell have very similar energies. Within graphene, one s -orbital and two p -orbitals of each carbon atom undergo an sp^2 hybridization. It leads to a trigonal planar structure with a formation of a σ bond between carbon atoms that are separated by 1.42 Å. We therefore see graphene has a honeycomb structure made of hexagons, see Fig 4.1(a). The σ band is responsible for the robustness of the lattice structure in all allotropes. Because of the Pauli principle, these bands have a filled shell and therefore form a deep valence band. The unaffected p -orbital, considered to be in the $2p_z$ state and perpendicular to the planar structure, can bind covalently with the neighboring carbon atoms, leading to the formation of a π band, see Fig 4.1(a, b). Since each p -orbital has one extra electron, the π band is half filled. These delocalized electrons in the $2p_z$ state constitute the distributed π bonding in the sheet, and are responsible for the electrical conductivity of graphene.

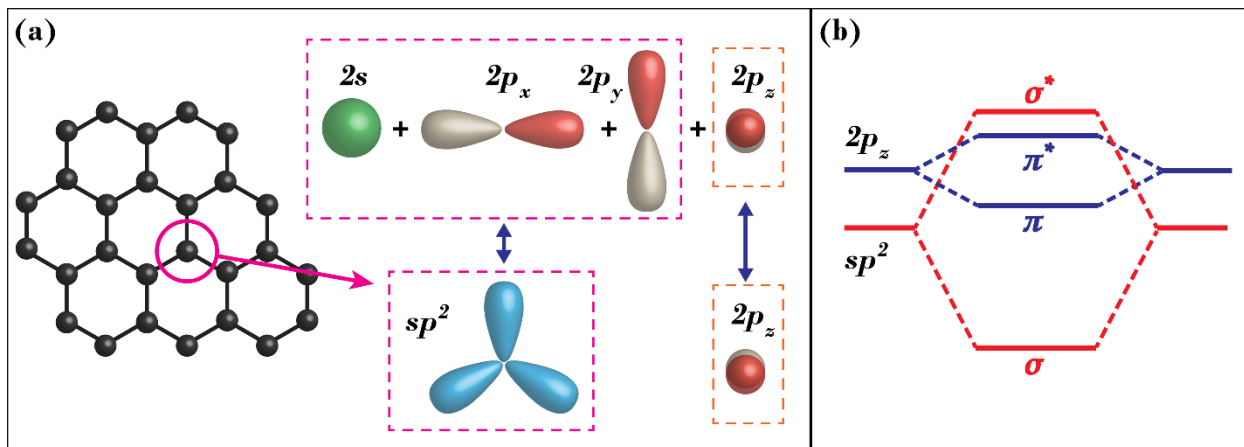


Figure 4.1 Electronic configuration of graphene. (a) Graphene structure with sp^2 co-planar bonding. (b) Energy level diagram of σ band (sp^2 hybridization) and π band ($2p_z - 2p_z$) in graphene.

The hexagonal honeycomb lattice of graphene can be viewed as two embedded triangular sublattices (labeled by A and B). The band theory of graphene has been derived with the tight-binding model. In this approach, only the hopping energies to the nearest sites are considered for the system Hamiltonian, and the energy-momentum dispersion relation can be analytically solved through the eigenvalue problem of $\mathcal{H}\psi = \varepsilon\psi$.¹³¹

$$\varepsilon(\mathbf{k}) = \varepsilon(k_x, k_y) = \pm t \sqrt{3 + 2 \cos(k_y a) + 4 \cos\left(\frac{k_x a}{2}\right) \cos\left(\frac{\sqrt{3} k_y a}{2}\right)}$$

where $t \approx 2.7$ eV is the hopping integral, the energy required to hop from one atomic site to its nearest neighbor and $a = 1.42$ Å is the lattice constant.

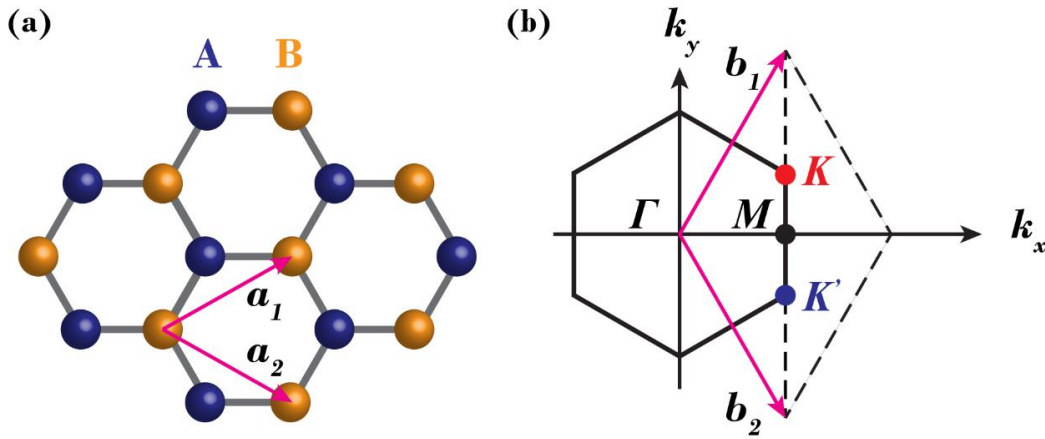


Figure 4.2 Honeycomb lattice and its Brillouin zone. (a) lattice structure of graphene, made out of two interpenetrating triangular lattices; \mathbf{a}_1 and \mathbf{a}_2 are the lattice unit vectors. (b) corresponding Brillouin zone. The Dirac cones are located at the K and K' points.

The most exciting and nonconventional electronic properties occur at the K and K' points where the π and π^* bands connect at zero energy in the k space (and therefore zero bandgap), called Dirac points (Fig 4.2). Specifically,

$$\mathbf{K} = \left(\frac{2}{3}\mathbf{b}_1 + \frac{1}{3}\mathbf{b}_2\right) + m\mathbf{b}_1 + n\mathbf{b}_2$$

$$\mathbf{K}' = \left(\frac{1}{3}\mathbf{b}_1 + \frac{2}{3}\mathbf{b}_2\right) + m\mathbf{b}_1 + n\mathbf{b}_2$$

where $\mathbf{b}_1 = \frac{2\pi}{3a}(1, \sqrt{3})$, $\mathbf{b}_2 = \frac{2\pi}{3a}(1, -\sqrt{3})$ are the reciprocal lattice vector and m, n are arbitrary integers. When performing low-energy expansion near $K(K')$ points, i.e., $\mathbf{k} = \mathbf{K}(K') + \mathbf{q}$, the effective Hamiltonian near the Dirac points can be expressed in a compact form of ¹³²

$$\mathcal{H}_K(\mathbf{q}) = \mathcal{H}(K + \mathbf{q}) = \hbar v_F \begin{bmatrix} 0 & q_x - iq_y \\ q_x + iq_y & 0 \end{bmatrix} = \hbar v_F \boldsymbol{\sigma}_{x,y} \cdot \mathbf{q}$$

$$\mathcal{H}_{K'}(\mathbf{q}) = \mathcal{H}(K' + \mathbf{q}) = \hbar v_F \begin{bmatrix} 0 & q_x + iq_y \\ q_x - iq_y & 0 \end{bmatrix} = \hbar v_F \boldsymbol{\sigma}'_{x,y} \cdot \mathbf{q}$$

where $\boldsymbol{\sigma}_{x,y} = \sigma_x \hat{\mathbf{x}} + \sigma_y \hat{\mathbf{y}}$, $\boldsymbol{\sigma}'_{x,y} = \sigma_x \hat{\mathbf{x}} - \sigma_y \hat{\mathbf{y}}$; $\sigma_x = \begin{bmatrix} 0 & 1 \\ 1 & 0 \end{bmatrix}$, $\sigma_y = \begin{bmatrix} 0 & -i \\ i & 0 \end{bmatrix}$ are the Pauli matrices and $v_F = \frac{3}{2}ta/\hbar \approx 10^6$ (m/s) is the Fermi velocity. The energy dispersion and the two-component wavefunction can be solved by demanding $\det(\mathcal{H}_{K(K')} - \mathcal{E}I) = 0$:

$$\mathcal{E}_K(\mathbf{q}) = \mathcal{E}_{K'}(\mathbf{q}) = \pm \hbar v_F |\mathbf{q}|$$

$$|\psi_K\rangle = \frac{1}{\sqrt{2}} \begin{bmatrix} e^{-i\theta_q/2} \\ \pm e^{i\theta_q/2} \end{bmatrix} |\mathbf{q}\rangle \text{ and } |\psi_{K'}\rangle = \frac{1}{\sqrt{2}} \begin{bmatrix} -e^{-i\theta_q/2} \\ \pm e^{i\theta_q/2} \end{bmatrix} |\mathbf{q}\rangle$$

where $\theta_q = \tan^{-1}(q_y/q_x)$. The \pm signs correspond to the conduction band (electron) and valence band (hole) respectively. Due to the band structure symmetry, the electrons and holes exhibit the same electronic behaviors at K points. The two-component column vector is the pseudospinor that defines the chirality of the particle and is important in suppressing the backscattering.¹³³ Note the electron and the hole near the K points have the opposite chiralities and hence are the antiparticles to each other. The conservation of chirality enables the unimpeded penetration through tall and wide potential barriers, which leads to the high mobility of graphene.¹³⁴

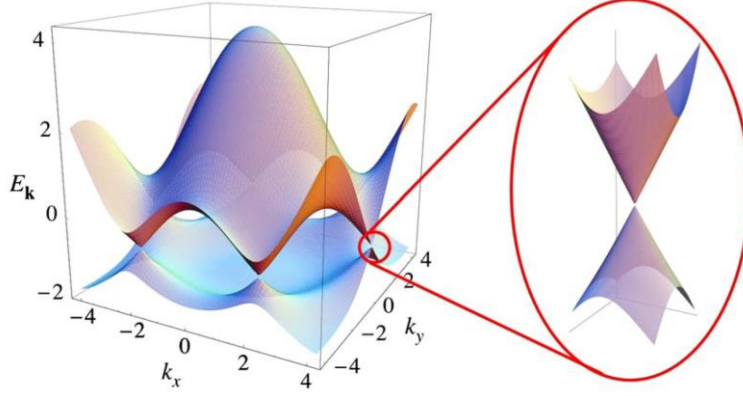


Figure 4.3 Electronic dispersion in the honeycomb lattice. Left: energy spectrum (in units of t) Right: zoom in of the energy bands close to one of the Dirac points, where π and π^* bands connect. Adapted from ref ¹³².

The shape of this dispersion relation is a cone, called Dirac cone (Fig 4.3). Such a linear dispersion makes electrons around K points behave very differently from that governed by the common parabolic dispersion. Recall the effective mass of the electron is defined as

$$m^* = \hbar^2 (\nabla_k \nabla_k \mathcal{E})^{-1}$$

which is proportional to the local radius of curvature. A linear band structure would thus give the result of $m^* = 0$, i.e., electrons would behave as if they are massless. Furthermore, the Fermi velocity at K points is independent of the momentum or energy. The relativistic-particle-like behavior of the carriers in graphene can be further illuminated by inspecting how the governing Hamiltonian at the K points resembles the 2D massless Dirac Hamiltonian:

$$\begin{aligned} \mathcal{H}_D &= c\boldsymbol{\alpha} \cdot \mathbf{p} + \beta mc^2 = \hbar c\boldsymbol{\alpha}_D \cdot \mathbf{k} \\ &\quad \updownarrow \\ \mathcal{H}_K &= \hbar v_F \boldsymbol{\sigma}_G \cdot \mathbf{k} \\ \mathcal{H}_{K'} &= \hbar v_F \boldsymbol{\sigma}'_G \cdot \mathbf{k} \end{aligned}$$

Direct comparison of the two Hamiltonians reveals some important insights. First, it is noted that $\boldsymbol{\alpha}_D$ and $\boldsymbol{\sigma}_G$ ($\boldsymbol{\sigma}'_G$) play similar roles in determining the spin properties of two systems respectively. While the basis in the two-component spinor representation of $\boldsymbol{\alpha}_D$ is the two real spin states (\uparrow, \downarrow), the basis of $\boldsymbol{\sigma}_G$ and $\boldsymbol{\sigma}'_G$ come from the occupation of electrons on two different sublattices **A** and **B**. Such a similarity to the spin index (up and down) is referred to as pseudospin. Second, the mapping of $c \leftrightarrow v_F$ indicates that the carriers at K points would travel in the speed of

v_F , analogous to the massless spin-1/2 particles traveling at the speed of c , i.e., the speed of light. These contribute to the ballistic properties of the carriers in graphene with a submicron traveling distance, giving rise to the reported high mobility of $\sim 200,000 \text{ cm}^2\text{V}^{-1} \text{ s}^{-1}$ in suspended samples.¹¹⁸

Section 4.2.2 Optical properties of graphene

Graphene is a truly 2D material and is intrinsically different from the bulk graphite with reduced number of layers, even if it is treated in a small thickness limit. The reduced dimensionality requires distinct descriptions for the physical quantities of graphene, especially those associated with volume. Optical conductivity, which is defined through the 2D surface current induced by electromagnetic waves, is therefore a better quantity to describe the optical properties of graphene than refractive index, since the induced polarization per unit volume cannot be well defined.¹³⁵

The optical conductivity $\sigma(\omega)$, is defined by $\mathcal{J} = \sigma(\omega)E_{\parallel}$ where \mathcal{J} is the surface current on graphene and E_{\parallel} is the in-plane component of the electric field. The optical conductivity is a complex quantity, with the imaginary part related to the dissipation in the medium and the real part associated with the polarization and dispersion. The surface current can be generated through an interband or an intraband transition, see Fig 4.4. The expression for the optical conductivity of graphene can be analytically derived with perturbation from the linear response theory within the Dirac band structure:^{136–138}

$$\sigma(\omega) = \sigma_{\text{inter}}(\omega) + \sigma_{\text{intra}}(\omega)$$

$$\sigma_{\text{inter}}(\omega) = \frac{\sigma_0}{2} \left(\tanh \frac{\hbar\omega + 2E_F}{4k_B T} + \tanh \frac{\hbar\omega - 2E_F}{4k_B T} \right) - i \frac{\sigma_0}{2\pi} \log \left[\frac{(\hbar\omega + 2E_F)^2}{(\hbar\omega - 2E_F)^2 + (2k_B T)^2} \right]$$

$$\sigma_{\text{intra}}(\omega) = i \frac{4\sigma_0}{\pi} \frac{E_F}{\hbar(\omega + i\gamma)}$$

where $\sigma_0 = e^2/(4\hbar)$ a constant called universal conductivity of graphene, E_F is the Fermi energy relative to the Dirac point (positive regardless of whether the graphene is p-doped or n-doped), and γ is the intraband scattering rate.

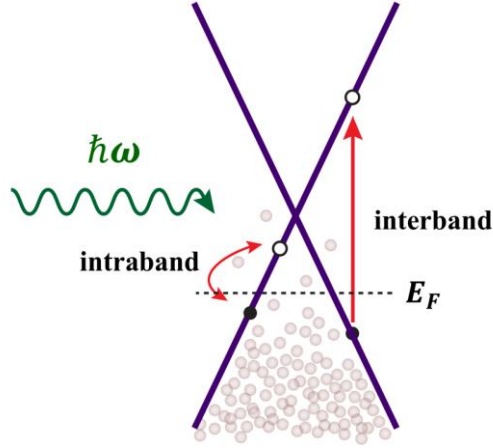


Figure 4.4 Light-induced transitions in doped graphene. Carriers can be excited through an interband or an intraband process. Due to the gapless band structure, the photoresponsivity from interband process is ultra-broadband.

Several important optical properties of graphene can be understood from the frequency responses of $\sigma(\omega)$, $\sigma_{\text{inter}}(\omega)$ and $\sigma_{\text{intra}}(\omega)$, with both the real and imaginary parts plotted in Fig 4.5. First, the intraband transition clearly dominates at low-frequency and the interband transition dominates at high-frequency. Starting from zero, the curve of $\text{Re}[\sigma_{\text{inter}}]$ experiences a prominent rise around $\hbar\omega = 2E_F$ to reach the steady state value of universal conductivity σ_0 , indicating the presence of Pauli blocking below $2E_F$. The universal conductivity σ_0 gives rise to the well-known 2.3% absorption of suspended graphene in the visible regime.¹³⁹ In addition, the Drudic form of $\sigma_{\text{intra}}(\omega)$ suggests the semi-metal nature of graphene and the ability to support plasmons.¹⁴⁰ Note however, that while the Drude weight for a bulk metal is proportional to n , the carrier density, the Drude weight for graphene is proportional to \sqrt{n} since $\sigma_{\text{intra}}(\omega) \propto E_F \propto \sqrt{n}$.

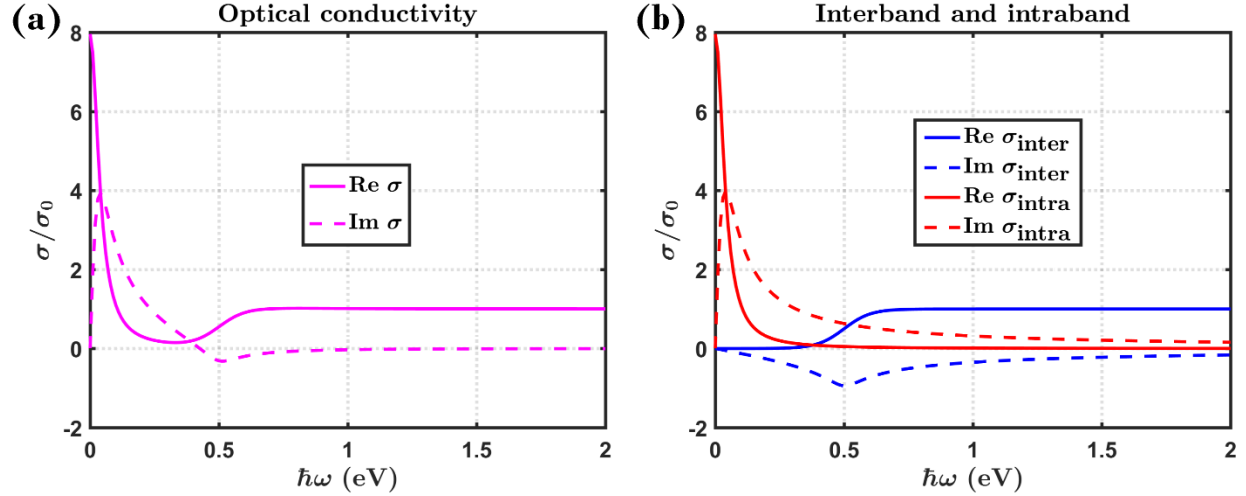


Figure 4.5 Optical conductivity of graphene with linear response theory. (a) The total conductivity, including the interband and intraband contributions: $\sigma(\omega) = \sigma_{\text{inter}}(\omega) + \sigma_{\text{intra}}(\omega)$. (b) The individual interband and intraband conductivities $\sigma_{\text{inter}}(\omega)$ and $\sigma_{\text{intra}}(\omega)$.

Due to the Dirac band structure, graphene has a very low density of states near the Dirac points and therefore the Fermi level can be changed very efficiently through carrier concentration control.¹⁴¹ Combined with the high mobility of graphene, the optical conductivity can be effectively tuned with ultrafast speed (as high as tens of GHz),¹⁴² making graphene an exciting photonic building block. Optical properties that can be electrically controlled include the wavelength at which the Pauli blocking of the interband transition begins and the Drude weight of the intraband conductivity, as shown in the plots of $\text{Re}[\sigma(\omega)]$ and $\text{Im}[\sigma(\omega)]$ at different Fermi levels in Fig 4.6.

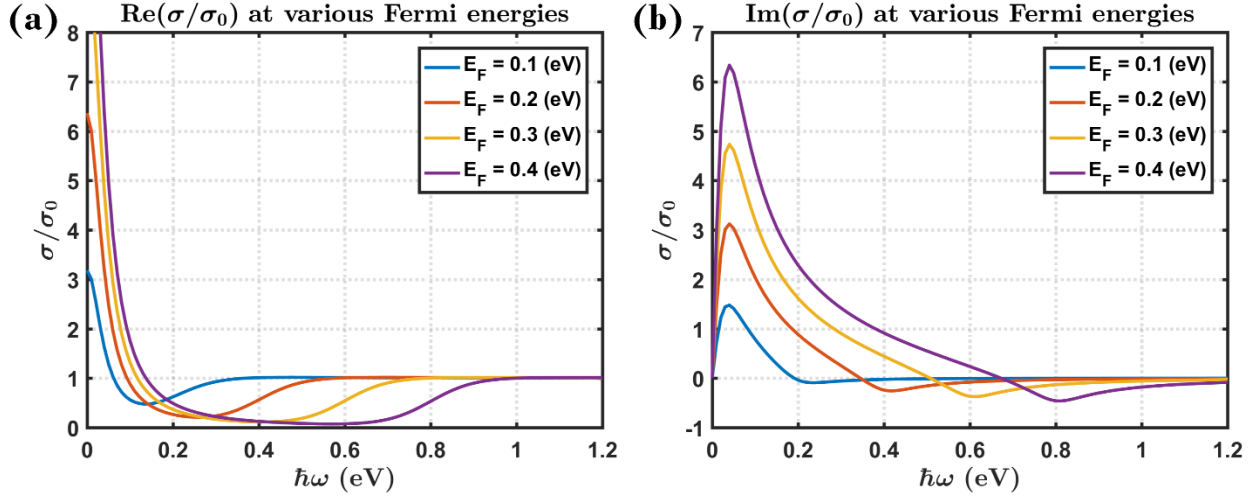


Figure 4.6 The electrically tunable optical conductivity of graphene. Real (a) and imaginary (b) part of the optical conductivity of graphene at different Fermi energies, plotted with the linear response theory. $\hbar\gamma = 40$ meV.

It is important to note that the optical properties derived above is restricted to the regime of low photon energy and low intensity excitation, and there have been studies to explore beyond this regime. The optical conductivity of graphene in the high photon energy region (up to 5 eV) has been measured with the ellipsometry-based technique,¹³⁵ and is plotted in Fig 4.7. A distinct peak of $\text{Re}[\sigma(\omega)]$ at 4.6 eV can be clearly seen, which originates from the van Hove singularity at the M point of the Brillouin zone that deviates from the linear Dirac band structure. In the regime of high photon energy, the strong electron-hole interaction can no longer be neglected and the excitonic effects should be considered.¹⁴³ In fact, it is the formation of excitons that shifts the peak associated with the M point from 5.1 eV to 4.6 eV. On the other hand, the intensity dependence of the absorption and transmission in graphene has been measured in several pump-probe experiments, where a linear dependence was observed in a low-intensity regime.¹⁴⁴ At higher pump fluence, a significant number of electrons and holes are created in the conduction and valence bands, respectively. This results in the Pauli blocking of further interband transitions, and consequently decreases the absorption.¹⁴⁵ The transmission scales nonlinearly with the intensity and saturates to a constant value. We will show in the next section that the interplay of both Pauli-blocking and intensity-dependent relaxation determines the saturation behavior. The Coulomb- and phonon-induced carrier dynamics in optically excited graphene will be investigated in more detail.

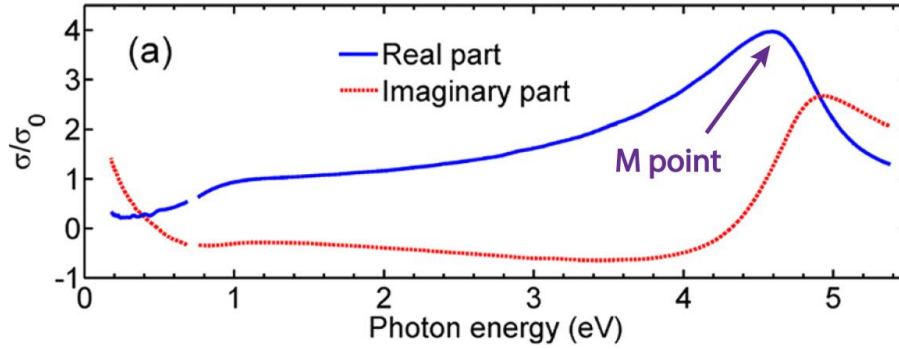


Figure 4.7 The broadband spectrum of the optical conductivity of graphene. Lines before the breakpoints are extrapolated with the linear response theory. Lines after the breakpoints are plotted with the data measured using ellipsometry technique. Adapted from ref ¹³⁵.

There are a variety of optical applications using graphene as the key element. In this study, we are particularly interested in the photodetector application of graphene. Photodetection with graphene can be advantageous for several reasons. First, because graphene has no bandgap, it absorbs light over a very broad spectrum, covering the entire range from ultraviolet to THz and hence enables ultra-broadband photodetection.¹⁴⁶ Second, graphene is a strong candidate as the basis material for transparent electronics since it is highly conductive and transparent simultaneously. In fact, we will demonstrate a prototype light field camera with a transparent focal stack implemented with graphene detectors. The working principles of the graphene detector and the complete setup of the prototype light field camera will be presented in Section 4.4.

Section 4.3 Absorption saturation in optically excited graphene

Section 4.3.1 The microscopic theory

When excited with intense light, graphene can exhibit nonlinear behaviors and it has been explored to find exciting applications in nonlinear optics. One of the impressive examples is a demonstrated working mode-locked fiber laser with graphene flake used as the saturable absorber that produced pulses with a duration of 460 fs.¹⁴⁷ A saturable absorber is a key component in passive mode-locking that shows increased transmission (reduced absorption) under stronger optical intensity. Graphene as a saturable absorber can hold distinctive merits such as the lower saturation intensity (due to the remarkably large absorption of atomic layer graphene), the ultrafast

recovery time (due to the ultrafast carrier relaxation in graphene), the large modulation depth (66% reported for pristine monolayer graphene, which is possibly the largest of all known saturable absorbers)¹⁴⁸ and the broadband tuneability (due to the zero bandgap). A fundamental understanding of the saturation behavior and the driving microscopic mechanism of graphene is thus of great interest for the development of other potential nonlinear optical applications. In the previous theoretical studies, the Coulomb-scattering, which is the most important relaxation mechanism at high carrier densities, was neglected.¹⁴⁹ We show in the following that the inclusion of the carrier-carrier relaxation channel leads to the more complete description of the scattering mechanisms and is consistent with the experimental observations.

To investigate the saturation behavior, we start with the graphene Bloch equations within the equation of motion formalism to track the dynamics of (i) p_k , the microscopic polarization which is a measure for the transition probability between the two bands (ii) ρ_k^v , the carrier occupation in the momentum state k for the conduction ($\lambda = c$) and the valence band ($\lambda = v$) and (iii) n_q^j , the phonon occupation with the momentum q in the mode j :¹⁴⁵

$$\dot{p}_k = (i\Delta\omega_k + \Omega_k^{\lambda\lambda})p_k - i\Omega_k^{vc}(\rho_k^c - \rho_k^v) + \dot{p}_k|_{\text{hf+s}}$$

$$\dot{\rho}_k^v = -2 \text{Im}[\Omega_k^{vc*}p_k] + \dot{\rho}_k^v|_{\text{hf+s}}$$

$$\dot{n}_q^j = -\gamma_{ph}(n_q^j - n_B^j) + \dot{n}_q^j|_s$$

where $\hbar\Delta\omega_k = (\mathcal{E}_k^v - \mathcal{E}_k^c)$ is the energy gap, $(\rho_k^c - \rho_k^v)$ represents the Pauli-blocking, $\gamma_{ph}^{-1} = 1.2$ (ps) is the phenomenological phonon lifetime and n_B is the Bose-Einstein equilibrium distribution for the phonons at room temperature. The light-matter interaction is considered semi-classically with $\Omega_k^{vc}(t) = i \frac{e}{m} M_k^{vc} \cdot A(t)$ as the Rabi frequency and $\Omega_k^{\lambda\lambda} = i \frac{e}{m} (M_k^{cc} - M_k^{vv})$ as the intraband carrier contribution that enables even-numbered multiple photon absorption and is proportional to the microscopic polarization p_k , where $A(t)$ is the vector potential that describes the laser pulse and $M_k^{\lambda\lambda'}$ are the wave number dependent optical matrix elements with $\lambda, \lambda' = c, v$.

The last terms in the 3 equations of motion are the Coulomb and carrier-phonon many-body interactions and can be split into the Hartree-Fock (first order) and the scattering (second and

higher order) parts. The application of second order Born-Markov approximation to the carrier and phonon occupation leads to the time-dependent Boltzmann equations of scattering rates:

$$\begin{aligned}\dot{p}_k|_{\text{hf+s}} &= \dot{p}_k|_{\text{hf}} + \dot{p}_k|_s = -\gamma_k \cdot p_k(t) + \mathcal{U}_k \\ \dot{\rho}_k^\lambda|_{\text{hf+s}} &= \dot{\rho}_k^\lambda|_{\text{hf}} + \dot{\rho}_k^\lambda|_s = \Gamma_{\lambda,k}^{\text{in}}(t)[1 - \rho_k^\lambda(t)] - \Gamma_{\lambda,k}^{\text{out}}(t)\rho_k^\lambda(t) \\ \dot{n}_q^j|_s &= \Gamma_{j,q}^{\text{em}}(t)[1 + n_q^j(t)] - \Gamma_{j,q}^{\text{ab}}(t)n_q^j(t)\end{aligned}$$

where $\Gamma_{\lambda,k}^{\text{in}}$ and $\Gamma_{\lambda,k}^{\text{out}}$ are the scattering rates in and out of the state (λ, k) including both carrier-carrier and carrier-phonon relaxation channels; $\Gamma_{j,q}^{\text{em}}$ and $\Gamma_{j,q}^{\text{ab}}$ are the phonon emission and absorption rates to the state (j, q) ; γ_k and \mathcal{U}_k correspond to the diagonal and off-diagonal parts of the coherence dephasing respectively.

Combine all the equations above and assume an ultrashort 10 fs-pulse excitations with a photon energy of $\hbar\omega = 1.5$ (eV), we can numerically solve the set of coupled differential equations in time domain, which is essentially the competing processes between the carrier scattering and optical pumping, see Fig 4.8(a). Specifically, we can calculate the temporal evolution of the pump-induced change of the carrier occupation at state k_0 with pump fluence I :

$$\Delta\rho(t, I) = \rho_{k_0}(t, I) - \rho_{k_0}(-\infty, I)$$

where $k_0 = \omega_L/v_F$ is the most efficiently excited state, ω_L is the carrier frequency of the excitation pulse and v_F is the Fermi velocity in the linear band structure. Some calculated curves of temporal evolution at different pump fluences are shown in Fig 4.8(b). For each $\Delta\rho(t, I)$ curve, we are particularly interested in the peak value during the temporal evolution, i.e.,

$$\Delta\rho_{\text{max}}(I) \equiv \Delta\rho(t_{\text{max}}, I),$$

since it is approximately proportional to the differential transmission spectrum

$$DT \equiv \Delta T/T_0 = (T - T_0)/T,$$

which can be directly measured through optical experiment and T_0 is the transmission with weak pump fluence.

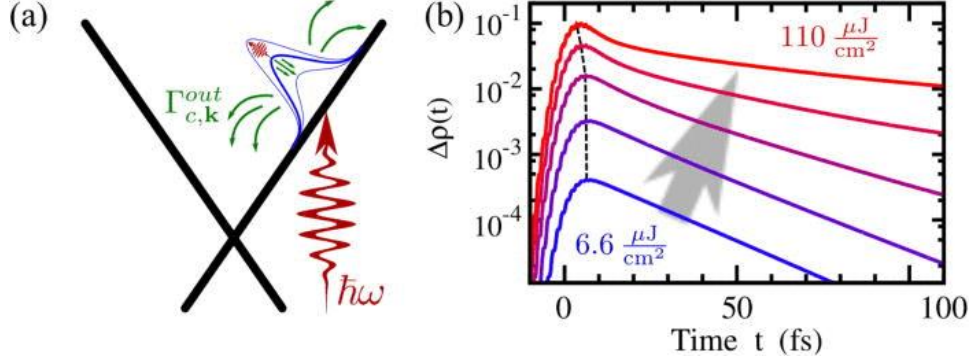


Figure 4.8 Illustration of the optical saturation in graphene. (a) competing processes between carrier scattering (green arrows) and optical pumping (red arrow). (b) Temporal evolution of the pump-induced change in occupation in the most efficiently excited state for various pump fluences. The dashed line indicates the temporal location of the maximum. Adapted from ref ¹³⁰.

We study the saturation of $\Delta\rho_{\max}(I)$ by varying the pump fluence over nine orders of magnitude from 10 pJ/cm² to 26 mJ/cm². As can be seen in Fig 4.9(b), $\Delta\rho_{\max}(I)$ scales almost linearly with the pump fluence up to approximately 0.1 mJ/cm². At stronger excitation, $\Delta\rho_{\max}(I)$ starts to saturate and the overall intensity dependence can be well described with the classical saturable absorption model:

$$\Delta\rho_{\max}(I) \propto \frac{I/I_{\text{sat}}}{1+I/I_{\text{sat}}}$$

where the saturation pump fluence I_{sat} is defined as the required fluence to reach $\Delta\rho_{\max}(I = \infty)/2$ and $I_{\text{sat}} \approx 0.65$ mJ/cm² is calculated. During the action of the pulse, the absorption saturation via Pauli-blocking is competing with the carrier out-scattering from the optically pumped states k_0 which is proportional to $\Gamma_{\lambda,k}^{\text{out}}(t)\rho_k^\lambda(t)$. A higher saturation fluence would correspond to a shorter relaxation time, which occurs when the optically generated carriers are efficiently scattered and spread over an energetically broader range, thus leading to less Pauli-blocking. Now we study each of the relaxation channels. First we discuss the relaxation through the carrier-phonon scattering. Numerical result shows that it is the least efficient scattering process, therefore a small saturation fluence of $I_{\text{sat}} \approx 0.36$ mJ/cm² is obtained when being the only relaxation considered. Second, we inspect the carrier-carrier, and it is clearly seen that the Coulomb scattering is more prominent and can efficiently reduce Pauli-blocking, resulting in a higher saturation fluence of $I_{\text{sat}} \approx 0.52$ mJ/cm². When both carrier-phonon and carrier-carrier

scattering are considered, even higher saturation fluence of $I_{\text{sat}} \approx 0.65 \text{ mJ/cm}^2$ can be calculated. Note the full-dynamics is not a simple sum of all relaxation channels since the different scattering processes compete with each other.

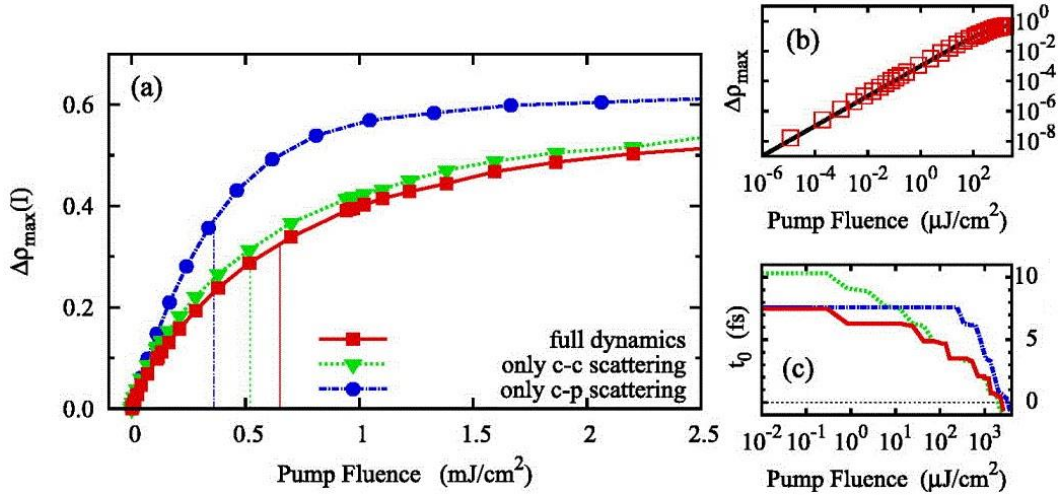


Figure 4.9 Saturation behavior in consideration of different scattering channels. (a) Saturation behavior of (i) all scattering channels (red solid line), (ii) pure carrier-carrier scattering (green dotted line), and (iii) pure carrier-phonon scattering (blue dashed-dotted line). The thin vertical lines indicate the saturation fluence respectively. (b) Full logarithmic plot of the full-dynamics shows a linear range for pump fluences of up to approximately 0.1 mJ/cm^2 . (c) The temporal location t_0 of the maximum with respect to the center of the Gaussian pulse indicates two different regimes for the full-dynamics: (i) at low pump intensities, the saturation resembles the purely phonon-driven dynamics (ii) at higher intensities, the saturation reflects the purely Coulomb-driven dynamics. Adapted from ref ¹³⁰.

Even more physical insights can be obtained by investigating how t_{max} , the temporal location of the maximum $\Delta\rho_{\text{max}}$ with respect to the center of the applied Gaussian excitation pulse, varies with the pump fluence. The relationship is studied on all the cases of carrier-carrier scattering, carrier-phonon scattering, and the combined full dynamics, see Fig 4.9(c). It clearly shows that the full dynamics resembles the purely phonon-driven dynamics at low pump fluence and reflects the purely Coulomb-driven dynamics at high pump fluence. Overall, the full-dynamics results in a saturation that asymptotically connects both regimes. The result indicates that the carrier-carrier scattering dominates the saturation at the regime of strong excitation, and the

carrier-phonon scattering plays the major role in the relaxation dynamics at the regime of weak excitation.

The saturation behavior discussed so far is based on the dynamics of the angle-averaged change of occupation $\Delta\rho_{|k_0|}$. It should be noted that the optically pumped state $k_0 = (|k_0|, \phi)$ depends on the momentum and the angle, where ϕ is typically not resolved in experiments. So far, to calculate $\Delta\rho_{\max}$ we averaged over all polar angles ϕ . This is a good assumption for experiments using multilayer graphene with rotationally stacked layers but not for one using a single layer graphene. The model is indeed appropriate for the 60-layer epitaxial graphene sample for the optical experiment, as we will see immediately in the following.

Section 4.3.2 The optical experiment

To verify the effectiveness of the microscopic theory, we performed the optical experiment to directly measure the transmissions at different pump fluences, converted the data to the differential transmission, and then compared the results to the numerical simulation with the experimental parameters. The experimental setup is shown in Fig 4.10. The excitation source consists of a Ti:Sapphire oscillator (Mira 900-F, Coherent) followed by a Ti:Sapphire regenerative amplifier (RegA 9050, Coherent). The oscillator produces ultrafast optical pulses with a center wavelength of 800 nm (or a photon energy of $\hbar\omega = 1.5$ eV), a pulse width of ~ 56 fs, a pulse energy of $\sim \mu\text{J}$ and a repetition rate of 67 MHz. The regenerative amplifier then subsequently provides a huge gain to the seed pulses from the oscillator through acoustic-optic modulator, converting the $\sim \mu\text{J}$ pulses to the $\sim \text{mJ}$ pulses with a new repetition rate of 250 MHz, which is advantageous in the study of saturation as the intense pump fluence is required. The beam was focused with an 80 mm focal length convex lens to the sample of graphene multilayer on SiC substrate, and the spot size was measured to be $100.6 \mu\text{m}$.

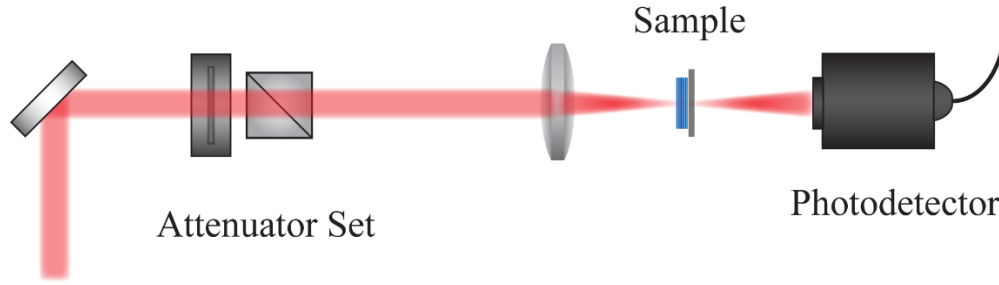


Figure 4.10 Experimental setup for the differential transmission measurements. The 60-layer epitaxial graphene sample on SiC substrate was excited with mJ pulses at the center wavelength of 800 nm. The transmission of the graphene sample and the SiC substrate were measured at different pump fluences.

The sample used in the experiment is a 60-layer epitaxial graphene on the single-crystal silicon carbide (SiC) substrate. Graphene can be epitaxially grown on both the Si-face and the C-face of the SiC substrates by thermal decomposition of Si atoms.¹⁵⁰ The C-face epitaxial growth is more important than the Si-face since it enables the high-quality growth of graphene stacks from a few up to a hundred layers and is compatible with the silicon technology. On the SiC substrate, multilayer epitaxial graphene can grow conformally across atomic sites on the SiC substrate, resulting in large and continuous layers with domain sizes exceeding hundreds of micrometers in size. Importantly, unlike graphite where the graphene layers are coupled through Van der Waal force, the individual layers in multilayer epitaxial graphene are electronically decoupled due to their unique rotational stacking. Each layer therefore preserves the electronic properties of graphene and exhibits Dirac cone near the Dirac points in its band structure.¹⁵¹ Figures 4.11 shows a representative high-resolution scanning tunneling microscopy (STM) image of multilayer epitaxial graphene¹⁵² and the real picture of graphene sample used in the experiment.

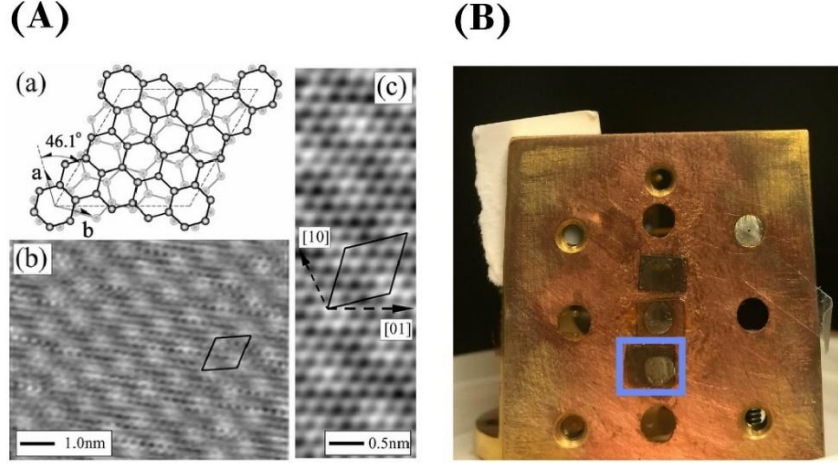


Figure 4.11 Images of multilayer epitaxial graphene (MEG). (A) High-resolution scanning tunneling microscopy (STM) image of MEG (B) Real picture of the MEG sample used in the experiment. Image (A) adapted from ref ¹⁵².

In the optical experiment, we selected 18 different pump fluences I_1, I_2, \dots, I_{18} spanning a range from 0.12 mJ/cm^2 to 7.64 mJ/cm^2 and the corresponding transmissions T_1, T_2, \dots, T_{18} of graphene on substrate were directly measured with a Si-based photodetector. The differential transmissions were then obtained by $DT_i = (T_i - T_1)/T_1$, with T_1 serving as the reference transmission from weak excitation. Note that T_i is the transmission that includes both the contributions graphene and SiC substrate, i.e., $T_i = T_i^g \cdot T_i^{\text{SiC}}$. Therefore, an independent set of SiC substrate transmissions was measured at the same selected pump fluences and the graphene-only transmission is obtained as $T_i^g = T_i/T_i^{\text{SiC}}$. Finally, the differential transmission is calculated as

$$DT_i = (T_i^g - T_1^g)/T_1^g = T_i^g/T_1^g - 1.$$

Now, we focus on a comparison between theory and experiment to quantitatively check our theoretical predictions. The 60-layer epitaxial graphene sample was excited by a 56 fs-pulse with a photon energy of $\hbar\omega = 1.5 \text{ eV}$, and the measured differential transmission is plotted in Fig 4.12 (blue). The experimental data was fitted by the classical saturable absorption model, resulting in a saturation fluence of $I_{\text{sat}}^{(60)} \approx 3.2 \text{ mJ/cm}^2$. We estimate the experimental fluence of a monolayer by assuming each of the 60 layers behaves like a saturable monolayer with

$$\alpha(I_n) = \alpha_0 \left(1 - \frac{I_{n-1}/I_{\text{sat}}}{1 + I_{n-1}/I_{\text{sat}}}\right), \alpha_0 = 2.3\%$$

Neglecting the influence of reflection, we iteratively obtain a lower limit of the saturation fluence of a monolayer of $I_{\text{sat}}^{(1)} \approx 1.5 \text{ mJ/cm}^2$.

Applying the same experimental parameters in the simulation, we calculate a saturation fluence for a monolayer of $I_{\text{sat}}^{\text{theory}} \approx 2.6 \text{ mJ/cm}^2$, which is in very good agreement with the data, see Fig 4.12. Note that the theoretically predicted value is between the 60-layer saturation $I_{\text{sat}}^{(60)}$ and the monolayer saturation $I_{\text{sat}}^{(1)}$, confirming the accuracy of the simulation.

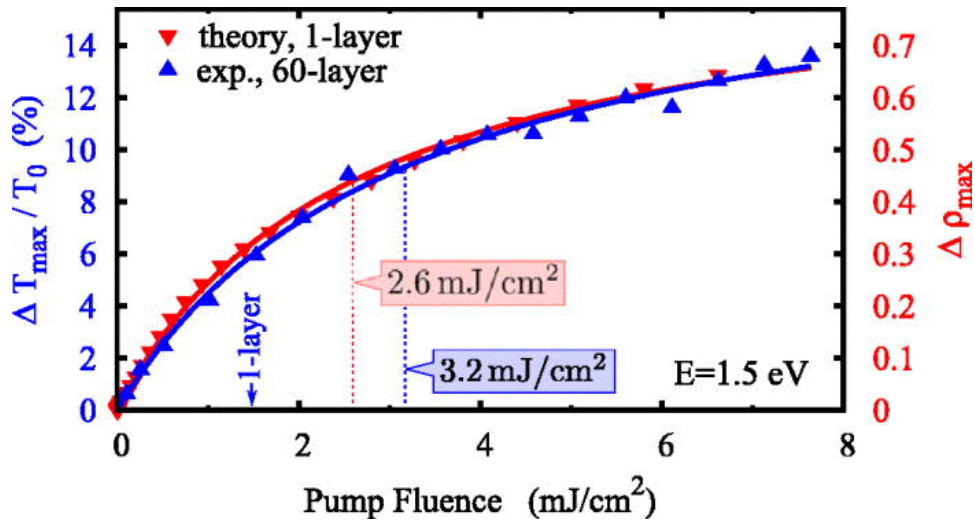


Figure 4.12 Experimentally determined saturation of transmission.(blue) experimental result of a 60-layer sample and a 56 fs-pulse with a photon energy of 1.5 eV (red) the corresponding microscopic calculation. A direct comparison shows an excellent agreement. Adapted from ref ¹³⁰.

In conclusion, the pump-induced change in transmission scales linearly with the fluence in a low intensity regime and saturates nonlinearly at higher fluences. The comparison between microscopic calculations and experimental results shows that the saturation behavior as an interplay between Pauli-blocking and scattering-induced redistribution of excited carriers.

Section 4.4 Light field camera with graphene focal stack

Section 4.4.1 All-Graphene Heterojunction Photodetector

The discovery of graphene has sparked interest in a whole class of atomic layer crystals including graphene, h-BN, MoS₂ and other TMDs. Unlike conventional semiconductors, their ultimate thinness (one or few atomic layers) make them nearly transparent across the electromagnetic spectrum. Despite this, the strong light-matter interaction in these 2D atomic crystals makes them sensitive light sensors at the same time. It may seem a paradox that a sensitive detector could also be nearly transparent, but this combination of properties is uniquely exhibited by these 2D electronic materials. In this section, we discuss how a highly transparent photodetector with great sensitivity can be realized with graphene and demonstrate the direct application of these detectors for constituting the transparent focal stack in a proof-of-concept single-pixel light field camera.

Recently, a graphene photodetector with high responsivity that preserves the ultra-broadband detection was reported.¹²⁹ It consists of two graphene layers sandwiching an ultra-thin tunneling barrier and has an architecture of field effect transistor (FET). When light is absorbed by both graphene layers, asymmetric tunneling between the two layers can occur and the photo-gating effect is induced. The photo-gating can critically modify the conductivity of the channel graphene and thus provide huge phototransistor gain. This is the foundation of the all-graphene heterojunction photodetector developed for the application of focal stack light field camera in this section, and hence we will discuss in more detail about its fabrication and the working principle. Note however, that since it was originally designed only as a conventional photodetector, additional modifications must be made to make it highly transparent, elaborated on below.

The graphene photodetector is based on a double-layer graphene heterostructure and its schematic is shown in Fig 4.13. The back gate is formed by a p-doped silicon wafer with 285 nm thermal oxide, allowing the electrical gating of the bottom layer graphene. A 6-nm-thick intrinsic silicon layer was chosen as the tunnel barrier and sandwiched by two graphene layers, where the bottom layer works as the channel and the top layer works as a floating top gate. The drain-source current is generated when a voltage bias is applied across the source and drain. The graphene layers used in the work were grown by chemical vapor deposition (CVD) on copper foil and then transferred with the Poly (methyl methacrylate) (PMMA) method.

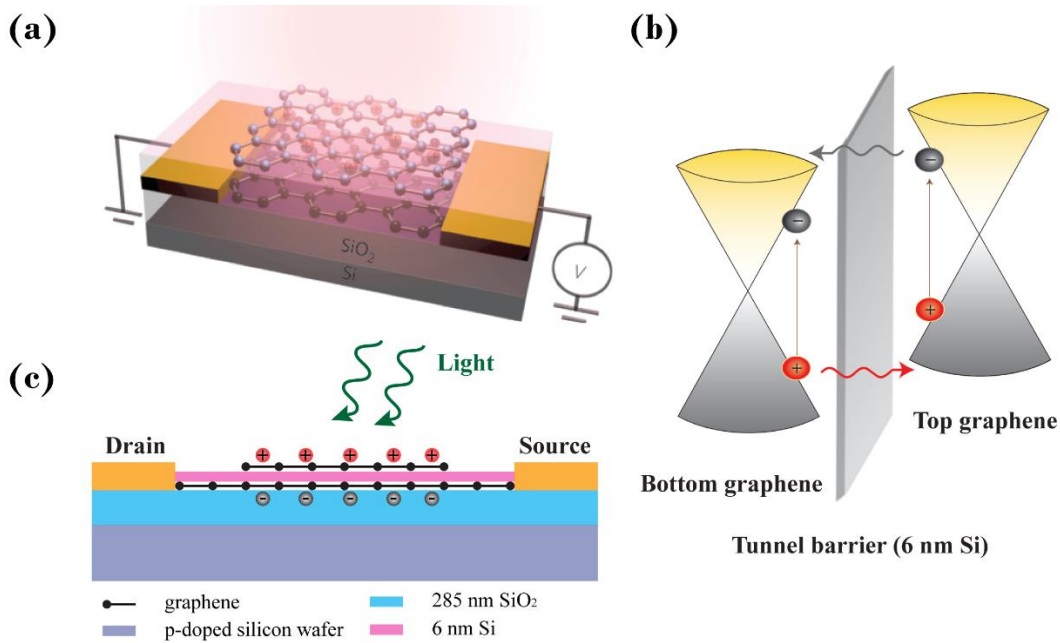


Figure 4.13 Device structure and working mechanism of the graphene photodetector. (a) The device structure. (b) The energy diagram and asymmetric tunneling under light illumination. (c) The layer-by-layer schematic demonstrating the photo-gating effect under light illumination. (a) and (b) are adapted from ref ¹²⁹.

The operating principle of the double-layer graphene photodetector can be understood from the band diagram shown in Fig 4.13(b). The top-layer graphene is more heavily p-doped compared to the bottom-layer graphene and the average Fermi energy difference is about 0.12 eV. Because of the doping difference, charge transfer would occur to equilibrate the Fermi level of the two graphene layers, leading to the tilted energy band in the tunnel barrier. As a result, when light is absorbed by the two graphene layers, the tunneling of electrons and holes are asymmetric: electrons tunnel preferentially from the top-layer graphene to the bottom-layer graphene while holes tunnel preferentially from bottom to top, as indicated by Fig 4.13(b). After tunneling, the tunneled electrons and holes are physically separated, and therefore they do not recombine in ultrashort time. During the time (τ_{lifetime}) when the charges remain trapped in the separated two graphene layers, the bottom graphene channel is gated by the top graphene, see Figure 4.13(c). As the gating effect takes place under light illumination, it is called photo-gating effect. The device therefore operates as a phototransistor with its top gate controlled optically. In a phototransistor,

the photoconductive gain, which is the ability to provide multiple electrical carriers per single incident photon, is determined by $\tau_{\text{lifetime}}/\tau_{\text{transit}}$ where τ_{lifetime} is the lifetime during which the tunneled carriers remain trapped in the two graphene layers and τ_{transit} is the transit time inversely proportional to the mobility of the channel material. It can be seen directly that the graphene phototransistor gain is benefited greatly from the high mobility of graphene and the strategy to extend the lifetime with tunnel barrier. The origin of the phototransistor gain can be understood with a simple physical picture that, the short transit time allows the photo-generated carriers to circulate in the circuit multiple times before recombination, equivalent to the generation of multiple times more photoexcited carriers.¹⁵³

Now we focus on the design of the all-graphene heterojunction photodetector that is to be used as the transparent focal stack in the light field camera application. As the ultimate goal is to develop a highly transparent detector, some redesign must be made to the photodetector discussed above. The schematic of the transparent all-graphene heterojunction photodetector is shown in Fig 4.14(a, b). On a transparent glass substrate, the back gate is now implemented with a bottom monolayer graphene and 40 nm Al_2O_3 , which is deposited as the back gate dielectric using atomic layer deposition (ALD) technique. Two more layers of graphene, working as the channel and the top gate, were then placed with a 6 nm Ta_2O_5 thin tunnel layer sandwiched in between. We select Ta_2O_5 over the intrinsic Si since it is a wide-bandgap material and therefore is transparent in the visible range. Furthermore, to make the entire operating device transparent, we eliminate the use of metal within the transparent window by replacing metal with graphene as the interconnect, and metal pads for wire-bonding and measurement purpose are all located outside the transparent windows. Devices with two different transparent window sizes ($200 \times 200 \mu\text{m}^2$ and $5 \times 5 \text{mm}^2$) were fabricated. Fig 4.14(c) shows the actual fabricated all-graphene transparent photodetectors with both designs on a printed Univ. of Michigan “M” logo. Even with the bare eyes, we can obviously see through the whole device and thus confirm its high transparency. At $1.2 \mu\text{m}$ laser excitation, the prototype device achieves a photoresponsivity greater than 20 A/W under 1 V bias voltage, comparable to previous non-transparent graphene photodetector.

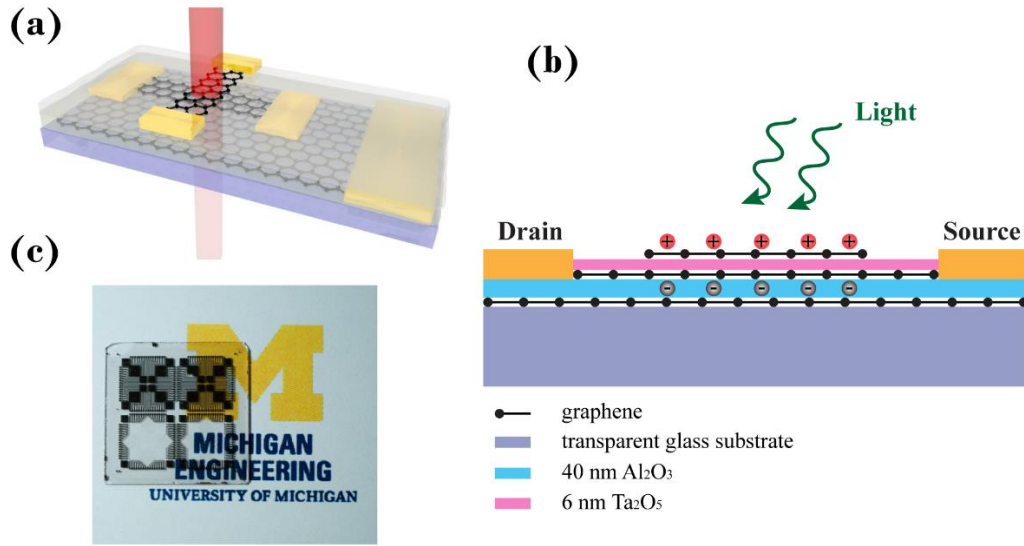


Figure 4.14 The all-graphene transparent heterojunction photodetector. (a) the device structure and (b) the layer-by-layer schematic (c) the actual fabricated all-graphene transparent heterojunction photodetectors on a sheet of paper with Univ. of Michigan “M” logo printout. Photo (a) and (c) adapted from ref ¹⁵⁴.

Section 4.4.2 Prototype single-pixel camera with graphene detectors

A light field camera, in contrast to a conventional camera that records 2D images, captures the high-dimensional data called light field. Light field is essentially the radiance function of monochromatic rays in the 3D space, with each ray specified by its emanating direction (with two angular parameters) and anchor point (with two spatial parameters) defined on a reference plane. Light field therefore, is a 4D function. A complete knowledge of the scene light field is of great interest, since the transformation on the light field function corresponds to the redirection of the rays. Examples of light field applications are digital refocusing, novel view rendering, depth estimation and synthetic aperture photography.¹⁵⁵ It has been demonstrated that 4D light field can be directly captured on a 2D sensor, with the employment of a microlenses array at the focal plane of the imaging lens that multiplexed the angular information.¹⁵⁶ This approach, however, has an inherent tradeoff of spatial resolution for angular resolution.

In this study, we propose a novel scheme of light field camera. The camera consists of a main camera lens, followed by multiple transparent sensor arrays stacked along the path of the light rays. The set of 2D images captured on the sensor corresponding to different focusing conditions is called *focal stack*. The key technology that enables the *simultaneous* capture of the

focal stack data is the all-graphene transparent detector discussed previously. The 4D light field can then be reconstructed with the sparse 3D focal stack with a model-based approach, which is the focus of next chapter.

It is a major technological step from demonstrating a single pixel to a dense 2D sensor array (which is not available at this stage). Nevertheless, here we demonstrate a key operating principle of focal stack light field imaging, particularly the ability to section (image a particular focal plane), or perform optical ranging. To accomplish this, we used two single-pixel graphene photodetectors on transparent substrates; the experimental scheme is shown in Fig 4.15.

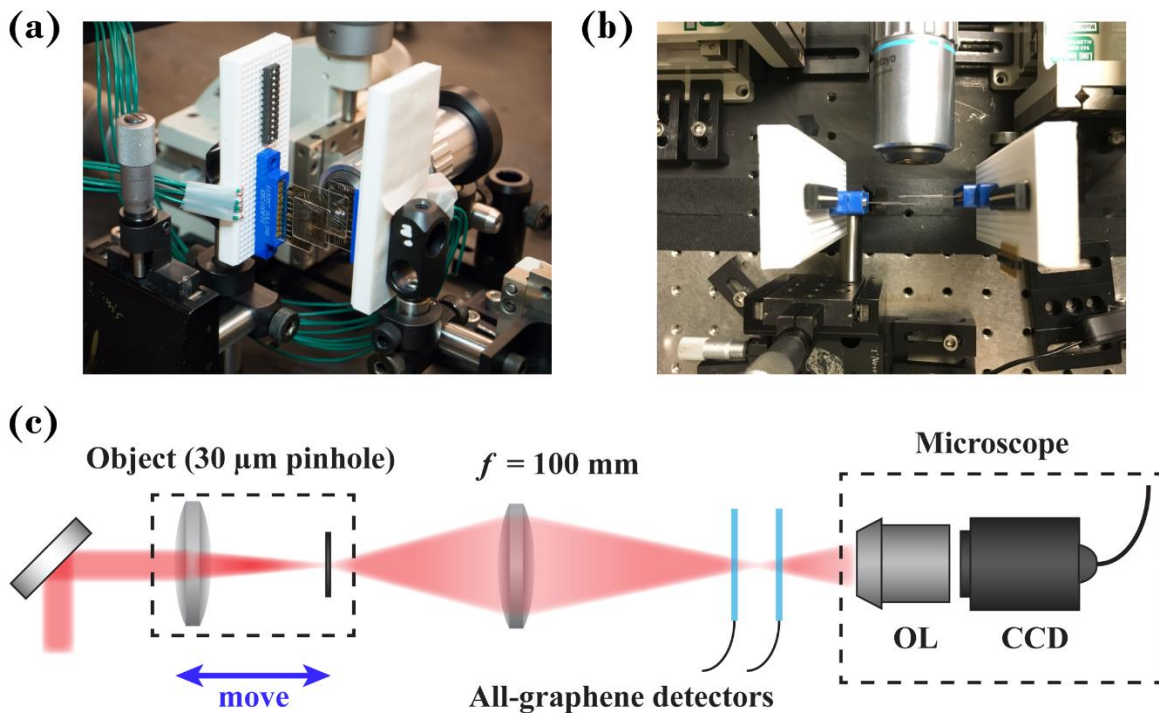


Figure 4.15 Prototype single-pixel focal stack camera. (a) cross-sectional (b) and top-down views of two stacking all-graphene transparent heterojunction broadband photodetectors along the light propagation direction. (c) Schematic of one-dimensional light field photodetection optical imaging system. Photo (a) and (b) adapted from ref ¹⁵⁴.

For the demonstration, we employed a 10 cm focal length front imaging lens and two transparent graphene detectors that are 2 mm apart. Behind the focal stack, a microscope provides separate confirmation that the test object is perfectly imaged at the center of each graphene detector

pixel. The test object is a point source formed by illuminating a 30 μm pinhole with the focused 632 nm HeNe laser. The point source, the center of the imaging lens, the two single-pixel detectors, and the optical axis of the microscope system are well aligned on the same optical axis (referred to as the z axis).

In the experiment, we recorded 10 sets of the front and back detector signal currents, which correspond to the 10 different positions of the illuminating pinhole from the farthest to the nearest with respect to the front lens, see Fig 4.16 (data points are indexed 1 to 10 from left to right). When the point source is very far from the imaging lens, the real image is completely out of focus on both of the front and the back graphene detector sheets. We then move the point source toward the imaging lens with a linear stage. At some point, the real image of the point source is perfectly focused on the front detector sheet while staying out of focus on the back detector sheet. The signal current of the front detector reaches its maximum, as it is proportional to the optical intensity illuminated. This corresponds to the 1st data points in Fig 4.16. As we continue to move the point source toward the imaging lens, the intensity of the real image decreases on the front detector sheet and increases on the back detector. At some point, the point source is sharply imaged on the back detector sheet while staying out of focus on the front detector sheet, corresponding to the last data points in Fig 4.16.

The curves demonstrate optical ranging or sectioning; with knowledge of the lens focal length and sensor positions, the longitudinal position of the object can be determined. In the figure, we normalize the object position to the Rayleigh range of the imaging system. In principle, high axial resolution can be obtained by imaging with a short focal length lens, e.g. a microscope objective. The axial resolution will be determined simply by the Rayleigh range/depth of field of the optic used in the imaging system, as it is in a traditional confocal microscope. Knowing the intensity profile along the z axis, we can extract the depth information of the scene from the data. The design can be readily extended to a 3D focal stack when high quality graphene detector arrays become available.

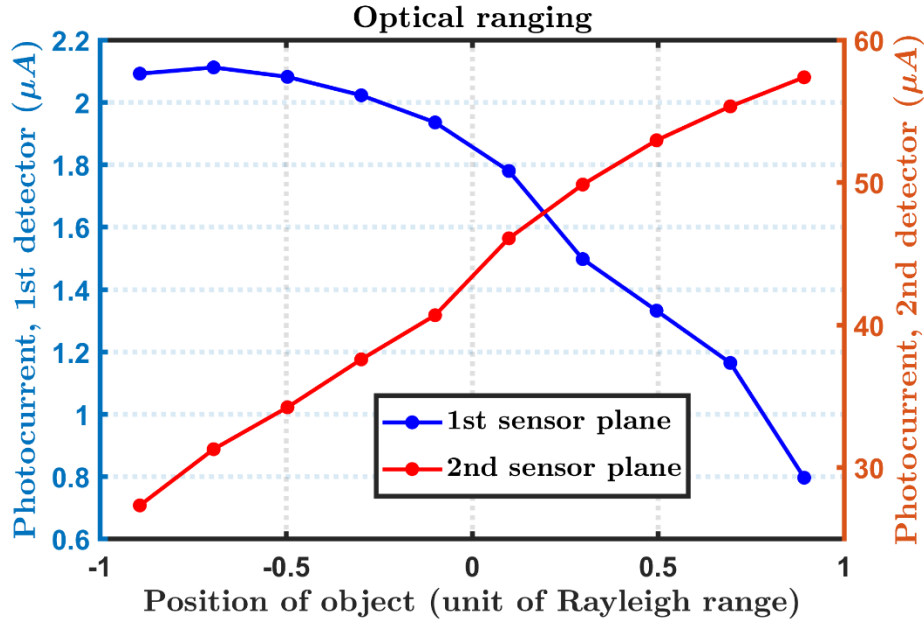


Figure 4.16 Demonstration of optical ranging. Photocurrent measured for the two all-graphene photodetectors (separated by 2 mm) at various positions of the point object. In principle the longitudinal position of the object can be determined with the knowledge of the lens focal length and sensor positions.

Section 4.5 Summary

In the chapter, we presented two studies regarding the optics of graphene. In the first part, a microscopic model that accounts for the optical saturation behavior of graphene was presented. The model includes both the mechanisms of carrier-carrier and carrier-phonon scattering, and its theoretical prediction is shown to be consistent with the differential transmission measurements of multilayer epitaxial graphene excited by the ultrafast optical pulses.

In the second part, we presented the applications of graphene in photodetection and imaging system. A novel light field imaging scheme was proposed that consists of a main camera lens followed by a set of graphene transparent detector arrays, which allows the simultaneous capture of 2D images under different focusing conditions. The proof-of-concept single-pixel focal stack light field camera was built and its key operating principle to perform optical ranging was demonstrated experimentally.

CHAPTER 5

Light Field Reconstruction from a Focal Stack

Section 5.1 Introduction

The advent of digital photography is a milestone in camera history. The ability to post-process the image data opens the new era of modern photography. Over the past two decades, the leap in computation power and advances in hardware manufacturing have further encouraged camera designers to explore and rethink new ways to acquire and process the visual information. In particular, attempts were made to capture the high-dimensional data sets that contain richer scene information than the 2D photographic images recorded by the conventional cameras. In fact, conventional images can be understood as simply the 2D projections of the high-dimensional data, and great details about the scene are lost within the image formation process of the conventional camera.

Even with the increasing processing power, an important question to ask is: what kind of information should we record on the digital sensor, so that with suitable processing, we can reconstruct an image that may have better quality or there may be new functionality in the imaging system. It turns out that, the 4D radiance function of rays in the 3D space, called *light field*, is the efficient high-dimensional data that enables new applications such as digital refocusing, novel view rendering, depth estimation and synthetic aperture photography.¹⁵⁷ The reinterpretation of the classic photographic imaging procedure that separates the process of imaging a scene (i.e., scene capture) from the actual realization of an image (i.e., image synthesis), is the key that offers new flexibility in terms of post-processing.¹⁵⁵ The 2-D images presented to the human observer are processed versions of the higher-dimensional data acquired by sensors, and only the computer

sees in their raw form. This partial replacement of physics by computation enables the post-capture modification of images on a previously unimaginable scale.

The device that aims at the acquisition, processing and rendering of light field, is called light field camera. In optical design terms, light field camera presents a completely different perspective from the convention camera. For a long time, optical resolution is the primary metric to be optimized, and when thinking in terms of two conjugate planes, the task being to design the lens system that is light-efficient in collecting the light emanating from a point on the object plane and converging it a point on the image plane. Light field camera on the other hand, focuses on acquiring the data that is essential for the complete recovery of full 3-D content of a scene and purposefully images out-of-focus regions in many cases. Various schemes for light field imaging have been proposed and demonstrated. For example, one may employ an array of microlenses at the focal plane of the imaging lens, in conjunction with a 2D detector array, to obtain the angular information necessary to reconstruct the light field. The first prototype was implemented by Ng et al. in 2005,¹⁵⁶ and imaging devices of this type are referred to as plenoptic cameras. This approach, however, has an inherent tradeoff of spatial resolution for angular resolution. Schemes incorporating programmable apertures,¹⁵⁸ multi-camera array¹⁵⁹ and other mask-based designs^{160,161} attempt to solve the low-resolution problem, but they either suffer from signal-to-noise limitations or require multiple images to be acquired and therefore are not suitable for recording dynamic scenes. Implementing a full-sensor-resolution, high SNR and real-time light field imaging system remains a challenging problem.

With recent advances in optoelectronic materials, a team at University of Michigan has proposed a novel light field camera that uses the state-of-art all-graphene transparent detector (discussed in the previous chapter) to capture the focal stack, a set of 2D images under different focusing conditions. *Simultaneous* acquisition of the focal stack data is enabled by the stacked, highly transparent detectors. In this chapter, we present a framework for 4D light field reconstruction of the scene from the focal stack data, covering the light field transport, the image formation process, and the camera operations such as refocusing and image rescaling. We further proposed a focal stack design rule based on the equally angular-spaced Fourier sampling. A model-based light field reconstruction was then performed with the synthetic photorealistic scene, where

the light field applications of all-in-focus image extraction and multi-view stereo were demonstrated.

Section 5.2 Overview of light field

Visual information is a result of complex interactions between the lighting, object geometry, materials, observer location, and the characteristic of the human visual systems (or of the imaging sensors). To generate a photorealistic image, all the parameters must be precisely modeled or specified, and numerous computations are required to simulate the process of the interactions.¹⁶² Instead of modeling this complexity (as computer graphics is doing), the plenoptic function is proposed to accommodate for all the possible variations of light without referring to an underlying model within the framework of geometric optic. It is a purely phenomenological description of the light distribution that assigns a radiance value to rays propagating within a physical 3D space. In the most general form, it adopts a seven-dimensional description: arbitrary radiance values can be assigned at every position of space, for every possible propagation direction, for every wavelength, and for every point in time, denoted as $\ell(x, y, z, \theta, \phi, \lambda, t)$ with the unit of $\text{W}/\text{m}^2/\text{sr}/\text{nm}/\text{s}$ which describes the spectral radiance per unit time, (x, y, z) is a spatial position, (θ, ϕ) is an incident direction, λ is the wavelength of light, and t is a temporal instance.¹⁶³

While the 7D plenoptic function records the complete information of a scene, its high-dimensional nature makes it expensive and difficult to sample, process, and store. Therefore, several constraints are imposed to reduce its dimensionality and make it practical for real applications: (i) it is assumed to be time-invariant, hence the temporal dimensional can be removed. (ii) it is considered as monochromatic, though the same reasoning can be applied to the color channels independently. (iii) assume the presence of a convex boundary surface S that separates the space into the inside part which contains the scene of interest and the outside part that is empty space (e.g. without occluding objects). In this case, rays from the convex hull of the scene to the outside space can propagate without loss, and hence the radiance is constant along the rays. An additional dimension can then be removed since the radiance conservation introduces a correlation between spatial positions. The 7D plenoptic function therefore, reduces to a 4D scalar-

valued function of $S \times S_{\dagger}^2$, where S_{\dagger}^2 is the hemisphere of directions toward the outside, termed *light field*.¹⁶⁴ In essence, light field is a data structure that supports efficient interpolation of the radiance estimates along specified rays.¹⁶⁵ Following the same reasoning, in 2D space the resulting light field is 2D. In the following discussion, we choose to discuss the framework in the 2D space as it permits a concise formulation, and it is straight forward to extend the result to 3D space (4D light field).

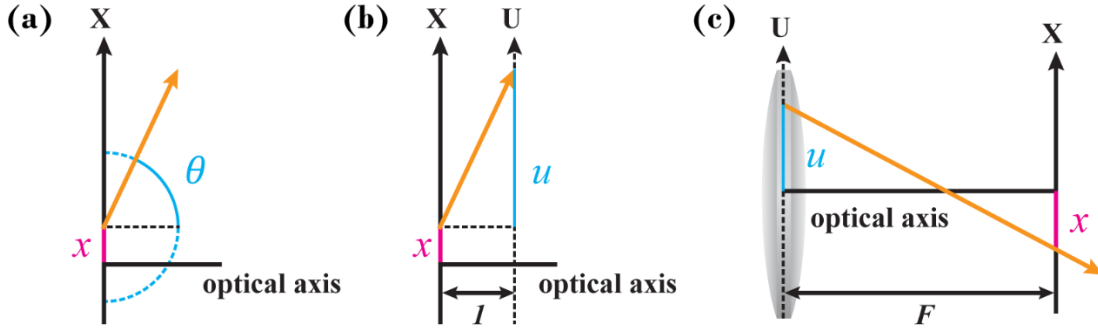


Figure 5.1 Light field parameterizations. (a) plane-sphere parameterization, (b) plane-plane parameterization and (c) in-camera parameterization.

There are several ways to parameterize the light field, and each can be advantageous in the specific applications (Fig 5.1). To describe the light field in the free space, the most popular choices are the *plane-sphere parameterization* and the *plane-plane parameterization*. In both cases, a plane p in the outside space is first chosen as the reference plane (called light field plane) and is perpendicular to the optical axis. Suppose a ray propagating from the convex hull of scene S intersects with plane p at position x . For the plane-sphere parameterization, the ray passing through position x with an angle θ with respect to the optical axis is specified as (x, θ) . For the plane-plane parameterization, a second plane q that is parallel to p and unit distance apart is constructed. The ray passing through position x on plane p with a transverse displacement u on plane q is specified by (x, u) . Under paraxial approximation, $\theta \approx u$ and the two parameterizations converge. To describe the light field in the camera, the *in-camera parameterization* assigns the two reference planes to the aperture plane and the sensor plane, and a ray that intersects with the sensor plane at x and the aperture plane at u is parameterized as (x, u) . The in-camera

parameterization is preferably adopted ^{166,167} as it permits a concise form for the image formation operation within the camera, which will be elaborated in the next section. For all the three cases, x is called *spatial* coordinate and $\theta(u)$ is called *directional* coordinate. It should be noted that the light field parameterization is always linked to a particular light field plane. Changing the plane in general, changes the configuration of the parameterized light field.

Section 5.3 Design of the focal stack light field camera

Section 5.3.1 Light field transport and camera modeling

The key technology at the center of the proposed scheme is a transparent photodetector. Present imaging systems employ a single optical sensor (photodetector array), usually at the focus of a lens system. Being made of silicon or similar material, the sensor is opaque, resulting in the loss of directional information on the light ray. If we could make highly sensitive but nearly transparent sensors, then multiple sensor arrays could be stacked along the path of the light rays, enabling directional information to be retained, and thus computational reconstruction of the light field in a single exposure. Recent breakthroughs in novel optoelectronic materials enable this new imaging paradigm to be realized. To perform the model-based light field reconstruction from the focal stack data, it is essential to derive the camera model and we start with the formulation of the light field transport. The analysis is performed in 2D space as it is mathematically compact. Extension of the result to 3D space (4D light field) will also be covered.

Consider first the light field propagating for a distance d in free space. With straight forward ray tracing in the plane-plane parameterization, the initial light field (ℓ) and the final light field (ℓ') are related through:

$$\ell' \left(\begin{bmatrix} x \\ u \end{bmatrix} \right) = \ell \left(T_d \begin{bmatrix} x \\ u \end{bmatrix} \right), \text{ where } T_d = \begin{bmatrix} 1 & -d \\ 0 & 1 \end{bmatrix}.$$

As can be seen, the resulting light field corresponds to a horizontal shear of the initial light field in the $x - u$ domain (called epipolar domain).

Next consider the light refraction by lens with focal length f . Under paraxial approximation, Snell's law is simplified such that the operation can be linearly expressed in the plane-plane parameterization as:

$$\ell' \left(\begin{bmatrix} x \\ u \end{bmatrix} \right) = \ell \left(R_f \begin{bmatrix} x \\ u \end{bmatrix} \right), \text{ where } R_f = \begin{bmatrix} 1 & 0 \\ \frac{1}{f} & 1 \end{bmatrix}.$$

As can be seen, the resulting light field corresponds to a vertical shear of the initial light field in the epipolar domain.

Now we consider the process of scene light field transport onto the sensor plane in a camera. Assume a linear scene corresponding to a 1D object, with a reflectance using plane-plane parameterization. As the light field plane is set to agree with the 1D object, the reflectance directly defines the scene light field. The light field first travels a distance of z to a lens with focal length f and is then imaged onto a 1D sensor that is distance F behind the lens, see Fig 5.2.

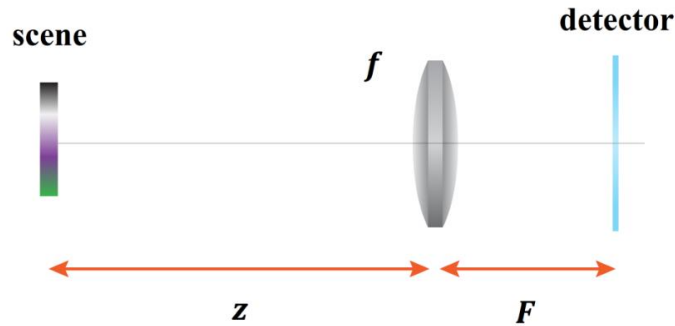


Figure 5.2 Schematic of light field transport in the photography process. The light field first travels a distance of z , then refracted by the imaging lens of focal length f , and finally propagates a distance of F to land on the detector.

In the absence of aperture, the light field on the sensor film can be traced by the serial application of optical transfer matrices:

$$\ell_{\text{sensor}} \left(\begin{bmatrix} x \\ u \end{bmatrix} \right) = \ell_{\text{scene}} \left(C_{z f F} \begin{bmatrix} x \\ u \end{bmatrix} \right), \text{ where } C_{z f F} = T_z R_f T_F = \begin{bmatrix} 1 - \frac{z}{f} & zF \left(\frac{1}{f} - \frac{1}{z} - \frac{1}{F} \right) \\ \frac{1}{f} & 1 - \frac{F}{f} \end{bmatrix}.$$

Practically, a finite size aperture is always present in the camera which should be considered. The effect can be included by incorporating a spatial *rect* function D_x at the stage after the lens refraction:

$$\ell_{\text{lens}} \left(\begin{bmatrix} x \\ u \end{bmatrix} \right) = \ell_{\text{scene}} \left(\text{T}_z \text{R}_f \begin{bmatrix} x \\ u \end{bmatrix} \right) \cdot \Pi_d \left(\begin{bmatrix} x \\ u \end{bmatrix} \right), \text{ where } D_x \left(\begin{bmatrix} x \\ u \end{bmatrix} \right) = \text{rect} \left(\frac{x}{D} \right).$$

and then propagate a distance F to the sensor plane:

$$\ell_{\text{sensor}} \left(\begin{bmatrix} x \\ u \end{bmatrix} \right) = \ell_{\text{scene}} \left(\text{T}_z \text{R}_f \text{T}_F \begin{bmatrix} x \\ u \end{bmatrix} \right) D_x \left(\text{T}_F \begin{bmatrix} x \\ u \end{bmatrix} \right) = \ell_{\text{scene}} \left(\text{C}_{zff} \begin{bmatrix} x \\ u \end{bmatrix} \right) D_x \left(\text{T}_F \begin{bmatrix} x \\ u \end{bmatrix} \right).$$

The image formation $i(x)$ on the sensor plane is the integration of the sensor light field along the directional dimension u , i.e.,

$$\mathcal{J}(x) = \int_{u_l}^{u_u} \ell_{\text{sensor}}(x, u) du.$$

Note $D_x \left(\text{T}_F \begin{bmatrix} x \\ u \end{bmatrix} \right)$ is now a vertically sheared rectangle function. It therefore imposes the x dependent lower bound $u_l(x)$ and upper bound $u_u(x)$ for the integration, which is not preferred in the computation. The in-camera parameterization is introduced to rectify the coordinate, making dimension x on the sensor plane (spatial) and dimension u on the aperture plane (directional). The transformation between the in-camera and the plane-plane parameterization can be derived as:

$$\ell_{\text{cam}} \left(\begin{bmatrix} x \\ u \end{bmatrix} \right) = \frac{1}{F} \ell_{\text{sensor}} \left(\text{P}_F \begin{bmatrix} x \\ u \end{bmatrix} \right), \text{ where } \text{P}_F = \begin{bmatrix} 1 & 0 \\ \frac{1}{F} & -\frac{1}{F} \end{bmatrix}.$$

The front factor of $1/F$ comes from the radiance conservation, which is not important in the analysis and will be omitted for simplicity. With the re-parameterization, the resulting light field in the camera coordinate now becomes

$$\ell_{\text{cam}} \left(\begin{bmatrix} x \\ u \end{bmatrix} \right) = \ell_{\text{scene}} \left(\text{C}_{zff} \text{P}_F \begin{bmatrix} x \\ u \end{bmatrix} \right) D_x \left(\text{T}_F \text{P}_F \begin{bmatrix} x \\ u \end{bmatrix} \right) = \ell_{\text{scene}} \left(\text{H} \begin{bmatrix} x \\ u \end{bmatrix} \right) D_u \left(\begin{bmatrix} x \\ u \end{bmatrix} \right)$$

where $\text{H} = \text{C}_{zff} \text{P}_F = \begin{bmatrix} -\frac{z}{F} & 1 - \frac{z}{f} - \frac{z}{F} \\ \frac{1}{F} & \frac{1}{f} - \frac{1}{F} \end{bmatrix}$ and $D_u \left(\begin{bmatrix} x \\ u \end{bmatrix} \right) = \text{rect} \left(\frac{u}{D} \right)$.

It is seen that now the integration is over the aperture plane, i.e.,

$$\mathcal{J}(x) = \int_{-D/2}^{+D/2} \ell_{\text{cam}}(x, u) du$$

and u_l, u_u are no longer dependent on x . With the parameters of $z = 500$ mm, $f = 50$ mm, $D = 30$ mm and $F = 50$ mm, the transformation of light field at each stage is illustrated in Fig 5.3:

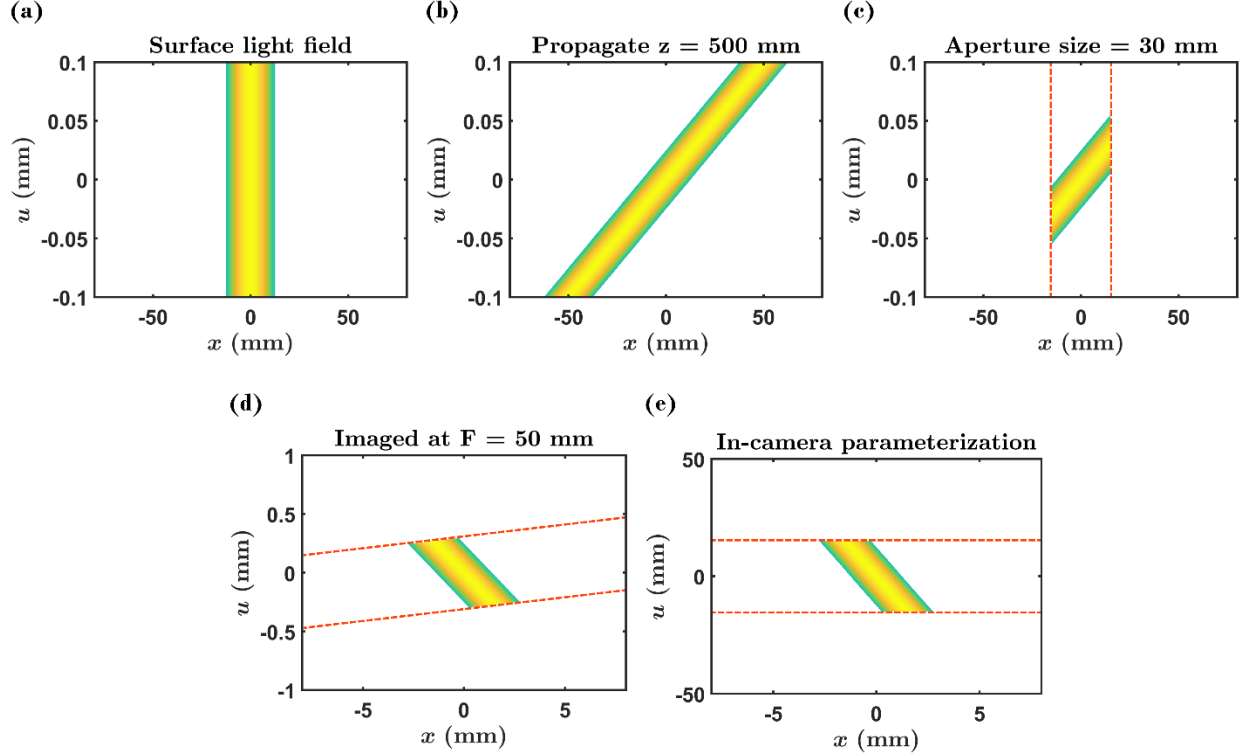


Figure 5.3 Light field transformation in the photography process. (a) The surface light field. (b) The light field observed at the lens plane that is units away from the surface. (c) The light field modulated by the blocking function of the aperture. The dotted lines define the width of the aperture. (d) The light field observed at the image plane. (e) The light field represented by the in-camera parameterization.

The formulation can be directly generalized to the 3D space (4D light field):

$$\ell_{\text{cam}} \left(\begin{bmatrix} x \\ u \end{bmatrix}, \begin{bmatrix} y \\ v \end{bmatrix} \right) = \ell_{\text{scene}} \left(H \begin{bmatrix} x \\ u \end{bmatrix}, H \begin{bmatrix} y \\ v \end{bmatrix} \right), \text{ where } H \text{ is defined as above.}$$

This can be rewritten in the form of more concise notations:

$$\ell_{\text{cam}} \left(\begin{bmatrix} x \\ u \end{bmatrix} \right) = \ell_{\text{scene}} \left(H \begin{bmatrix} x \\ u \end{bmatrix} \right)$$

where the bold characters $\mathbf{x} = \begin{bmatrix} x \\ y \end{bmatrix}$ and $\mathbf{u} = \begin{bmatrix} u \\ v \end{bmatrix}$ represent the 2D spatial and angular vector respectively.

Section 5.3.2 Light field imaging and transformation

The core of the model-based reconstruction is the derivation of the forward model A , such that $y = Ax$ where y is the measurement and x is the signal to be reconstructed. Specifically, for focal stack light field camera we seek to formulate

$$\mathcal{f} = \mathcal{A} \cdot \ell$$

where \mathcal{f} is the focal stack images on the camera sensors, \mathcal{A} is the *forward model* and ℓ is the in-camera light field on the last film. In the end, we will derive its discrete form. As mentioned earlier, the focal stack \mathcal{f} is a set of images taken with different focusing conditions. In our proposed scheme, this is achieved by placing a set of transparent sensor films with different distances to the main camera lens, see Fig 5.4.

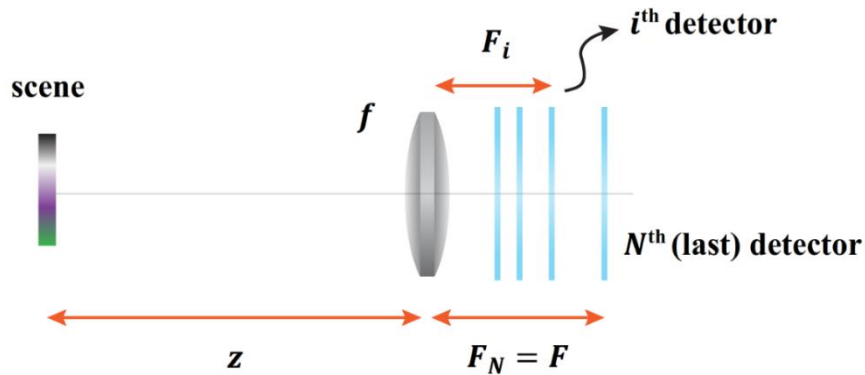


Figure 5.4 Schematic of the proposed focal stack camera. N sets of transparent sensor films are placed at different distances $[F_1, \dots, F_i, \dots, F_N]$ with respect to the camera lens.

We have previously seen that the process of scene light field captured on the sensor plane can be modeled with the transformation $\ell_{\text{cam}} \left(\begin{bmatrix} \mathbf{x} \\ \mathbf{u} \end{bmatrix} \right) = \ell_{\text{scene}} \left(\text{H} \begin{bmatrix} \mathbf{x} \\ \mathbf{u} \end{bmatrix} \right)$. In fact, camera operations such as refocusing and image scaling can also be described by the corresponding transformations, as the process only involves linear redirection of the rays. While the transformations can be obtained with geometric optics, we can derive them more elegantly with simple function mappings

as follow. With the camera configuration in Fig 4.5, suppose the scene light field is ℓ_0 , the in-camera light field on the i^{th} film is ℓ_i and we have

$$\ell_i \left(\begin{bmatrix} \mathbf{x} \\ \mathbf{u} \end{bmatrix} \right) = \ell_0 \left(H_i \begin{bmatrix} \mathbf{x} \\ \mathbf{u} \end{bmatrix} \right), \text{ where } H_i = \begin{bmatrix} -\frac{z}{F_i} & 1 - \frac{z}{f} - \frac{z}{F_i} \\ \frac{1}{F_i} & \frac{1}{f} - \frac{1}{F_i} \end{bmatrix}$$

Now if we set the N^{th} (last) film as the reference plane and express ℓ_i in terms of ℓ_N :

$$\ell_i \left(\begin{bmatrix} \mathbf{x} \\ \mathbf{u} \end{bmatrix} \right) = \ell_0 \left(H_i \begin{bmatrix} \mathbf{x} \\ \mathbf{u} \end{bmatrix} \right) = \ell_N \left(H_N^{-1} H_i \begin{bmatrix} \mathbf{x} \\ \mathbf{u} \end{bmatrix} \right) = \ell_N \left(H_i^F \begin{bmatrix} \mathbf{x} \\ \mathbf{u} \end{bmatrix} \right),$$

$$\text{where } H_i^F = H_N^{-1} H_i = \begin{bmatrix} \frac{F_N}{F_i} & 1 - \frac{F_N}{F_i} \\ 0 & 1 \end{bmatrix}.$$

H_i^F therefore represents the transformation that refocuses light field from the N^{th} film to the i^{th} film, and the i^{th} focal stack image is $\mathcal{J}_i(\mathbf{x}) = \int \ell_N \left(H_i^F \begin{bmatrix} \mathbf{x} \\ \mathbf{u} \end{bmatrix} \right) d\mathbf{u}$, where the integration is over the aperture. From the perspective of linear algebra, this can be rewritten as

$$\mathcal{J}_i = \mathcal{A}_i \cdot \ell_N$$

for some linear operator \mathcal{A}_i . Explicitly, focal stack now becomes

$$[\mathcal{J}_1, \dots, \mathcal{J}_i, \dots, \mathcal{J}_N] = [\mathcal{A}_1 \ell_N, \dots, \mathcal{A}_i \ell_N, \dots, \ell_N]$$

and can be cast into the following desired form:

$$\mathcal{J} = \mathcal{A} \cdot \ell, \text{ where}$$

$$\mathcal{J} = [\mathcal{J}_1, \dots, \mathcal{J}_i, \dots, \mathcal{J}_N], \mathcal{A} = [\mathcal{A}_1, \dots, \mathcal{A}_i, \dots, \mathcal{A}_N] \text{ and } \ell = \ell_N \text{ is the light field on the last film.}$$

On completion of the derivation in the continuous form, we now work on its discrete counterpart for practical computation. The light field is first discretized as:

$$\ell(\mathbf{x}, \mathbf{u}) \approx \sum_{\mathbf{m}} \sum_{\mathbf{p}} \ell[\mathbf{m}, \mathbf{p}] \cdot \text{rect}_{\Delta_x}(\mathbf{x} - \mathbf{m}\Delta_x) \text{rect}_{\Delta_u}(\mathbf{u} - \mathbf{p}\Delta_u)$$

where \mathbf{m} and \mathbf{p} are index vectors of dimension 2 that correspond to \mathbf{x} and \mathbf{u} respectively.

The integration is then replaced by summation for the image formation of $\ell[\mathbf{m}, \mathbf{p}]$. It has been shown by H. Nien that the image formation $\mathcal{J}^H[\mathbf{m}]$ on the sensor with the transformed light field $\ell^H[\mathbf{m}, \mathbf{p}]$ is:¹⁶⁸

$$\mathcal{J}^H[\mathbf{m}] = (\ell * \mathbf{g})[\mathbf{m}', \mathbf{p}'] \Big|_{\mathbf{m}'=a\mathbf{m}, \mathbf{p}'=\frac{c\Delta_x}{\Delta_u}\mathbf{m}},$$

$$\text{where } \mathbf{g}[\mathbf{m}, \mathbf{p}] = (s * t)(\mathbf{m}\Delta_x, \mathbf{p}\Delta_u),$$

$$s(\mathbf{x}, \mathbf{u}) = \text{rect}_{\Delta_x}(\mathbf{x})\text{rect}_{\Delta_u}(\mathbf{u}) \text{ and } t(\mathbf{x}, \mathbf{u}) = \frac{1}{|\det(\mathbf{H})|} \text{rect}_{|\det(\mathbf{H})|\Delta_x}(\mathbf{d}\mathbf{x} - \mathbf{b}\mathbf{u})$$

and a, b, c, d are the matrix elements of $\mathbf{H} = \begin{bmatrix} a & b \\ c & d \end{bmatrix}$.

As we have derived the refocusing transformation \mathbf{H}_i^F , the forward model for a single focal sheet, \mathcal{A}_i , can be explicitly defined with the above equations, and the discrete focal stack images can finally be cast in the linear closed form of:

$$\mathcal{F}[\mathbf{m}] = \mathcal{A} \cdot \ell[\mathbf{m}, \mathbf{p}],$$

where $\mathcal{F}[\mathbf{m}] = \left[\mathcal{J}^{\mathbf{H}_1^F}[\mathbf{m}], \dots, \mathcal{J}^{\mathbf{H}_i^F}[\mathbf{m}], \dots, \mathcal{J}^{\mathbf{H}_N^F}[\mathbf{m}] \right]$ is the discrete focal stack, $\ell[\mathbf{m}, \mathbf{p}]$ is the discrete light field on the last film, and $\mathcal{A} = [\mathcal{A}_1, \dots, \mathcal{A}_i, \dots, \mathcal{A}_N]$ is the forward model where \mathcal{A}_i is defined as above.

Section 5.3.3 Fourier slice sampling and the detector configuration

While the spatial relationship between photograph and light field can be understood intuitively and we have explicitly derived it in the previous section, analyzing in the Fourier domain presents an even simpler view of the process of photographic imaging: a photograph is simply a 2D slice of the 4D light field.¹⁶⁹ We therefore analyze the proposed light field imaging system in the Fourier domain. This is stated formally in the following, which is a direct consequence from the Fourier slice photography theorem based on Lambertian scene and full aperture assumption:¹⁶⁷

Theorem: Fourier slice sampling with focal stack

The measurement at the i^{th} detector is given by

$$J_i(x, y) = \frac{\gamma^{i-1}}{F^2} \mathcal{F}_{2D}^{-1} \left\{ \mathcal{S}_i \left\{ \mathcal{F}_{4D} \{ \ell(x, y, u, v) \} \right\} \right\}, i = 1, \dots, N,$$

where $\mathcal{F}_{4D} \{ \ell(x, y, u, v) \} = L(\omega_x, \omega_y, \omega_u, \omega_v)$ and $\mathcal{F}_{2D} \{ \ell(x, y) \} = L(\omega_x, \omega_y)$

are the 4D and 2D Fourier transforms respectively. The slicing operator $\mathcal{S}_i \{ \cdot \}$ is defined by

$$\mathcal{S}_i \{ W \}(\omega_x, \omega_y) := W(\alpha_i \omega_x, \alpha_i \omega_y, (1 - \alpha_i) \omega_x, (1 - \alpha_i) \omega_y)$$

where F is the distance between the camera lens and the N^{th} (furthest) detector; $\alpha_i F$ corresponds to the distance between the camera lens and the i^{th} detector (i.e., $\alpha_N = 1$); $\gamma \in [0, 1]$ is the transparency of the detectors; $\omega_x, \omega_y, \omega_u, \omega_v \in \mathbb{R}$ are spatial frequencies; N is the number of detectors.

The theorem suggests that the number of 4D Fourier samples of the light field increases as the number of detectors D increases, thereby showing the improvement of reconstruction quality with D . A direct consequence of the theorem is that the i^{th} focal stack sheet would radially sample the $\omega_x - \omega_u$ and the $\omega_y - \omega_v$ Fourier domain along the line with the slope $\alpha_i / (1 - \alpha_i)$. Now suppose we are to design a light field camera of size F (distance between the last focal stack sheet and the camera lens) and the working range is between w_1 and w_2 ($w_1 > w_2$) from the imaging lens. Point sources at $w_{1,2}$ will be sharply imaged at $\alpha_{w_{1,2}} F$, which satisfies $\frac{1}{f} = \frac{1}{w_{1,2}} + \frac{1}{\alpha_{w_{1,2}} \beta}$, see Fig 5.5(a). They would confine a sector between θ_{w_1} and θ_{w_2} in the $\omega_x - \omega_u$ and $\omega_y - \omega_v$ domain, where

$$\theta_{w_1} = \tan^{-1} \frac{\alpha_{w_1}}{1 - \alpha_{w_1}}$$

$$\theta_{w_2} = \pi + \tan^{-1} \frac{\alpha_{w_2}}{1 - \alpha_{w_2}}$$

Without prior information about the scene (and therefore the corresponding 4D Fourier spectrum), we can arrange the N focal stack sheet locations such that they correspond to the radial sampling

lines that are equally angular-spaced by $\delta\theta = \frac{\theta_{w_2} - \theta_{w_1}}{N}$ within the sector (confined by the designed working range).

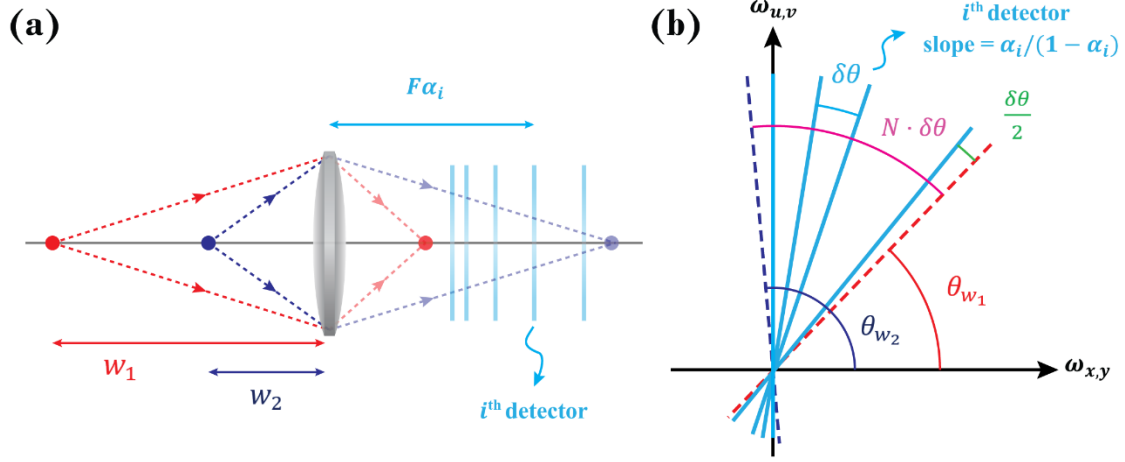


Figure 5.5 Fourier slice sampling. (a) Schematic of the system design, where the i^{th} sensor is placed at distance $F\alpha_i$ from the main lens. (b) Schematic of the radial slice sampling in the Fourier domain. The detectors are placed such that their corresponding radial sampling lines are equally angular-spaced.

As illustrated in Fig 5.5(b), such a configuration can be constructed in the following steps:

1. Numerically solve F from the constraint of $\frac{\delta\theta}{2} = \theta_{w_2} - \frac{\pi}{2}$ in terms of w_1 , w_2 , f and N
2. Calculate θ_{w_1} , θ_{w_2} and $\delta\theta$
3. Determine the position of the i^{th} focal stack sheet by

$$\alpha_i F = \frac{F \tan\left[\left(\theta_{w_1} + \frac{\delta\theta}{2}\right) + (i-1)\delta\theta\right]}{1 + \tan\left[\left(\theta_{w_1} + \frac{\delta\theta}{2}\right) + (i-1)\delta\theta\right]}$$

As a numerical example, if our light field camera is expected to work in the range of 30cm - 3m, the focal length of the imaging lens is 50 mm and has 5 transparent detectors, then they will be placed at [51.65, 53.31, 55.07, 56.95, 58.95] mm based on the above design rules.

Section 5.4 Light field reconstruction from focal stack

Section 5.4.1 Reconstruction settings

We have seen that the (sparse) 3D focal stack formation from the 4D light field can be modeled by the linear operation of $\mathcal{f} = \mathcal{A} \cdot \ell$, and the problem of reconstructing the camera light field $\hat{\ell}$ (as well as the scene light field) from the focal stack data can then be posed as the least-square minimization problem of

$$\hat{\ell} = \min_{\ell} \|\mathcal{f} - \mathcal{A} \cdot \ell\|_2^2$$

which can be solved with linear methods such as gradient descent (GD) or conjugate gradient descent (CG). Note that due to the dimensionality gap between (sparse) 3D and 4D, the reconstruction is an ill-posed problem and a proper choice of regularization is desired, which is a process of introducing additional information to help solve the underdetermined problem and takes the following form in the minimization problem:

$$\hat{\ell} = \min_{\ell} \|\mathcal{f} - \mathcal{A} \cdot \ell\|_2^2 + R(\ell)$$

The design of the regularization is a challenging problem. In the demonstrated light field reconstruction on the photorealistic scene, it is possible for the light field to be reconstructed with good quality without the regularization, if the focal stack covers the entire depth of field of the scene.

Here we address the subtleties in this specific reconstruction problem. First, we re-inspect the form of the forward model for the i^{th} focal image formation:

$$\mathcal{J}_i^{\text{H}_i^F}[\mathbf{m}] = (\ell * \mathbf{g})[\mathbf{m}', \mathbf{p}']|_{\mathbf{m}'=a\mathbf{m}, \mathbf{p}'=\frac{c\Delta_x}{\Delta_u}\mathbf{m}}, \text{ where } \text{H}_i^F = \begin{bmatrix} a & b \\ c & d \end{bmatrix} = \begin{bmatrix} \frac{F_N}{F_i} & 1 - \frac{F_N}{F_i} \\ 0 & 1 \end{bmatrix}$$

$\mathbf{g}[\mathbf{m}, \mathbf{p}]$ is the 4D refocusing kernel that can be precomputed. The operation can be understood as convolution with \mathbf{g} performed on the 2D grids of $[a\mathbf{m}, \frac{c\Delta_x}{\Delta_u}\mathbf{m}]$. Hence for any non-integer a or $\frac{c\Delta_x}{\Delta_u}$, 2D interpolation and its transpose are required for the implementation of forward and backward projections, which is computationally inefficient. The strategy therefore, is to convert the original reconstruction problem to an equivalent one that involves a simpler form of the refocusing transformation.

Now consider a synthetic camera system that consists of a main lens with a set of synthetic focal lengths (illustrated in Fig 5.6),

$$[f_1^{\text{syn}}, \dots, f_i^{\text{syn}}, \dots, f_N^{\text{syn}}], \text{ where } f_i^{\text{syn}} = \frac{1}{\frac{1}{f} + \frac{1}{F} - \frac{1}{F_i}}$$

and F_i is the distance between the main lens and the i^{th} detector in Fig 5.4.

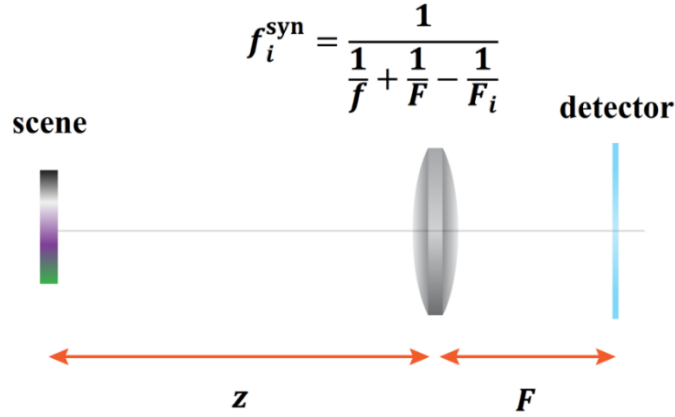


Figure 5.6 Focal stack camera with synthetic focal lengths. N images are captured with the sets of synthetic focal lengths $[f_1^{\text{syn}}, \dots, f_i^{\text{syn}}, \dots, f_N^{\text{syn}}]$. With the preprocessing of image scaling, this system is equivalent to that in Fig 5.4.

Suppose the focal stack images captured by the synthetic camera is nothing but the rescaled focal stack images in the original focal stack:

$$\mathcal{F}^{\text{syn}}[\mathbf{m}] = \left[\mathcal{J}_1 \left[\frac{F_1}{F_N} \mathbf{m} \right], \dots, \mathcal{J}_i \left[\frac{F_i}{F_N} \mathbf{m} \right], \dots, \mathcal{J}_N \right],$$

where $\mathcal{F}[\mathbf{m}] = [\mathcal{J}_1, \dots, \mathcal{J}_i, \dots, \mathcal{J}_N]$ is the original focal stack.

It can be proven that the two systems are equivalent, and the detail of the derivation is in Appendix.

The resulting refocusing transformation for the synthetic camera system is:

$$H_i^f = \begin{bmatrix} 1 & 1 - \frac{F_N}{F_i} \\ 0 & 1 \end{bmatrix}$$

where the implementation of forward model requires no interpolation ($a = 1, c = 0$), as discussed.

The complete procedure for the system design and light field reconstruction is summarized below:

1. Determine the configuration of the focal stack camera, $[F_1, \dots, F_i, \dots, F_N]$ where F_i is the distance between main lens and the i^{th} detector. This is achieved with the knowledge of the main lens focal length f , number of transparent detector films N , and the desired working range $[w_1, w_2]$.
2. Suppose the focal stack images captures by the camera is $\mathcal{J}[\mathbf{m}] = [\mathcal{J}_1, \dots, \mathcal{J}_i, \dots, \mathcal{J}_N]$, then

we perform image re-scaling to obtain

$$\mathcal{J}^{\text{syn}}[\mathbf{m}] = \left[\mathcal{J}_1 \left[\frac{F_1}{F_N} \mathbf{m} \right], \dots, \mathcal{J}_i \left[\frac{F_i}{F_N} \mathbf{m} \right], \dots, \mathcal{J}_N \right].$$

This is a pre-processing step that requires interpolation.

3. Construct the forward model \mathcal{A}^{syn} with the set of synthetic focal lengths

$$[f_1^{\text{syn}}, \dots, f_i^{\text{syn}}, \dots, f_N^{\text{syn}}], \text{ where } f_i^{\text{syn}} = \frac{1}{\frac{1}{f} + \frac{1}{F} - \frac{1}{F_i}}$$

4. Solve the optimization problem of

$$\hat{\ell} = \min_{\ell} \|\mathcal{J}^{\text{syn}} - \mathcal{A}^{\text{syn}} \cdot \ell\|_2^2 + R(\ell), \text{ where } R(\ell) \text{ is some choice of regularization}$$

and $\hat{\ell}$ is the reconstructed in-camera light field on the last sensor film.

Section 5.4.2 Light field reconstruction of the synthetic scene

With the developed procedure for model-based light field reconstruction from focal stack, we now discuss the simulation results of different synthetic scenes. We start with the study on the planar objects. In this specific case, the scene consists of two patterned disks perpendicular to the optical axis. The two disks are placed at different depths to the camera lens, transversely displaced such that one disk occludes part of the other, see Fig 5.7. In addition, the two disks are set to be *Lambertian*, meaning that the light field is constant along the directional dimension. The camera parameters are set as the following: each sensor plane is $3 \times 3 \text{ cm}^2$ in size and has 301×301 pixels; the directional resolution is set to be 11×11 and the diameter of the circular aperture is 6.6 cm.

Now we consider different scenarios of a planar scene object relative to the imaging system. One extreme case is that the object happens to be sharply imaged on one of the focal stack sheet (say the i^{th} detector). This can be regarded as the optimal detection, since the spectral energy of the scene object would disperse along the spectral lines with slope $\alpha_i/(1 - \alpha_i)$ and completely sampled by the i^{th} detector, based on the discussion in Section 5.3.3. The light field can be reconstructed with high quality using standard least-square minimization methods such as GD or CG even without any regularization except at the occlusion region. At the normal operation of camera, however, it is more likely that the spectral energy of the scene falls in-between the sampling lines, which are determined by the sensor locations. In fact, we can consider the worst-case sampling, which can be constructed as the following: place the planar object at w_b away from the main lens, which is then sharply imaged at a distance $F\alpha_b$ and the spectral line with slope $\alpha_b/(1 - \alpha_b)$ would lie in the middle of the two spectral sampling lines determined by the i^{th} and $(i + 1)^{\text{th}}$ detectors.

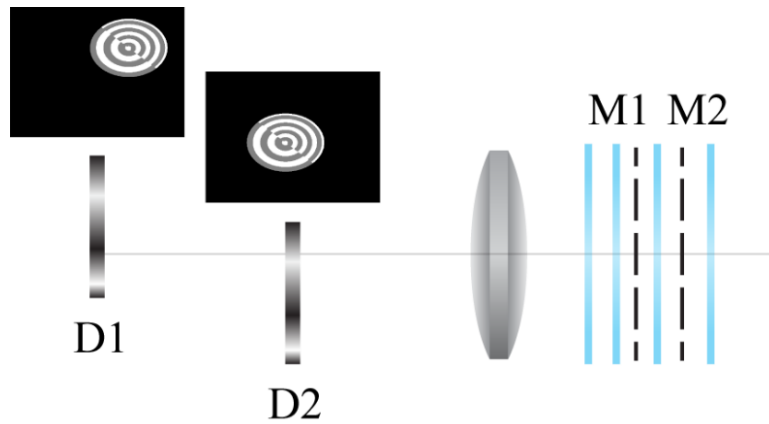


Figure 5.7 Planar scene objects of two patterned disks. The two disks are 467.3 mm and 678 mm away from the imaging lens of focal length 50 mm and are transversely displaced. The focal stack consists of 5 sensor films that are placed at [51.65, 53.31, 55.07, 56.947, 58.95] mm from the lens.

Here we demonstrate a worse-case sampling with numerical simulation. In this specific case, the back and front disks are 467.3 mm and 678 mm away from the camera lens, respectively; the five sensor films in the focal stack are placed at distances [51.65, 53.31, 55.07, 56.947, 58.95]

mm from the camera lens, with the focal length being 50 mm, see Fig 5.7. Fig 5.8 displays the captured focal stack images (with scaling). Note the back disk appears to be identical on the 2nd and 3rd focal sheet, the front disk appears to be identical on the 3rd and 4th focal sheet, and they appear to be equally blurry on the 3rd focal sheet. This is the exact manifestation that, the spectral energy of the back disk disperses along the spectral line that is equally angular-spaced between the two spectral sampling lines determined by the 2nd and 3rd focal sheet. The same reasoning applies to the front disk imaging.

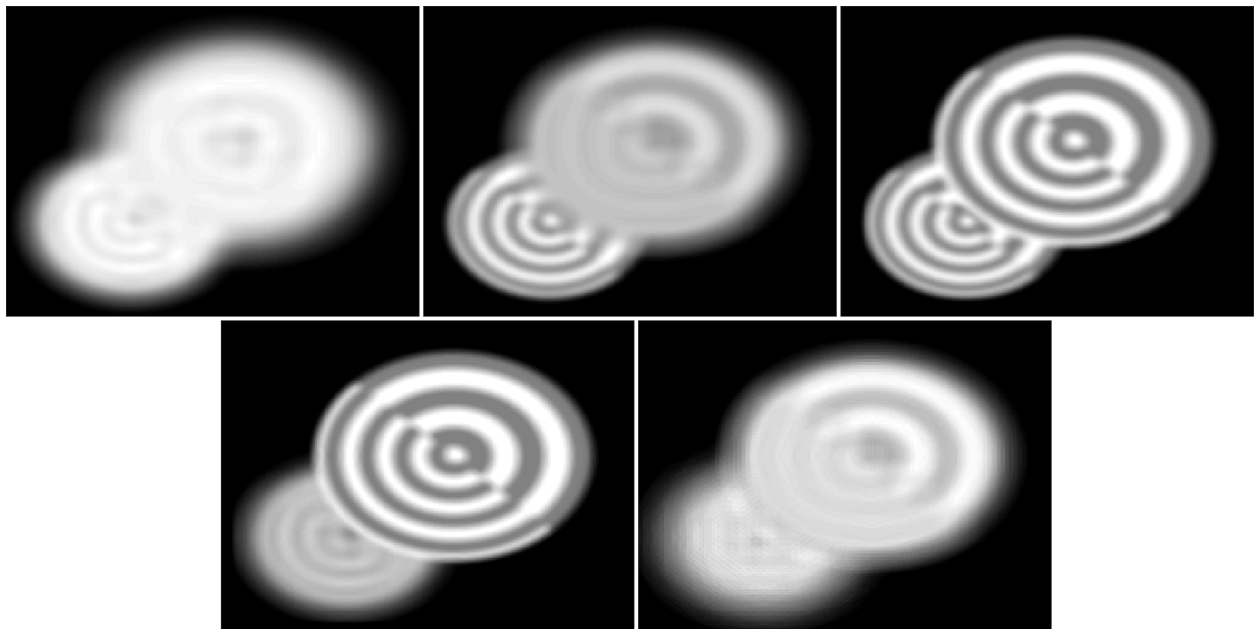


Figure 5.8 Focal stack of the worst-case sampling. Sensor films are placed from the nearest to the farthest distances with respect to the camera lens, following the order from left to right, top to down.

Now we consider the light field reconstruction of a photorealistic scene, where the scene light field is adapted from ref ¹⁷⁰. The scene depth ranges from a distance of 1.97 to 2.56 m from the camera lens. Five sensor films are arranged according to the Fourier sampling design rule, and the focal stack covers the entire depth of field of the scene. The focal stack images are displayed in Fig 5.9 and we performed the light field reconstruction from these focal stack data.

Since light field is 4D, a direct visualization on the global data is not possible. An important data subset of light field for the visual evaluation is the 2D sub-aperture image, defined as

$$s[\mathbf{m}] = \ell[\mathbf{m}, \mathbf{p}]|_{\mathbf{p}=\mathbf{p}_0}, \text{ where } \mathbf{p}_0 \text{ is some directional data grid on the aperture plane}$$

A sub-aperture image can be visualized as the image captured with the pinhole set at \mathbf{p}_0 on the aperture plane that corresponds to some view point. In fact, the process of refocusing can be understood as the adding and shifting of all the sub-aperture images. Since they are pinhole images, they should look sharp, with no blur, and are essentially the all-in-focus images. Fig 5.10 shows the reconstructed central sub-aperture image $\ell_{\text{recon}}[\mathbf{m}, \mathbf{p}_{\text{center}}]$ and is compared with the ground-truth image. Except that some spatial details are blurred, the reconstruction result well matches the ground-truth image and no obvious artifact is found at the occlusion region.



Figure 5.9 Focal stack images of the photorealistic scene. Sensor films are placed from the nearest to the farthest distances with respect to the camera lens, following the order from left to right, top to down.

The reconstruction of the light field corresponds to the full reconstruction of the sub-aperture images, i.e., the knowledge of pinhole images from all different viewpoints. Novel views besides from the central viewpoint are readily accessible, and perspective shifts from the reconstructed left, central and right viewpoints are illustrated in Fig 5.11(a). One of the direct

application is the multi-view stereo, where the depth can be perceived visually with disparity and is illustrated in Fig 5.11(b).

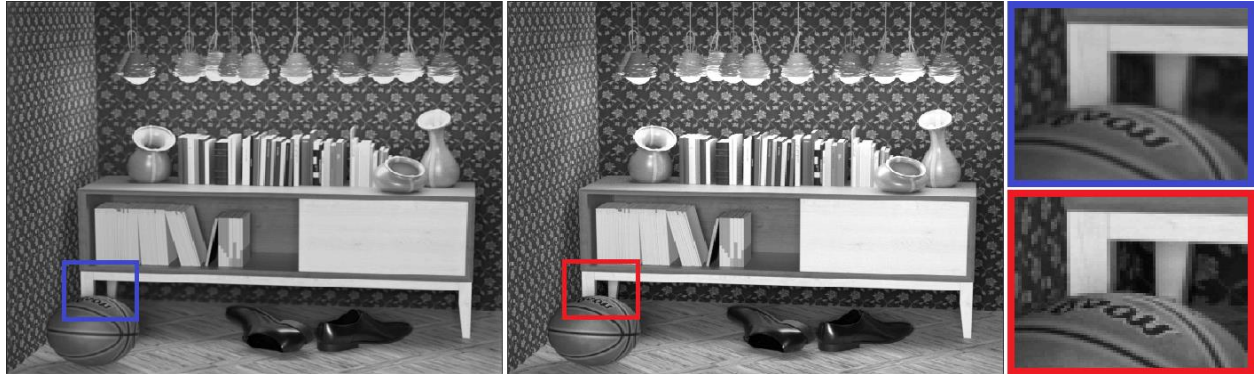


Figure 5.10 Light field reconstruction of the photorealistic scene. Left: reconstructed central sub-aperture image. Central: ground-truth sub-aperture image. Top-right: close-up view at the occlusion region in the reconstructed image. Bottom-right: close-up view at the occlusion region in the ground-truth image.

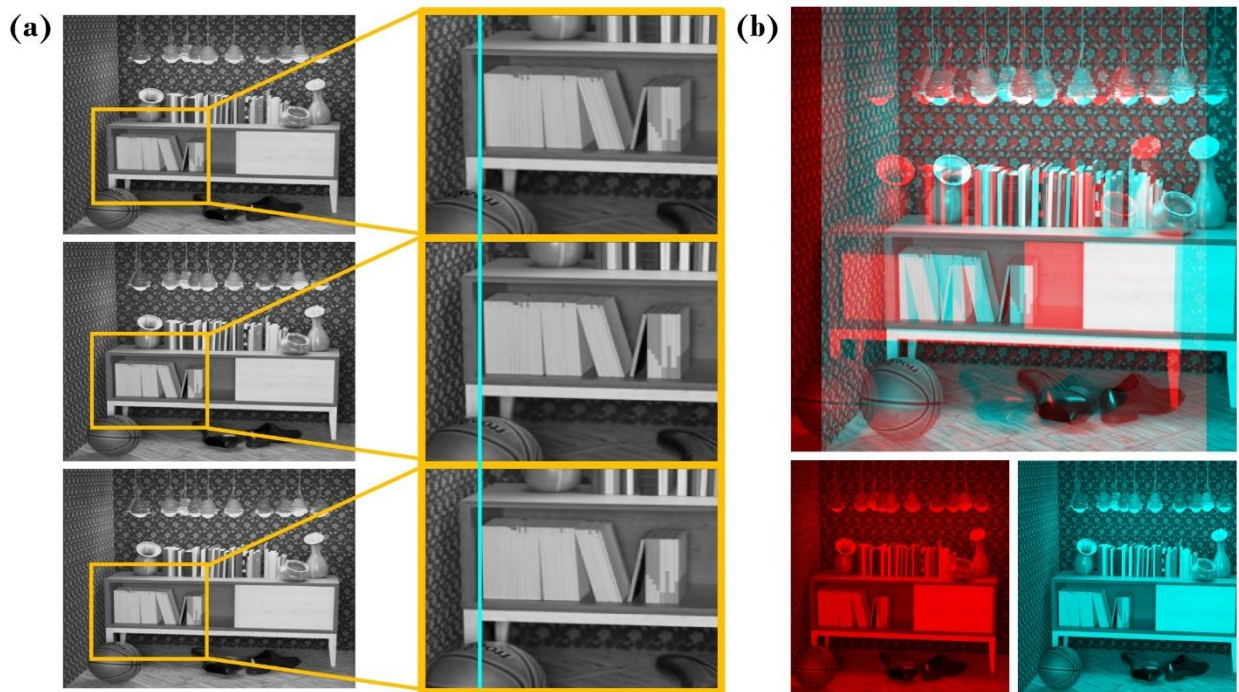


Figure 5.11 Demonstration of perspective shift and multi-view stereo. (a) The perspective shifts. The close-up views show the reconstructed disparities within the yellow rectangle boxes. Top: left viewpoint. Middle: central viewpoint. Bottom: right viewpoint (b) Top: the stereo image. Constructed by fusing sub-aperture images at different viewpoints with baseline being 10.67 cm. Bottom-left: left viewpoint. Bottom-right: right viewpoint.

Section 5.5 Summary

In this chapter, we present a complete analysis on the light field transport, the image formation process, and the camera operations such as refocusing and image rescaling. A focal stack design rule was proposed based on the equally angular-spaced Fourier sampling. The model-based light field reconstruction was performed with the synthetic photorealistic scene, where the light field applications of all-in-focus image extraction and multi-view stereo were demonstrated.

CHAPTER 6

Retrospect and Prospect

In this thesis, I have addressed several frontiers in the problems of optical scattering and imaging. The summary and potential future directions are discussed in the following.

Section 6.1 Nonlinear light scattering of nano-plasmonics

The first frontier focuses on the fundamental understanding of the nonlinear light scattering and its association with the electrostatic asymmetry in the nano-plasmonic system of AuNRs, discussed in Chapter 1 and 2.

In Chapter 1, I conducted the NLO experiment to illustrate the optical asymmetry induced by the electrostatic asymmetry of AuNRs. While the internal charge distortion effect has been discussed previously as a possible cause for the surprisingly high hyperpolarizability in AuNRs,⁶² this experiment serves as the first systematic study on the optical symmetry breaking from electrostatic asymmetry. For the first time, AuNR samples were prepared with their electrostatic asymmetry states explicitly controlled. The resulting SHG and the broadband PL from these samples, which are indicative of the degree of optical asymmetry, align with their corresponding electrostatic asymmetry conditions.

In Chapter 2, I provided a complete picture of both coherent and incoherent light scattering from AuNRs. The observed unconventional SHG and THG scaling behaviors were explained by the optical damping effect on SPR. In particular, I established a novel microscopic model that accounts for the broadband PL, where the physical origin was attributed to the scattering between the 2nd order LSPR mode and the electron gas. In the study, I performed the first spectrally resolved

intensity dependence experiment and proposed a sampling strategy for the precise measurements. The quantitative model requires only 3 physically constrained parameters to fit the entire spectrum as well as the scaling behaviors, and is consistent with other recent studies of the nonlinear optical properties of AuNRs.^{97,98}

The fundamental understanding of the optical symmetry breaking and its physical origin provides a new pathway to explain and control NLO properties. One possible future work is the implementation of a nano-plasmonic system that maximizes NLO emission based on this knowledge, where the electrostatic asymmetry involves as a new physical parameter. In particular, the experimental data in Fig 1.9 suggests the flexibility in controlling both the absolute and relative signal strengths of the SHG and the broadband PL. Another finding that attracts the attention is the nearly quadratic scaling of the total signal at 400 nm (SHG + broadband component), which is highly suggestive of a physical origin from coherent process and is an interesting subject for a quantum spectroscopic study.

Section 6.2 Light transmission through highly scattering media

The second frontier concerns a novel approach to the control of monochromatic light transmission through highly scattering media, discussed in Chapter 3.

In Chapter 3, I presented an optical system that can characterize the scattering media in the form of transmission matrix, thereby enables the control of monochromatic light transmission through the media. In most of the previous studies, the complex transmission matrix was measured using interferometric designs.^{111,112} This work serves as one of the early works toward a reference free architecture. Compared to the pioneer reference-less design using binary amplitude modulation,¹¹³ phase modulation was adopted that has a higher theoretically achievable enhancement.¹⁰² The PhaseCut algorithm was applied for the first time to solve the phase retrieval problem for the transmission matrix recovery, where SDP was used as the computational method. On applying the computed optimal wavefront, beam focused onto a point beyond the scattering medium was demonstrated.

There are several promising directions to develop based on this study. First, recall that the introduced scheme is efficient in data acquisition, where the training data for the recovery of

transmission matrix rows are simultaneously recorded on the corresponding camera pixels. One immediate follow-up work is the implementation of an infrastructure that allows the parallel computations on multiple transmission matrix rows, which can significantly reduce the required total run time of SDP. The established framework can also be used to solve other technological problems. One of such applications is its use in controlling a fiber communication system, where the multimode fiber can be characterized with a transmission matrix. Compared to the interferometric methods that most techniques use to date,¹⁰⁴ a reference-less architecture can be tremendously advantageous in the ultimate miniaturization of the end systems.

Section 6.3 Light field imaging based on graphene optics

The third frontier explores the optical saturation behavior of graphene and a specific light field camera application where graphene is the key material for the implementation of highly transparent photodetector, discussed in Chapter 4 and Chapter 5.

In Chapter 4, for the first part I conducted one of the early experimental studies for the optical saturation behavior of graphene. The differential transmission of graphene sample at increasing excitation intensities was measured to verify the microscopic theory that quantitatively describes the optical saturation as the interplay between Pauli-blocking and scattering-induced redistribution of excited carriers. The experimental data showed a good agreement with the theoretical prediction. For the second part, I presented a novel, proof-of-concept optical system that operates for light field imaging. The system has an architecture of single-pixel focal stack camera, where the focal stack consists of all-graphene heterojunction photodetectors stacked along the optical axis, which is only possible with their superior transparency. The system was physically implemented and its principle of operation was demonstrated.

In Chapter 5, I presented the computational framework for model-based light field reconstruction from focal stack dataset. The light field transport, the image formation process, and the camera operations of refocusing and image rescaling were explicitly developed. I also proposed a focal stack design rule based on the equally angular-spaced Fourier sampling. Compared to other recent studies on the reconstruction from focal stack data,^{171,172} this study provides a more general formulation and can extend to any imaging system modeled by the optical transfer matrix. A

simulation of light field reconstruction was then performed with the synthetic photorealistic scene, where the light field applications of all-in-focus image extraction and multi-view stereo were demonstrated.

Possible future improvements on the proposed system are two-fold. One the hardware side, it is a major technological step from demonstrating a single pixel to a dense 2D sensor array. The state-of-art fabrication of graphene–CMOS integration has been reported to achieved a 388×288 -pixel resolution on a 15.1×14.3 mm graphene image sensor array, even though it was not designed for the highest transparency.¹⁷³ Dense photodetector arrays based on other 2D or ultrathin materials are presumably highly transparent, and therefore can potentially be great candidates as well for the focal stack application.

On the computation side, there are two interesting directions to explore. First, while the preliminary results showed a decent light field reconstruction from the synthetic dataset, the 4D light field reconstruction from sparse 3D focal stack is intrinsically an ill-posed problem and a proper regularization is highly desired. Developing a sparsity promoting prior in the design of regularization can be plausible, due to the unique linear stripe structure of light field in the epipolar domain. Inspired by the proposed Fourier sampling, it is also possible to explore the regularization in the Fourier domain. Second, a learning approach, such as the convolutional neural network (CNN), can be a promising direction to the light field reconstruction problem. Frontier researches have demonstrated the power of learning approach in different aspects of light field photography problems.^{174,175} The data-driven nature can help bypass the need for a complicated modeling of the physical acquisition process in the device, and it is possible to reconstruct the light field with better quality as well as faster speed on successful learning process.

APPENDIX

Focal Stack Camera with Synthetic Focal Lengths

In the following we investigate the relationship between the two focal stack cameras depicted in Fig A.1(a) and Fig A.1(b). System in Fig A.1(a) captures the focal stack images using N transparent detector films placed at $[F_1, \dots, F_i, \dots, F_N]$ from the main lens (with focal length f). System in Fig A.1(b) captures the focal stack images *sequentially* on a single detector film using the main lens with a set of synthetic focal lengths $[f_1^{\text{syn}}, \dots, f_i^{\text{syn}}, \dots, f_N^{\text{syn}}]$.

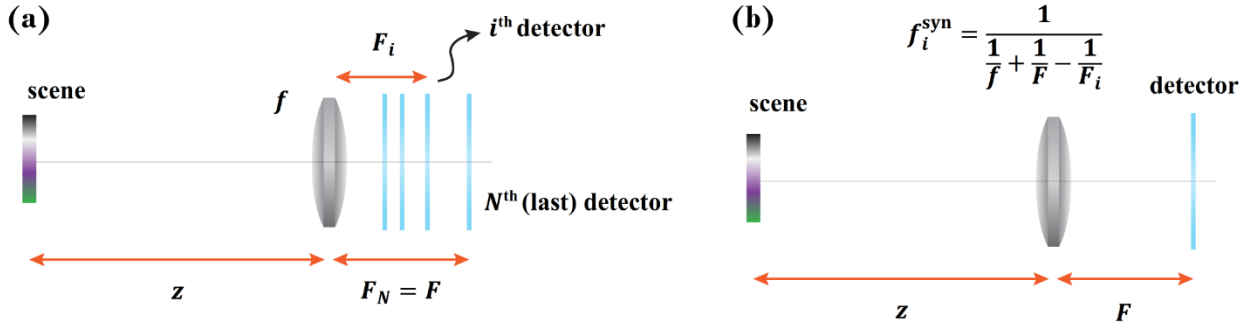


Figure A.1 Two focal stack camera schemes. (a) Multi-detector focal stack camera. (b) Multi-focus focal stack camera.

Before making the comparison, we first introduce two light field transformations. The first is the *synthetic refocusing* operation, illustrated in Fig A.2(a). Following the same reasoning in section 5.3.2, the light field after synthetic refocusing with the new focal length f' is:

$$\ell' \left(\begin{bmatrix} \mathbf{x} \\ \mathbf{u} \end{bmatrix} \right) = \ell \left(\mathbf{H}'^{-1} \mathbf{H} \begin{bmatrix} \mathbf{x} \\ \mathbf{u} \end{bmatrix} \right) = \ell \left(\mathbf{H}^f \begin{bmatrix} \mathbf{x} \\ \mathbf{u} \end{bmatrix} \right),$$

$$\text{where } H^f = \begin{bmatrix} -\frac{z}{F} & 1 - \frac{z}{f} - \frac{z}{F} \\ \frac{1}{F} & \frac{1}{f} - \frac{1}{F} \end{bmatrix}^{-1} \begin{bmatrix} -\frac{z}{F} & 1 - \frac{z}{f} - \frac{z}{F} \\ \frac{1}{F} & \frac{1}{f} - \frac{1}{F} \end{bmatrix} = \begin{bmatrix} 1 & \frac{F}{f'} - \frac{F}{f} \\ 0 & 0 \end{bmatrix}$$

The second is the *scaling* operation, illustrated in Fig A.2(b). The scaling is effectively achieved with a new focal length f' and a corresponding new film position F' , where

$$\frac{1}{f} - \frac{1}{F} = \frac{1}{z} = \frac{1}{f'} - \frac{1}{F'}$$

is satisfied as the scaling operation should preserve the imaging condition of the lens formula. It is then straight forward to show that

$$\ell' \left(\begin{bmatrix} \mathbf{x} \\ \mathbf{u} \end{bmatrix} \right) = \ell \left(H'^{-1} H \begin{bmatrix} \mathbf{x} \\ \mathbf{u} \end{bmatrix} \right) = \ell \left(H^s \begin{bmatrix} \mathbf{x} \\ \mathbf{u} \end{bmatrix} \right),$$

$$\text{where } H^s = \begin{bmatrix} -\frac{z}{F'} & 1 - \frac{z}{f'} - \frac{z}{F'} \\ \frac{1}{F'} & \frac{1}{f'} - \frac{1}{F'} \end{bmatrix}^{-1} \begin{bmatrix} -\frac{z}{F} & 1 - \frac{z}{f} - \frac{z}{F} \\ \frac{1}{F} & \frac{1}{f} - \frac{1}{F} \end{bmatrix} = \begin{bmatrix} \frac{F}{F'} & 0 \\ 0 & 1 \end{bmatrix}$$

and $s = (F/F')^{-1}$ is the scaling factor.

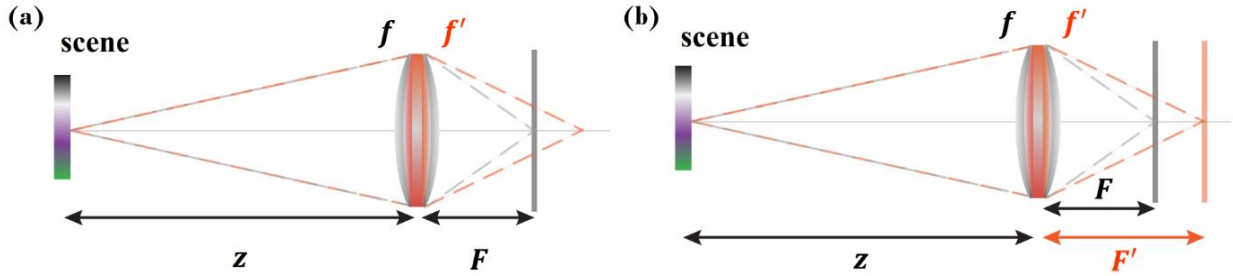


Figure A.2 Synthetic refocusing and scaling operations. (a) Synthetic refocusing operation with f changed to f' (b) Scaling operation with f changed to f' and F changed to F' . Note $\frac{1}{f} - \frac{1}{F} = \frac{1}{f'} - \frac{1}{F'}$ is satisfied.

We have seen in section 5.3.2 that for system A.1(a), the light field after refocusing at the new film position F_i is:

$$\ell_i \left(\begin{bmatrix} \mathbf{x} \\ \mathbf{u} \end{bmatrix} \right) = \ell_N \left(H_i^F \begin{bmatrix} \mathbf{x} \\ \mathbf{u} \end{bmatrix} \right), \text{ where } \ell_N \text{ is the light field on the } N^{\text{th}} \text{ film and } H_i^F = \begin{bmatrix} \frac{F_N}{F_i} & 1 - \frac{F_N}{F_i} \\ 0 & 1 \end{bmatrix}.$$

The key observation is that H_i^F can be factored as a product of H^f and H^s , if we set $f_i = \frac{1}{\frac{1}{f} + \frac{1}{F_N} - \frac{1}{F_i}}$,

i.e.,

$$H_i^F = \begin{bmatrix} \frac{F_N}{F_i} & 1 - \frac{F_N}{F_i} \\ 0 & 1 \end{bmatrix} = \begin{bmatrix} 1 & \frac{F_N}{f_i} - \frac{F_N}{f} \\ 0 & 1 \end{bmatrix} \begin{bmatrix} \frac{F_N}{F_i} & 0 \\ 0 & 1 \end{bmatrix} = \begin{bmatrix} 1 & 1 - \frac{F_N}{F_i} \\ 0 & 1 \end{bmatrix} \begin{bmatrix} \frac{F_N}{F_i} & 0 \\ 0 & 1 \end{bmatrix} = H^f H^s$$

Therefore, the operation of system A.1(a) can be interpreted as the operation of system A.1(b) followed by scaling each of the i^{th} focal stack image with the factor of $s_i = F_i/F_N$.

BIBLIOGRAPHY

- (1) Yan, J.; Han, M.; Zhang, J.; Xu, C.; Luijten, E.; Granick, S. Reconfiguring Active Particles by Electrostatic Imbalance. *Nat. Mater.* **2016**, *15*, 1095–1099.
- (2) Litchinitser, N. M.; Sun, J. Optical Meta-Atoms: Going Nonlinear. *Science* **2015**, *350*, 1033–1034.
- (3) Alkilany, A. M.; Thompson, L. B.; Boulos, S. P.; Sisco, P. N.; Murphy, C. J. Gold Nanorods: Their Potential for Photothermal Therapeutics and Drug Delivery, Tempered by the Complexity of Their Biological Interactions. *Adv. Drug Deliv. Rev.* **2012**, *64*, 190–199.
- (4) Huang, X.; Neretina, S.; El-Sayed, M. A. Gold Nanorods: From Synthesis and Properties to Biological and Biomedical Applications. *Adv. Mater.* **2009**, *21*, 4880–4910.
- (5) N’Gom, M.; Li, S.; Schatz, G.; Erni, R.; Agarwal, A.; Kotov, N.; Norris, T. B. Electron-Beam Mapping of Plasmon Resonances in Electromagnetically Interacting Gold Nanorods. *Phys. Rev. B - Condens. Matter Mater. Phys.* **2009**, *80*, 113411.
- (6) Vesseur, E. J. R.; de Waele, R.; Kuttge, M.; Polman, A. Direct Observation of Plasmonic Modes in Au Nanowires Using High-Resolution Cathodoluminescence Spectroscopy. *Nano Lett.* **2007**, *7*, 2843–2846.
- (7) Imura, K.; Nagahara, T.; Okamoto, H. Near-Field Two-Photon-Induced Photoluminescence from Single Gold Nanorods and Imaging of Plasmon Modes. *J. Phys. Chem. B* **2005**, *109*, 13214–13220.
- (8) Kim, J.-Y.; Han, M.-G.; Lien, M.-B.; Magonov, S.; Zhu, Y.; Ferguson, H.; Norris, T.; Nicholas A. Kotov Hidden Asymmetry of Gold Nanorods. *Sci. Adv.* **2017**.
- (9) Lohse, S. E.; Murphy, C. J. The Quest for Shape Control: A History of Gold Nanorod Synthesis. *Chem. Mater.* **2013**, *25*, 1250–1261.
- (10) Jana, N. R.; Gearheart, L.; Murphy, C. J. Wet Chemical Synthesis of High Aspect Ratio Cylindrical Gold Nanorods. *J. Phys. Chem. B* **2001**, *105*, 4065–4067.
- (11) Jana, N. R.; Gearheart, L.; Murphy, C. J. Seed-Mediated Growth Approach for Shape-Controlled Synthesis of Spheroidal and Rod-like Gold Nanoparticles Using a Surfactant Template. *Adv. Mater.* **2001**, *13*, 1389–1393.
- (12) Nikoobakht, B.; El-Sayed, M. A. Preparation and Growth Mechanism of Gold Nanorods (NRs) Using Seed-Mediated Growth Method. *Chem. Mater.* **2003**, *15*, 1957–1962.
- (13) Jana, N. R. Gram-Scale Synthesis of Soluble, near-Monodisperse Gold Nanorods and Other Anisotropic Nanoparticles. *Small* **2005**, *1*, 875–882.

- (14) Ali, M. R. K.; Snyder, B.; El-Sayed, M. A. Synthesis and Optical Properties of Small Au Nanorods Using a Seedless Growth Technique. *Langmuir* **2012**, *28*, 9807–9815.
- (15) Bohren, C. F.; Huffman, D. R. Absorption and Scattering of Light by Small Particles; John Wiley & Sons: New York, 1983.
- (16) Jain, P. K.; Huang, W.; El-Sayed, M. A. On the Universal Scaling Behavior of the Distance Decay of Plasmon Coupling in Metal Nanoparticle Pairs: A Plasmon Ruler Equation. *Nano Lett.* **2007**, *7*, 2080–2088.
- (17) Hu, M.; Chen, J.; Li, Z.-Y.; Au, L.; Hartland, G.V.; Li, X.; Marquez, M.; Xia, Y. Gold Nanostructures: Engineering Their Plasmonic Properties for Biomedical Applications. *Chem. Soc. Rev.* **2006**, *35*, 1084–1094.
- (18) Kumar, A.; Mazinder Boruah, B.; Liang, X. J. Gold Nanoparticles: Promising Nanomaterials for the Diagnosis of Cancer and HIV/AIDS. *J. Nanomater.* **2011**, *2011*, 1–17.
- (19) Raschke, G.; Kowarik, S.; Franzl, T.; Sönnichsen, C.; Klar, T. A.; Feldmann, J.; Nichtl, A.; Kürzinger, K. Biomolecular Recognition Based on Single Gold Nanoparticle Light Scattering. *Nano Lett.* **2003**, *3*, 935–938.
- (20) Sönnichsen, C.; Franzl, T.; Wilk, T.; von Plessen, G.; Feldmann, J.; Wilson, O.; Mulvaney, P. Drastic Reduction of Plasmon Damping in Gold Nanorods. *Phys. Rev. Lett.* **2002**, *88*, 77402.
- (21) Novo, C.; Gomez, D.; Perez-Juste, J.; Zhang, Z.; Petrova, H.; Reismann, M.; Mulvaney, P.; Hartland, G.V. Contributions from Radiation Damping and Surface Scattering to the Linewidth of the Longitudinal Plasmon Band of Gold Nanorods: A Single Particle Study. *Phys. Chem. Chem. Phys.* **2006**, *8*, 3540–3546.
- (22) Hao, E.; Schatz, G. C. Electromagnetic Fields around Silver Nanoparticles and Dimers. *J. Chem. Phys.* **2004**, *120*, 357–366.
- (23) McPeak, K. M.; Jayanti, S.V.; Kress, S. J. P.; Meyer, S.; Iotti, S.; Rossinelli, A.; Norris, D. J. Plasmonic Films Can Easily Be Better: Rules and Recipes. *ACS Photonics* **2015**, *2*, 326–333.
- (24) Prescott, S. W.; Mulvaney, P. Gold Nanorod Extinction Spectra. *J. Appl. Phys.* **2006**, *99*, 123504.
- (25) Brioude, A.; Jiang, X. C.; Pileni, M. P. Optical Properties of Gold Nanorods: DDA Simulations Supported by Experiments. *J. Phys. Chem. B* **2005**, *109*, 13138–13142.
- (26) Baban, D. F.; Seymour, L. W. Control of Tumour Vascular Permeability. *Adv. Drug Deliv. Rev.* **1998**, *34*, 109–119.
- (27) Iyer, A. K.; Khaled, G.; Fang, J.; Maeda, H. Exploiting the Enhanced Permeability and Retention Effect for Tumor Targeting. *Drug Discov. Today* **2006**, *11*, 812–818.
- (28) Ferrari, M. Cancer Nanotechnology: Opportunities and Challenges. *Nat. Rev. Cancer* **2005**, *5*, 161–171.

- (29) Brannon-Peppas, L.; Blanchette, J. O. Nanoparticle and Targeted Systems for Cancer Therapy. *Adv. Drug Deliv. Rev.* **2012**, *64*, 206–212.
- (30) Ghosh, P.; Han, G.; De, M.; Kim, C. K.; Rotello, V. M. Gold Nanoparticles in Delivery Applications. *Adv. Drug Deliv. Rev.* **2008**, *60*, 1307–1315.
- (31) Tong, L.; Zhao, Y.; Huff, T. B.; Hansen, M. N.; Wei, A.; Cheng, J. X. Gold Nanorods Mediate Tumor Cell Death by Compromising Membrane Integrity. *Adv. Mater.* **2007**, *19*, 3136–3141.
- (32) Huff, T. B.; Tong, L.; Zhao, Y.; Hansen, M. N.; Cheng, J.-X.; Wei, A. Hyperthermic Effects of Gold Nanorods on Tumor Cells. *Nanomedicine* **2007**, *2*, 125–132.
- (33) Durr, N. J.; Larson, T.; Smith, D. K.; Korgel, B. A.; Sokolov, K.; Ben-Yakar, A. Two-Photon Luminescence Imaging of Cancer Cells Using Molecularly Targeted Gold Nanorods. *Nano Lett.* **2007**, *7*, 941–945.
- (34) Huang, X.; El-Sayed, I. H.; Qian, W.; El-Sayed, M. A. Cancer Cells Assemble and Align Gold Nanorods Conjugated to Antibodies to Produce Highly Enhanced, Sharp, and Polarized Surface Raman Spectra: A Potential Cancer Diagnostic Marker. *Nano Lett.* **2007**, *7*, 1591–1597.
- (35) Takahashi, H.; Niidome, Y.; Yamada, S. Controlled Release of Plasmid DNA from Gold Nanorods Induced by Pulsed near-Infrared Light. *Chem. Commun.* **2005**, *17*, 2247–2249.
- (36) Chen, C. C.; Lin, Y. P.; Wang, C. W.; Tzeng, H. C.; Wu, C. H.; Chen, Y. C.; Chen, C. P.; Chen, L. C.; Wu, Y. C. DNA-Gold Nanorod Conjugates for Remote Control of Localized Gene Expression by near Infrared Irradiation. *J. Am. Chem. Soc.* **2006**, *128*, 3709–3715.
- (37) Wijaya, A.; Schaffer, S. B.; Pallares, I. G.; Hamad-Schifferli, K. Selective Release of Multiple DNA Oligonucleotides from Gold Nanorods. *ACS Nano* **2009**, *3*, 80–86.
- (38) Somin, E. L.; Sasaki, D. Y.; Perroud, T. D.; Yoo, D.; Patel, K. D.; Lee, L. P. Biologically Functional Cationic Phospholipid-Gold Nanoplasmonic Carriers of RNA. *J. Am. Chem. Soc.* **2009**, *131*, 14066–14074.
- (39) Hong, R.; Han, G.; Fernández, J. M.; Kim, B. J.; Forbes, N. S.; Rotello, V. M. Glutathione-Mediated Delivery and Release Using Monolayer Protected Nanoparticle Carriers. *J. Am. Chem. Soc.* **2006**, *128*, 1078–1079.
- (40) Polizzi, M. A.; Stasko, N. A.; Schoenfish, M. H. Water-Soluble Nitric Oxide-Releasing Gold Nanoparticles. *Langmuir* **2007**, *23*, 4938–4943.
- (41) Kawano, T.; Niidome, Y.; Mori, T.; Katayama, Y.; Niidome, T. PNIPAM Gel-Coated Gold Nanorods for Targeted Delivery Responding to a near-Infrared Laser. *Bioconjug. Chem.* **2009**, *20*, 209–212.
- (42) Alper, J.; Crespo, M.; Hamad-Schifferli, K. Release Mechanism of Octadecyl Rhodamine B Chloride from Au Nanorods by Ultrafast Laser Pulses. *J. Phys. Chem. C* **2009**, *113*, 5967–5973.
- (43) Kim, C. K.; Ghosh, P.; Pagliuca, C.; Zhu, Z. J.; Menichetti, S.; Rotello, V. M. Entrapment

- of Hydrophobic Drugs in Nanoparticle Monolayers with Efficient Release into Cancer Cells. *J. Am. Chem. Soc.* **2009**, *131*, 1360–1361.
- (44) Ni, W.; Kou, X.; Yang, Z.; Wang, J. Tailoring Longitudinal Surface Plasmon Wavelengths, Scattering and Absorption Cross Sections of Gold Nanorods. *ACS Nano* **2008**, *2*, 677–686.
- (45) Mohamed, M. B.; Volkov, V.; Link, S.; El-Sayed, M. A. The “Lightning” Gold Nanorods: Fluorescence Enhancement of over a Million Compared to the Gold Metal. *Chem. Phys. Lett.* **2000**, *317*, 517–523.
- (46) Lee, K. S.; El-Sayed, M. A. Dependence of the Enhanced Optical Scattering Efficiency Relative to that of Absorption for Gold Metal Nanorods on Aspect Ratio, Size, End-Cap Shape, and Medium Refractive Index. *J. Phys. Chem. B* **2005**, *109*, 20331–20338.
- (47) Huang, X.; El-Sayed, I. H.; Qian, W.; El-Sayed, M. A. Cancer Cell Imaging and Photothermal Therapy in the near-Infrared Region by Using Gold Nanorods. *J. Am. Chem. Soc.* **2006**, *128*, 2115–2120.
- (48) Wang, H.; Huff, T. B.; Zweifel, D. A.; He, W.; Low, P. S.; Wei, A.; Cheng, J.-X. In Vitro and in Vivo Two-Photon Luminescence Imaging of Single Gold Nanorods. *Proc. Natl. Acad. Sci.* **2005**, *102*, 15752–15756.
- (49) Oldenburg, A. L.; Hansen, M. N.; Zweifel, D. A.; Wei, A.; Boppart, S. A. Plasmon-Resonant Gold Nanorods as Low Backscattering Albedo Contrast Agents for Optical Coherence Tomography. *Opt. Express* **2006**, *14*, 6724–6738.
- (50) Li, P.-C.; Wang, C.-R. C.; Shieh, D.-B.; Wei, C.-W.; Liao, C.-K.; Poe, C.; Jhan, S.; Ding, A.-A.; Wu, Y.-N. In Vivo Photoacoustic Molecular Imaging with Simultaneous Multiple Selective Targeting Using Antibody-Conjugated Gold Nanorods. *Opt. Express* **2008**, *16*, 18605–18615.
- (51) Zharov, V. P.; Mercer, K. E.; Galitovskaya, E. N.; Smeltzer, M. S. Photothermal Nanotherapeutics and Nanodiagnostics for Selective Killing of Bacteria Targeted with Gold Nanoparticles. *Biophys. J.* **2006**, *90*, 619–627.
- (52) El-Sayed, I. H.; Huang, X.; El-Sayed, M. A. Selective Laser Photo-Thermal Therapy of Epithelial Carcinoma Using Anti-EGFR Antibody Conjugated Gold Nanoparticles. *Cancer Lett.* **2006**, *239*, 129–135.
- (53) Dickerson, E. B.; Dreaden, E. C.; Huang, X.; El-Sayed, I. H.; Chu, H.; Pushpanketh, S.; McDonald, J. F.; El-Sayed, M. A. Gold Nanorod Assisted near-Infrared Plasmonic Photothermal Therapy (PPTT) of Squamous Cell Carcinoma in Mice. *Cancer Lett.* **2008**, *269*, 57–66.
- (54) von Maltzahn, G.; Park, J. H.; Agrawal, A.; Bandaru, N. K.; Das, S. K.; Sailor, M. J.; Bhatia, S. N. Computationally Guided Photothermal Tumor Therapy Using Long-Circulating Gold Nanorod Antennas. *Cancer Res.* **2009**, *69*, 3892–3900.
- (55) Kelly, K. L.; Coronado, E.; Zhao, L. L.; Schatz, G. C. The Optical Properties of Metal Nanoparticles: The Influence of Size, Shape, and Dielectric Environment. *J. Phys. Chem. B* **2003**, *107*, 668–677.

- (56) Sönnichsen, C.; Reinhard, B. M.; Liphardt, J.; Alivisatos, A. P. A Molecular Ruler Based on Plasmon Coupling of Single Gold and Silver Nanoparticles. *Nat. Biotechnol.* **2005**, *23*, 741–745.
- (57) Murphy, C. J.; Gole, A. M.; Hunyadi, S. E.; Stone, J. W.; Sisco, P. N.; Alkilany, A.; Kinard, B. E.; Hankins, P. Chemical Sensing and Imaging with Metallic Nanorods. *Chem. Commun.* **2008**, *5*, 544–557.
- (58) Anker, J. N.; Hall, W. P.; Lyandres, O.; Shah, N. C.; Zhao, J.; van Duyne, R. P. Biosensing with Plasmonic Nanosensors. *Nat. Mater.* **2008**, *7*, 442–453.
- (59) Wang, C.; Chen, Y.; Wang, T.; Ma, Z.; Su, Z. Biorecognition-Driven Self-Assembly of Gold Nanorods: A Rapid and Sensitive Approach toward Antibody Sensing. *Chem. Mater.* **2007**.
- (60) Brewer, S. H.; Glomm, W. R.; Johnson, M. C.; Knag, M. K.; Franzen, S. Probing BSA Binding to Citrate-Coated Gold Nanoparticles and Surfaces. *Langmuir* **2005**.
- (61) Rossouw, D.; Couillard, M.; Vickery, J.; Kumacheva, E.; Botton, G. A. Multipolar Plasmonic Resonances in Silver Nanowire Antennas Imaged with a Subnanometer Electron Probe. *Nano Lett.* **2011**, *11*, 1499–1504.
- (62) Singh, A.; Lehoux, A.; Remita, H.; Zyss, J.; Ledoux-Rak, I. Second Harmonic Response of Gold Nanorods: A Strong Enhancement with the Aspect Ratio. *J. Phys. Chem. Lett.* **2013**, *4*, 3958–3961.
- (63) Leonov, A. P.; Zheng, J.; Clogston, J. D.; Stern, S. T.; Patri, A. K.; Wei, A. Detoxification of Gold Nanorods by Treatment with Polystyrenesulfonate. *ACS Nano* **2008**, *2*, 2481–2488.
- (64) Gole, A.; Murphy, C. J. Polyelectrolyte-Coated Gold Nanorods: Synthesis, Characterization and Immobilization. *Chem. Mater.* **2005**, *17*, 1325–1330.
- (65) Lien, M.-B.; Kim, J.-Y.; Han, M.-G.; Chang, Y.-C.; Chang, Y.-C.; Heather J. Ferguson; Zhu, Y.; Andrew A. Herzing; Schotland, J. C.; Nicholas A. Kotov; *et al.* Optical Asymmetry and Nonlinear Light Scattering from Colloidal Gold Nanorods. *ACS Nano* **2017**, *11*, 5925–5932.
- (66) Kauranen, M.; Zayats, A.V. Nonlinear Plasmonics. *Nat. Photonics* **2012**, *6*, 737–748.
- (67) Link, S.; Mohamed, M. B.; El-Sayed, M. A. Simulation of the Optical Absorption Spectra of Gold Nanorods as a Function of Their Aspect Ratio and the Effect of the Medium Dielectric Constant. *J. Phys. Chem. B* **1999**, *103*, 3073–3077.
- (68) Jain, P. K.; Lee, K. S.; El-Sayed, I. H.; El-Sayed, M. A. Calculated Absorption and Scattering Properties of Gold Nanoparticles of Different Size, Shape, and Composition: Applications in Biological Imaging and Biomedicine. *J. Phys. Chem. B* **2006**, *110*, 7238–7248.
- (69) Fava, D.; Nie, Z.; Winnik, M. A.; Kumacheva, E. Evolution of Self-Assembled Structures of Polymer-Terminated Gold Nanorods in Selective Solvents. *Adv. Mater.* **2008**, *20*, 4318–4322.

- (70) York, J.; Spetzler, D.; Xiong, F.; Frasn, W. D. Single-Molecule Detection of DNA via Sequence-Specific Links between F1-ATPase Motors and Gold Nanorod Sensors. *Lab Chip* **2008**, *8*, 415–419.
- (71) Durr, N. J.; Larson, T.; Smith, D. K.; Korgel, B. A.; Sokolov, K.; Ben-Yakar, A. Two-Photon Luminescence Imaging of Cancer Cells Using Molecularly Targeted Gold Nanorods. *Nano Lett.* **2007**, *7*, 941–945.
- (72) Boyd, G. T.; Yu, Z. H.; Shen, Y. R. Photoinduced Luminescence from the Noble Metals and Its Enhancement on Roughened Surfaces. *Phys. Rev. B* **1986**, *33*, 7923–7936.
- (73) Farrer, R. A.; Butterfield, F. L.; Chen, V. W.; Fourkas, J. T. Highly Efficient Multiphoton-Absorption-Induced Luminescence from Gold Nanoparticles. *Nano Lett.* **2005**, *5*, 1139–1142.
- (74) Tong, L.; Wei, Q.; Wei, A.; Cheng, J.-X. Gold Nanorods as Contrast Agents for Biological Imaging: Optical Properties, Surface Conjugation and Photothermal Effects. *Photochem. Photobiol.* **2009**, *85*, 21–32.
- (75) Lippitz, M.; Dijk, M. A.; Orrit, M. Third-Harmonic Generation from Single Gold Nanoparticles. *Nano Lett.* **2005**, *5*, 799–802.
- (76) Schwartz, O.; Oron, D. Background-Free Third Harmonic Imaging of Gold Nanorods. *Nano Lett.* **2009**, *9*, 4093–4097.
- (77) Dadap, J. I.; Shan, J.; Eisenthal, K. B.; Heinz, T. F. Second-Harmonic Rayleigh Scattering from a Sphere of Centrosymmetric Material. *Phys. Rev. Lett.* **1999**, *83*, 4045–4048.
- (78) Dadap, J. I.; Shan, J.; Heinz, T. F. Theory of Optical Second-Harmonic Generation from a Sphere of Centrosymmetric Material: Small-Particle Limit. *J. Opt. Soc. Am. B* **2004**, *21*, 1328–1347.
- (79) Hao, E. C.; Schatz, G. C.; Johnson, R. C.; Hupp, J. T. Hyper-Rayleigh Scattering from Silver Nanoparticles. *J. Chem. Phys.* **2002**, *117*, 5963–5966.
- (80) Russier-Antoine, I.; Benichou, E.; Bachelier, G.; Jonin, C.; Brevet, P. F. Multipolar Contributions of the Second Harmonic Generation from Silver and Gold Nanoparticles. *J. Phys. Chem. C* **2007**, *111*, 9044–9048.
- (81) Bachelier, G.; Russier-Antoine, I.; Benichou, E.; Jonin, C.; Brevet, P.-F. Multipolar Second-Harmonic Generation in Noble Metal Nanoparticles. *J. Opt. Soc. Am. B* **2008**, *25*, 955–960.
- (82) Butet, J.; Duboisset, J.; Bachelier, G.; Russier-Antoine, I.; Benichou, E.; Jonin, C.; Brevet, P.-F. Optical Second Harmonic Generation of Single Metallic Nanoparticles Embedded in a Homogeneous Medium. *Nano Lett.* **2010**, *10*, 1717–1721.
- (83) Nik, B.; El-Sayed, M. A. Preparation and Growth Mechanism of Gold Nanorods (NRs) Using Seed - Mediated Growth Method. *J. Phys. Chem. A* **2003**, *15*, 1957–1962.
- (84) Kim, J.-Y.; Lien, M.-B.; Han, M.-G.; Zhu, Y.; Norris, T.; Kotov, N. Charge Anisotropy of Gold Nanorods *251st American Chemical Society National meeting & Exposition*; American Chemical Society: San Diego, 2016; p. 244.

- (85) Völkl, E.; Allard, L. F.; Joy, D. C. Introduction to Electron Holography; 1st ed.; Springer US, 1999; Vol. 53.
- (86) Kim, J.-Y.; Lien, M.-B.; Han, M.-G.; Magonov, S.; Zhu, Y.; Ferguson, H.; Norris, T.; Kotov, N. Hidden Asymmetry of Gold Nanorods. *Accept by Sci. Adv.* **2017**.
- (87) Link, S.; Ei-Sayed, M. A. Spectroscopic Determination of the Melting Energy of a Gold Nanorod. *J. Chem. Phys.* **2001**, *114*, 2362–2368.
- (88) Hubert, C.; Billot, L.; Adam, P.-M.; Bachelot, R.; Royer, P.; Grand, J.; Gindre, D.; Dorkenoo, K. D.; Fort, A. Role of Surface Plasmon in Second Harmonic Generation from Gold Nanorods. *Appl. Phys. Lett.* **2007**, *90*, 181105.
- (89) Boyd, R. W. Nonlinear Optics; 3rd ed.; Academic Press, 2008.
- (90) Groeneveld, R. H. M.; Sprik, R.; Lagendijk, A. Femtosecond Spectroscopy of Electron-Electron and Electron-Phonon Energy Relaxation in Ag and Au. *Phys. Rev. B* **1995**, *51*, 11433–11445.
- (91) Perner, M.; Bost, P.; Lemmer, U.; Plessen, G.; Feldmann, J.; Becker, U.; Mennig, M.; Schmitt, M.; Schmidt, H. Optically Induced Damping of the Surface Plasmon Resonance in Gold Colloids. *Phys. Rev. Lett.* **1997**, *78*, 2192–2195.
- (92) Lin, Z.; Zhigilei, L.V.; Celli, V. Electron-Phonon Coupling and Electron Heat Capacity of Metals under Conditions of Strong Electron-Phonon Nonequilibrium. *Phys. Rev. B* **2008**, *77*, 75133.
- (93) Verellen, N.; Denkova, D.; Clercq, B.; Silhanek, A.V.; Ameloot, M.; Dorpe, P.; Moshchalkov, V.V. Two-Photon Luminescence of Gold Nanorods Mediated by Higher Order Plasmon Modes. *ACS Photonics* **2015**, *2*, 410–416.
- (94) Beversluis, M. R.; Bouhelier, A.; Novotny, L. Continuum Generation from Single Gold Nanostructures through near-Field Mediated Intraband Transitions. *Phys. Rev. B* **2003**, *68*, 115433.
- (95) Bouhelier, A.; Bachelot, R.; Lerondel, G.; Kostcheev, S.; Royer, P.; Wiederrecht, G. P. Surface Plasmon Characteristics of Tunable Photoluminescence in Single Gold Nanorods. *Phys. Rev. Lett.* **2005**, *95*, 267405.
- (96) Imura, K.; Nagahara, T.; Okamoto, H. Near-Field Two-Photon-Induced Photoluminescence from Single Gold Nanorods and Imaging of Plasmon Modes. *J. Phys. Chem. B* **2005**, *109*, 13214–13220.
- (97) Knittel, V.; Fischer, M. P.; Roo, T.; Mecking, S.; Leitenstorfer, A.; Brida, D. Nonlinear Photoluminescence Spectrum of Single Gold Nanostructures. *ACS Nano* **2015**, *9*, 894–900.
- (98) Mertens, J.; Kleemann, M.-E.; Chikkaraddy, R.; Narheng, P. How Light Is Emitted by Plasmonic Metals. *Nano Lett.* **2017**, *17*, 2568–2574.
- (99) William, H.; Rodney, L. Scattering of Light by Crystals; John Wiley & Sons, 1978.
- (100) Agarwal, G. S. Brownian Motion of a Quantum Oscillator. *Phys. Rev. A* **1971**, *4*, 739–747.

- (101) Agarwal, G. S. Quantum Electrodynamics in the Presence of Dielectrics and Conductors. I. Electromagnetic-Field Response Functions and Black-Body Fluctuations in Finite Geometries. *Phys. Rev. A* **1975**, *11*, 230–242.
- (102) Vellekoop, I. M. Feedback-Based Wavefront Shaping. *Opt. Express* **2015**, *23*, 12189.
- (103) Vellekoop, I. M.; Mosk, A. P. Focusing Coherent Light through Opaque Strongly Scattering Media. *Opt. Lett.* **2007**, *32*, 2309.
- (104) Kim, M.; Choi, W.; Choi, Y.; Yoon, C.; Choi, W. Transmission Matrix of a Scattering Medium and Its Applications in Biophotonics. *Opt. Express* **2015**, *23*, 12648.
- (105) Čižmár, T.; Mazilu, M.; Dholakia, K. In Situ Wavefront Correction and Its Application to Micromanipulation. *Nat. Photonics* **2010**, *4*, 388–394.
- (106) Park, C.; Park, J. H.; Rodriguez, C.; Yu, H.; Kim, M.; Jin, K.; Han, S.; Shin, J.; Ko, S. H.; Nam, K. T.; *et al.* Full-Field Subwavelength Imaging Using a Scattering Superlens. *Phys. Rev. Lett.* **2014**, *113*, 113901.
- (107) van Putten, E. G.; Akbulut, D.; Bertolotti, J.; Vos, W. L.; Lagendijk, A.; Mosk, A. P. Scattering Lens Resolves Sub-100 Nm Structures with Visible Light. *Phys. Rev. Lett.* **2011**, *106*, 193905.
- (108) van Putten, E. G.; Lagendijk, A.; Mosk, A. P. Nonimaging Speckle Interferometry for High-Speed Nanometer-Scale Position Detection. *Opt. Lett.* **2012**, *37*, 1070–1072.
- (109) N’Gom, M.; Lien, M.-B.; Norris, T. B.; Michielssen, E.; Nadakuditi, R. R. Controlling Light Transmission Through Highly Scattering Media Using Semi-Definite Programming as a Phase Retrieval Computation Method. *Sci. Rep.* **2017**, *7*, 2518.
- (110) Schott, S.; Bertolotti, J.; Léger, J.-F.; Bourdieu, L.; Gigan, S. Characterization of the Angular Memory Effect of Scattered Light in Biological Tissues. *Opt. Express* **2015**, *23*, 13505.
- (111) Popoff, S. M.; Lerosey, G.; Carminati, R.; Fink, M.; Boccaro, A. C.; Gigan, S. Measuring the Transmission Matrix in Optics: An Approach to the Study and Control of Light Propagation in Disordered Media. *Phys. Rev. Lett.* **2010**, *194*, 100601.
- (112) Kim, M.; Choi, Y.; Yoon, C.; Choi, W.; Kim, J.; Park, Q.-H.; Choi, W. Maximal Energy Transport through Disordered Media with the Implementation of Transmission Eigenchannels. *Nat. Photonics* **2012**, *6*, 583–587.
- (113) Drémeau, A.; Liutkus, A.; Martina, D.; Katz, O.; Schülke, C.; Krzakala, F.; Gigan, S.; Daudet, L. Reference-Less Measurement of the Transmission Matrix of a Highly Scattering Material Using a DMD and Phase Retrieval Techniques. *Opt. Express* **2015**, *23*, 11898.
- (114) Waldspurger, I.; D’Aspremont, A.; Mallat, S. Phase Recovery, MaxCut and Complex Semidefinite Programming. *Math. Program.* **2015**, *149*, 47–81.
- (115) Grant, M.; Boyd, S. Grant, M.; Boyd, S. Available at <http://cvxr.com/cvx/>; 2010,.
- (116) Choi, Y.; Yang, T. D.; Fang-Yen, C.; Kang, P.; Lee, K. J.; Dasari, R. R.; Feld, M. S.; Choi, W. Overcoming the Diffraction Limit Using Multiple Light Scattering in a Highly

- Disordered Medium. *Phys. Rev. Lett.* **2011**, *107*, 23902.
- (117) Lee, C.; Wei, X.; Kysar, J. W.; Hone, J. Measurement of the Elastic Properties and Intrinsic Strength of Monolayer Graphene. *Science* **2008**, *321*, 385–388.
- (118) Du, X.; Skachko, I.; Barker, A.; Andrei, E. Y. Approaching Ballistic Transport in Suspended Graphene. *Nat. Nanotechnol.* **2008**, *3*, 491–495.
- (119) Novoselov, K. S.; Geim, A. K.; Morozov, S.V; Jiang, D.; Zhang, Y.; Dubonos, S.V; Grigorieva, I.V; Firsov, A. A. Electric Field Effect in Atomically Thin Carbon Films. *Science* **2004**, *306*, 666–669.
- (120) Mak, K. F.; Lee, C.; Hone, J.; Shan, J.; Heinz, T. F. Atomically Thin MoS₂: A New Direct-Gap Semiconductor. *Phys. Rev. Lett.* **2010**, *105*, 136805.
- (121) Gorbachev, R.V.; Riaz, I.; Nair, R. R.; Jalil, R.; Britnell, L.; Belle, B. D.; Hill, E. W.; Novoselov, K. S.; Watanabe, K.; Taniguchi, T.; *et al.* Hunting for Monolayer Boron Nitride: Optical and Raman Signatures. *Small* **2011**, *7*, 465–468.
- (122) Geim, A. K.; Grigorieva, I.V; Hunt, B.; Sanchez-Yamagishi, J. D.; Young, A. F.; Yankowitz, M.; LeRoy, B. J.; Watanabe, K.; Taniguchi, T.; Moon, P.; *et al.* Van Der Waals Heterostructures. *Nature* **2013**, *499*, 419–425.
- (123) Bao, Q.; Loh, K. P. Graphene Photonics, Plasmonics, and Broadband Optoelectronic Devices. *ACS Nano* **2012**, *6*, 3677–3694.
- (124) Xia, F.; Mueller, T.; Lin, Y.; Valdes-Garcia, A.; Avouris, P. Ultrafast Graphene Photodetector. *Nat. Nanotechnol.* **2009**, *4*, 839–843.
- (125) Gabor, N. M.; Song, J. C. W.; Ma, Q.; Nair, N. L.; Taychatanapat, T.; Watanabe, K.; Taniguchi, T.; Levitov, L. S.; Jarillo-Herrero, P. Hot Carrier-Assisted Intrinsic Photoresponse in Graphene. *Science* **2011**, *334*, 648–652.
- (126) Yan, J.; Kim, M.-H.; Elle, J. A.; Sushkov, A. B.; Jenkins, G. S.; Milchberg, H. M.; Fuhrer, M. S.; Drew, H. D. Dual-Gated Bilayer Graphene Hot-Electron Bolometer. *Nat. Nanotechnol.* **2012**, *7*, 472–478.
- (127) Park, J.; Ahn, Y. H.; Ruiz-Vargas, C. Imaging of Photocurrent Generation and Collection in Single-Layer Graphene. *Nano Lett.* **2009**, *9*, 1742–1746.
- (128) Furchi, M.; Urich, A.; Pospischil, A.; Lilley, G.; Unterrainer, K.; Detz, H.; Klang, P.; Andrews, A. M.; Schrenk, W.; Strasser, G.; *et al.* Microcavity-Integrated Graphene Photodetector. *Nano Lett.* **2012**, *12*, 2773–2777.
- (129) Liu, C.-H.; Chang, Y.-C.; Norris, T. B.; Zhong, Z. Graphene Photodetectors with Ultra-Broadband and High Responsivity at Room Temperature. *Nat. Nanotechnol.* **2014**, *9*, 273–278.
- (130) Winzer, T.; Knorr, A.; Mittendorff, M.; Winnerl, S.; Lien, M. Bin; Sun, D.; Norris, T. B.; Helm, M.; Malic, E. Absorption Saturation in Optically Excited Graphene. *Appl. Phys. Lett.* **2012**, *101*, 221115.
- (131) Wallace, P. R. The Band Theory of Graphite. *Phys. Rev.* **1947**, *71*, 622–634.

- (132) Castro Neto, A. H.; Guinea, F.; Peres, N. M. R.; Novoselov, K. S.; Geim, A. K. The Electronic Properties of Graphene. *Rev. Mod. Phys.* **2009**, *81*, 109–162.
- (133) Wu, X.; Li, X.; Song, Z.; Berger, C.; de Heer, W. A. Weak Antilocalization in Epitaxial Graphene: Evidence for Chiral Electrons. *Phys. Rev. Lett.* **2007**, *98*, 136801.
- (134) Katsnelson, M. I.; Novoselov, K. S.; Geim, A. K. Chiral Tunnelling and the Klein Paradox in Graphene. *Nat. Phys.* **2006**, *2*, 620–625.
- (135) Chang, Y. C.; Liu, C. H.; Liu, C. H.; Zhong, Z.; Norris, T. B. Extracting the Complex Optical Conductivity of Mono- and Bilayer Graphene by Ellipsometry. *Appl. Phys. Lett.* **2014**, *104*, 261909.
- (136) Stauber, T.; Peres, N. M. R.; Geim, A. K. Optical Conductivity of Graphene in the Visible Region of the Spectrum. *Phys. Rev. B - Condens. Matter Mater. Phys.* **2008**, *78*, 85432.
- (137) Falkovsky, L. A.; Pershoguba, S. S. Optical Far-Infrared Properties of a Graphene Monolayer and Multilayer. *Phys. Rev. B - Condens. Matter Mater. Phys.* **2007**, *76*, 153410.
- (138) Falkovsky, L. A.; Varlamov, A. A. Space-Time Dispersion of Graphene Conductivity. *Eur. Phys. J. B* **2007**, *56*, 281–284.
- (139) Nair, R. R.; Blake, P.; Grigorenko, A. N.; Novoselov, K. S.; Booth, T. J.; Stauber, T.; Peres, N. M. R.; Geim, A. K. Fine Structure Constant Defines Visual Transparency of Graphene. *Science* **2008**, *320*, 1308.
- (140) A. N. Grigorenko, M. Polini, K. S. N. Graphene Plasmonics. *Nat. Photonics* **2012**, *6*, 749–758.
- (141) Wang, F.; Zhang, Y.; Tian, C.; Girit, C.; Zettl, A.; Crommie, M.; Shen, Y. R. Gate-Variable Optical Transitions in Graphene. *Science* **2008**, *320*, 206–209.
- (142) Phare, C. T.; Daniel Lee, Y.-H.; Cardenas, J.; Lipson, M. Graphene Electro-Optic Modulator with 30 GHz Bandwidth. *Nat. Photonics* **2015**, *9*, 511–514.
- (143) Yang, L.; Deslippe, J.; Park, C.-H.; Cohen, M. L.; Louie, S. G. Excitonic Effects on the Optical Response of Graphene and Bilayer Graphene. *Phys. Rev. Lett.* **2009**, *103*, 186802.
- (144) Breusing, M.; Kuehn, S.; Winzer, T.; Malić, E.; Milde, F.; Severin, N.; Rabe, J. P.; Ropers, C.; Knorr, A.; Elsaesser, T. Ultrafast Nonequilibrium Carrier Dynamics in a Single Graphene Layer. *Phys. Rev. B - Condens. Matter Mater. Phys.* **2011**, *83*, 153410.
- (145) Malic, E.; Winzer, T.; Bobkin, E.; Knorr, A. Microscopic Theory of Absorption and Ultrafast Many-Particle Kinetics in Graphene. *Phys. Rev. B - Condens. Matter Mater. Phys.* **2011**, *84*, 205406.
- (146) Mak, K. F.; Ju, L.; Wang, F.; Heinz, T. F. Optical Spectroscopy of Graphene: From the Far Infrared to the Ultraviolet. *Solid State Commun.* **2012**, *152*, 1341–1349.
- (147) Sun, Z.; Hasan, T.; Torrisi, F.; Popa, D.; Privitera, G.; Wang, F.; Bonaccorso, F.; Basko, D. M.; Ferrari, A. C. Graphene Mode-Locked Ultrafast Laser. *ACS Nano* **2010**, *4*, 803–810.
- (148) Bao, Q.; Zhang, H.; Wang, Y.; Ni, Z.; Yan, Y.; Shen, Z. X.; Loh, K. P.; Tang, D. Y. Atomic-

- Layer Graphene as a Saturable Absorber for Ultrafast Pulsed Lasers. *Adv. Funct. Mater.* **2009**, *19*, 3077–3083.
- (149) Vasko, F. T. Saturation of Interband Absorption in Graphene. *Phys. Rev. B - Condens. Matter Mater. Phys.* **2010**, *82*, 245422.
- (150) de Heer, W. A.; Berger, C.; Wu, X.; First, P. N.; Conrad, E. H.; Li, X.; Li, T.; Sprinkle, M.; Hass, J.; Sadowski, M. L.; *et al.* Epitaxial Graphene. *Solid State Commun.* **2007**, *143*, 92–100.
- (151) de Heer, W. A.; Berger, C.; Wu, X.; Sprinkle, M.; Hu, Y.; Ruan, M.; Stroschio, J. A.; First, P. N.; Haddon, R.; Piot, B.; *et al.* Epitaxial Graphene Electronic Structure and Transport. *J. Phys. D. Appl. Phys.* **2010**, *43*, 374007.
- (152) Hass, J.; Varchon, F.; Millan-Otoya, J. E.; Sprinkle, M.; Sharma, N.; de Heer, W. A.; Berger, C.; First, P. N.; Magaud, L.; Conrad, E. H. Why Multilayer Graphene on 4H-SiC(0001) Behaves like a Single Sheet of Graphene. *Phys. Rev. Lett.* **2008**, *100*, 125504.
- (153) Konstantatos, G.; Badioli, M.; Gaudreau, L.; Osmond, J.; Bernechea, M.; de Arquer, F. P. G.; Gatti, F.; Koppens, F. H. L. Hybrid Graphene–quantum Dot Phototransistors with Ultrahigh Gain. *Nat. Nanotechnol.* **2012**, *7*, 363–368.
- (154) Liu, C.-H. Graphene Transistor Based Nanoelectronic and Nanophotonic Applications (Thesis), 2016.
- (155) Ihrke, I.; Restrepo, J.; Mignard-Debise, L. Principles of Light Field Imaging: Briefly Revisiting 25 Years of Research *IEEE Signal Processing Magazine*; 2016; Vol. 33, pp. 59–69.
- (156) Ng, R.; Levoy, M.; Brédif, M.; Duval, G.; Horowitz, M.; Hanrahan, P. Light Field Photography with a Hand-Held Plenoptic Camera *Computer Science Technical Report CSTR*; 2005; Vol. 2, pp. 1–11.
- (157) Lam, E. Y. Computational Photography with Plenoptic Camera and Light Field Capture: Tutorial. *J. Opt. Soc. Am. A* **2015**, *32*, 2021.
- (158) Liang, C.-K.; Lin, T.-H.; Wong, B.-Y.; Liu, C.; Chen, H. H. Programmable Aperture Photography: Multiplexed Light Field Acquisition *ACM Transactions on Graphics (TOG)*; ACM, 2008; Vol. 27, p. 55.
- (159) Venkataraman, K.; Lelescu, D.; Duparré, J.; McMahon, A.; Molina, G.; Chatterjee, P.; Mullis, R.; Nayar, S. PiCam: An Ultra-Thin High Performance Monolithic Camera Array *ACM Transactions on Graphics (TOG)*; 2013; Vol. 32, p. 166.
- (160) Xu, Z.; Ke, J.; Lam, E. High-Resolution Lightfield Photography Using Two Masks. *Opt. Express* **2012**, *20*, 10971–10983.
- (161) Veeraraghavan, A.; Raskar, R.; Agrawal, A.; Mohan, A.; Tumblin, J. Dappled Photography: Mask Enhanced Cameras for Heterodyned Light Fields and Coded Aperture Refocusing. *ACM Trans. Graph.* **2007**, *26*, 69.
- (162) Liang, C.-K. Analysis, Acquisition, and Processing of Light Field for Computational

- Photography (Thesis), 2009.
- (163) Adelson, E. H.; Bergen, J. R. The Plenoptic Function and the Elements of Early Vision; 1991.
- (164) Levoy, M.; Hanrahan, P. Light Field Rendering *Proceedings of the 23rd annual conference on Computer graphics and interactive techniques*; ACM, 1996; pp. 31–42.
- (165) Zhan, Y. Light Field Imaging (Thesis), 2013.
- (166) Liang, C.-K.; Shih, Y.-C.; Chen, H. H. Light Field Analysis for Modeling Image Formation *IEEE Transactions on Image Processing*; 2011; Vol. 20, pp. 446–460.
- (167) Ng, R. Fourier Slice Photography *ACM Transactions on Graphics (TOG)*; ACM, 2005; Vol. 24, pp. 735–744.
- (168) Nien, H. Model-Based X-Ray CT Image and Light Field Reconstruction Using Variable Splitting Methods (Thesis), 2014.
- (169) Ng, R. Digital Light Field Photography (Thesis), 2006.
- (170) Honauer, K.; Johannsen, O.; Kondermann, D.; Goldluecke, B. A Dataset and Evaluation Methodology for Depth Estimation on 4D Light Fields *Asian Conference on Computer Vision*; Springer: Cham, 2017; pp. 19–34.
- (171) Yin, X.; Wang, G.; Li, W.; Liao, Q. Iteratively Reconstructing 4D Light Fields from Focal Stacks. *Appl. Opt.* **2016**, *55*, 8457–8463.
- (172) Alonso, J. R.; Fernández, A.; Ferrari, J. A. Reconstruction of Perspective Shifts and Refocusing of a Three-Dimensional Scene from a Multi-Focus Image Stack. *Appl. Opt.* **2016**, *55*, 2380–2386.
- (173) Goossens, S.; Navickaite, Gabriele Monasterio, Carles, Gupta, S.; José Piqueras, J.; Pérez, R.; Burwell, G.; Nikitskiy, I.; Lasanta, T.; Galán, T.; Puma, E.; Centeno, A.; *et al.* Broadband Image Sensor Array Based on graphene–CMOS Integration. *Nat. Photonics* **2017**, *11*, 366–371.
- (174) Wang, T.; Zhu, J.-Y.; Kalantari, N. K.; Efros, A. A.; Ramamoorthi, R. Light Field Video Capture Using a Learning-Based Hybrid Imaging System. *SIGGRAPH* **2017**, *36*.
- (175) Kalantari, N. K.; Wang, T.; Ramamoorthi, R. Learning-Based View Synthesis for Light Field Cameras *ACM Transactions on Graphics (TOG)*; 2016; Vol. 35, p. 193.